Geochemistry of lava samples collected near the oceanic detachments at 13ºN along the Mid-Atlantic Ridge

Master of Science Thesis

Randi Storeide

Department of Earth Science University of

Bergen June 2017

August 2017

Abstract

The structure and composition of the oceanic lithosphere is mainly controled by the supply of magmatic melts to the ridge axis. At slow-spreading, mid-oceanic ridges are characterized by complex spreading styles, where large variations in the melt supply are resulting in intermittent volcanism. During periods of reduced magmatic activity, spreading is accomodated by displacement on low-angle extensional detachement faults, forming Oceanic Core Complexes (OCC). These deep-seated faults are ultimately exhuming lower crust and upper mantle material, exposing all types of eruptive and plutonic igneous rocks, as well as mantle-derived ultramafic rocks variably altered and deformed (MacLeod, J. Escartín et al. 2002, Escartín, Mével et al. 2003, Dick, Tivey et al. 2008). This composite geological setting is suggesting a complex history and interplay between tectonic deformation and magmatic supply around OCCs.The aim of this study is to characterize the spatiotemporal evolution of magmatic processes concomitant with the development of a detachment fault. The foundation of this geochemical work is a recent detailed study of the tectonic structure and evolution of detachment fault zones at 13°20'N and 13°30'N along the Mid-Atlantic Ridge (Escartín, Mével et al. 2017). Highresolution microbathymetry, coupled with samples collected by deepsea vehicles are allowing us to present a geochemical dataset integrated in a complex OCC geological landscape. New major, trace elements and Sr, Nd, Pb and Hf isotopes, together with previously published data (Wilson, Murton et al. 2013), are used to build a petrogenetic model. Geochemical variance comparable to that of the entire Mid-Atlantic Ridge suggest a heterogenous mantle source as well as complex melting- and post-melting modifications. Enriched melt signals is best explaned by includiong a fusible, recycled mantle component, whereas depleted signals require the presence of a anomalous residual mantle component. Off-axis volcanism through permeable fault zones is indicated by the presence of *in-situ*, unevolved basalts in fault disrupted areas. Prolonged periods of melt starvation and enhanced crustal accretion by fault displacement is likely to reflect the combination of two different mechanisms: (1) reduced influen the recycled, fusible mantle component, and (2) diversionof melts away from the spreading axis fault zone conduits.

Acknowledgment

I firstly want to offer my most sincere gratitude to my amazing advisor, Assoc. Prof. Cédric Hamelin for sharing his ideas, and for believing in my project. His efforts and enthusiasm have been essential for my motivation and progress. During lab work and isotopic analysis (MC-ICP-MS), he has included me in every step, giving me valuable, hands-on experience. The knowledge he has shared with me has been crucial for my thesis, and will be useful in my future career as a geologist. I could not have wished for a more committed, talented advisor. I would be proud to work with you again. I would also like to express a warm gratitude to, Prof. Javier Escartín (IPGP, France) for several productive discussions and for providing bathymetrical maps from the study area. His knowledge on oceanic core complexes has been both impressive and inspiring. My gratitude is further extended to Dr. Antoine Bezos and the University of Nantes for our collaboration. The staff at the Bergen Analytical Facility deserve a warm gratitude for their assistance. I want to thank Yuval Ronen for providing Sr-measurements (TIMS) and for preparing samples for trace element measurements. I also want to thank Siv Hjorth Dundaas for performing trace element analyses (ICP-MS). I thank Vilde Nesbø Bakke, Karoline Brunborg, Solveig Lie Onstad and Lars Ottemo Gärtner for proofreading my thesis and for providing valuable feedback. Acknowledgements are also offered to the faculty at the University if Bergen for educating me, and to my fellow students for making the past 5 years memorable. Lastly, I would like to thank my incredibly patient friends and family for their endless support and patience through it all.

Table of Contents

1. Introduction

Some of the most striking morphological features associated with slow-spreading ridges are kilometer scale, domed, and corrugated elevations in an otherwise chaotic and disrupted terrain (Cannat, Sauter et al. 2006). These dome shaped undulations have been interpreted as fault planes of particularly large-offset, low angle detachment faults, speculated to reflect long-term (1-2 Ma) strain localization on initially steep normal-faults (*e.g.* Cann, Blackman et al. (1997), Tucholke, Lin et al. (1998), MacLeod, J. Escartín et al. (2002), Cannat, Sauter et al. (2006)). In the past two decades, the nature and distribution of these features have been of growing interest. Topographic, lithological, and geophysical data has revealed that crustal accretion is often focused onto oceanic detachment faults when present. During the 2010 Chapman Conference on Detachment in Oceanic lithosphere, crustal accretion accommodated by oceanic detachment faults was accepted as a distinct mode of seafloor spreading (Escartín and Canales 2011).

The growing understanding of detachment faults have led to a consensus on the dynamic of these features. A link between emergence of detachment faults and protracted periods of magma starvation pinpoint magmatism as an essential control on their initiation and evolution (Tucholke, Lin et al. 1998, Escartin, Smith et al. 2008, MacLeod, Searle et al. 2009).

The causes for these occasional periods of magma starvation along parts of mid-oceanic ridges remain ambiguous. In a recent study of two detachment faults, located at 13º20'N and 13º30'N along the Mid-Atlantic Ridge (MAR), Wilson, Murton et al. (2013) argued for a direct link between mantle heterogeneities and the transition from magmatic to detachment fault spreading. This reasoning was based on petrogenetic analysis of dredged basalt samples. During the ODEMAR (Oceanic DEtachment faults at the Mid Atlantic Ridge) cruise in 2013, a comprehensive survey of these detachment faults and the surrounding area was carried out. This survey included microbathymetry data, video imagery, and rock sampling performed by a Remotely Operated Vehicle (ROV) (Escartín, Mével et al. 2017).

In this study, the theory proposed by Wilson, Murton et al. (2013) will be revisited in the light of a new, improved dataset acquired during the ODEMAR cruise. Based on the compiled dataset, a comprehensive petrogenetic model will be proposed. Unlike Wilson et al., (2013), our dataset is primarily based on detailed, *in-situ* sampling, as well as high-resolution maps. This allows for

combining morphological and geochemical observations. More specifically, this study seeks to further constrain the nature the 13º20'N and 13º30'N detachment faults, the melting conditions and melting mantle components during their initiation and evolution.

2. Background

2.1 Mid-Oceanic Ridge physical processes

2.1.1 Spreading rate and ridge classification

Observation of reversals on the seafloor reveal that the rate of seafloor spreading varies along mid-oceanic ridges (Müller, Sdrolias et al. 2008), with spreading rates from 10 mm/yr to 100 mm/yr (Forsyth and Langmuir 2007). Based on spreading rate, mid-oceanic ridges can be sub-divided into three classes; fast- (> 70 mm/yr), intermediate- (50-70 mm/yr), and slow-spreading ridges (<50 mm/yr) (Dick, Lin et al. 2003, Smith 2013).

Across-axis profiles of spreading ridges reveal some distinctive characteristics for the different classes. Fast-spreading ridges are associated with a gently elevated, symmetrical, dome shaped axial high (Dick, Lin et al. 2003, Sen 2014). Magmatic isostasy indicates that high temperatures and a robust magmatic crust prevail along these ridges (Klein 2003, Buck, Lavier et al. 2005). The structure of the oceanic crust is generally believed to correspond to the Penrose model (by Penrose Conference Participants in 1972). According to this model, the oceanic crust is composed of the following sequence of layers from base to top: mantle, dunite, gabbro, a "sheeted" dike complex, pillow lavas, and sediments. With reducing spreading rates, the axial relief abates. Intermediate ridges appear negatively relieved, with tectonically disturbed axial ridge valleys (figure 1a). Slow-spreading ridges are characterized by a thin oceanic crust, rugged topography, wide (20-30 km), and deep (~ 2 km) rift valley, and complex tectonic structure (Buck, Lavier et al. 2005). Crustal accretion at slow-spreading ridges may be symmetric or asymmetric along spreading axes. Symmetric spreading similar in morphology as intermediate spreading. Asymmetric slow-spreading is induced by prolonged strain localization along deep seated detachment faults (Escartin, Smith et al. 2008). Corrugated, domed, serpentinized lower

crust and upper mantle are the surface expressions of these detachment faults (MacLeod, J. Escartín et al. 2002, Reston and Ranero 2011) (figure 1b). Recently, a fourth class, ultraslow-spreading ridges with spreading rates < 20 mm/yr has been proposed (Dick, Lin et al. 2003). Intermittent volcanism, smooth, mantle-derived seafloor, symmetric spreading and a lack of transform faults are characteristic features for ultraslow-spreading ridges (Dick, Lin et al. 2003) (figure 1c).

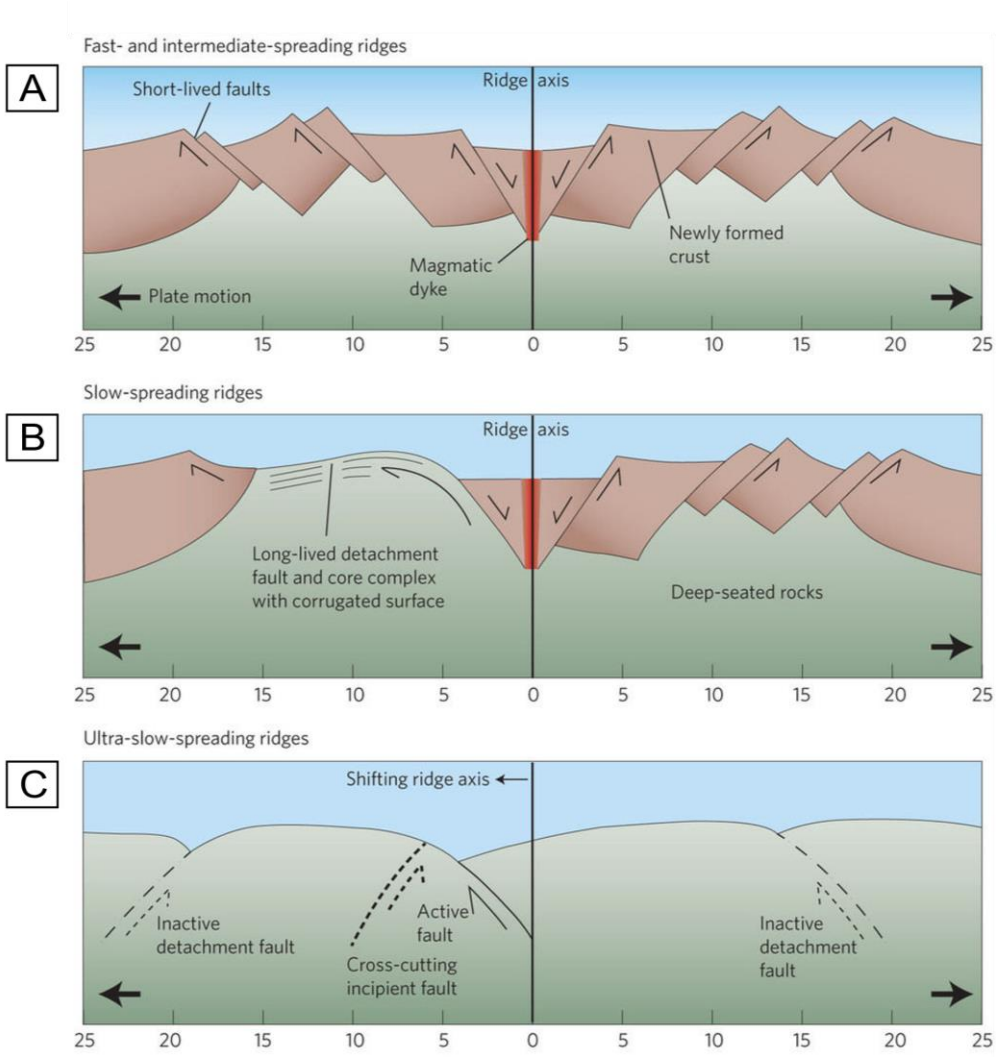

Figure 1: Cross-sections of spreading axes. (a) Fast- and intermediate-spreading mid-ocean ridges, with a narrow summit graben. Crustal accretion dominated by magmatism at the ridge axis. Seafloor spreading is symmetrical, and normal faults are small and short-lived. (b) Slow-spreading ridges with wide rift valleys and significant tectonic activity. Protracted extension along deep-seated detachment faults result in exhumation of corrugated oceanic core complexes (OCC). These are characteristic for asymmetric spreading ridges. (c) Ultra-slow-spreading ridge with very limited magmatism. Smooth detachment faults accommodate spreading on both sides of the ridge axis. As one detachment fault terminates, strain relocalizes on a new fault closer to the ridge axis. Figure from Smith (2013).

2.1.2 Spreading mode and ridge morphology

Decompression melting of the mantle beneath mid-oceanic ridges is the process responsible for oceanic crustal accretion on Earth (Klein 2003). According to this model, the upper mantle passively ascends towards Earth's surface because of plate divergence, thus compensating for plate convergence. Under spreading centres, the upper mantle follow vertical flow paths towards the surface until it no longer decompresses, and turns to a horizontal path along the oceanic lithosphere (figure 2) (Klein 2003). As hot mantle ascends towards the ridge axis, it reaches a threshold pressure (the mantle solidus depth), at which point partial melting will initiate (Forsyth and Langmuir 2007) (figure 2).

The amount of melt produced is a manifestation of the pressure-temperature conditions, which reflects the ongoing competition between heat transfer from Earth's interior by convection and heat lost by conduction to the surface (Forsyth and Langmuir 2007). As the onset of melting is deeper in hot mantle than in cold mantle, the melting column is larger, resulting in more robust melting budget and ultimately thicker oceanic crust (figure 2).

An inverse relationship exists between conductive cooling of the lithosphere and spreading rate (Dick, Lin et al. 2003, Michael, Langmuir et al. 2003). At slow spreading rates, the effect of conductive cooling is more profound than on fast spreading ridges. Truncated melting columns causes deeper melt termination and ultimately reduced melt production (Michael, Langmuir et al. 2003) (figure 2).

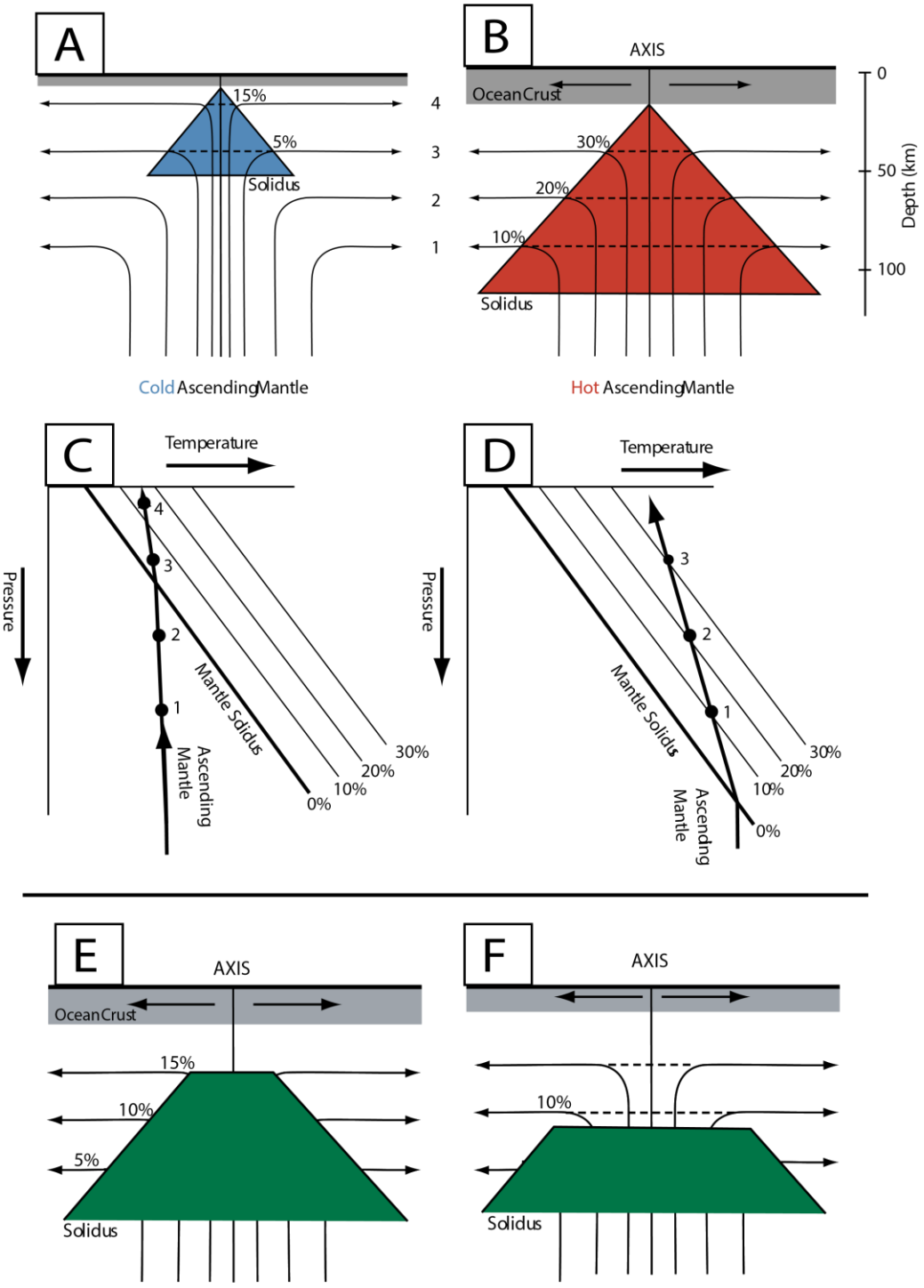

Figure 2: Diagram illustrating melting beneath mid-oceanic ridges. (a) Melting of cold mantle, resulting in a shallow melting column and a thin oceanic crust. (b) Melting of hot mantle, resulting in a deep melting column and a thick oceanic crust. (c) and (d) illustrate the temperature-pressure relationship between cold and hot mantle respectively. Flow lines (bended arrows) represent melting extents at different depths within the melting region. Corresponding values are illustrated in (c) and (d). (e) Melting beneath slow-spreading ridge. (f) Melting beneath ultraslow-spreading ridge. Reduced melting ascendance inhibits melting beneath slow- and ultra-slow-spreading ridges, resulting in truncated melting columns (i.e. trapezoids). Figure modified from Forsyth and Langmuir (2007).

As a compensation for reduced magmatism at slow- and ultra-slow-spreading ridges, crustal accretion may in part be accommodated by fault planes (Dick, Lin et al. 2003). Crustal accretion is a manifestation magmatism and/or slip on normal faults (Escartin, Smith et al. 2008, Smith, Escartín et al. 2008, MacLeod, Carlut et al. 2011). Ultimately, the bulk crustal accretion A_{tot} along spreading ridges may be expressed as the sum of magmatic accretion, A_m and tectonic accretion, A_t (MacLeod, Carlut et al. 2011).

$$A_{tot} = A_t + A_m$$

Observations suggest similar morphologies of ridges spreading at comparable rates, which in turn reflect the proportion of $A_t + A_m$ (*e.g.* Dick, Lin et al. (2003)). Volcanic ridges, lava-hummocks, and smooth lava flows characterize fast-spreading, A_m dominated ridges (figure 1a). A significant reduction in A_m and corresponding increase in A_t along intermediate-spreading ridges is manifested by the appearance of steep normal faults and a rugged abyssal-hill morphology (figure 1b). Significant morphological diversity is seen at slow- and ultra-slow-spreading ridges. Rounded, volcanic seamounts, abyssal-hills, and corrugated massifs are common features associated with these spreading centres.

2.1.3 History of Oceanic Core Complexes

The idea that normal faults could accommodate extensive strain along mid-oceanic ridges, eventually exhuming deep-seated mafic and ultramafic rocks has existed for decades (Karson 1983). In the late 1990's, corrugated, dome shaped structures termed "megamullions" were documented for the first time along a slow-spreading section (30^{o}N) of the MAR (Cann, Blackman et al. 1997, Tucholke, Lin et al. 1998). Succeeding studies refer to these structures as 'oceanic core complexes' (OCC), and linked them to their continental analogues 'metamorphic core complexes' (Karson, White et al. 1999). These corrugated, domed features have been interpreted as fault planes of low angle detachment faults (Cann, Blackman et al. 1997, Tucholke, Lin et al. 1998, MacLeod, J. Escartín et al. 2002, Cannat, Sauter et al. 2006).

Comprehensive studies dealing with petrological aspects of megamullions supported this theory by identifying *in-situ* fault rocks on these massifs (MacLeod, J. Escartín et al. 2002, Escartín, Mével et al. 2003). The present-day consensus is that OCC are tilted, exhumed footwalls of large-offset oceanic detachment faults (figure 3) (Escartín, Mével et al. 2017).

2.1.4 Nature of Oceanic Core Complexes

The formation of oceanic detachment faults (figure 3) is believed to be controlled by the magma budget (Tucholke, Lin et al. 1998, Smith, Cann et al. 2006, MacLeod, Searle et al. 2009). However, the presence of gabbro within corrugated OCC suggest some influence of magmatism, even in the presence of active detachment faults (Escartín, Mével et al. 2003, Buck, Lavier et al. 2005, Ildefonse, D.K. Blackman et al. 2007). Based on numerical models and geological data, Tucholke, Behn et al. (2008) presented the "Goldilocks Hypothesis", which refers to an optimal A_m range (between 0.3 and 0.5) for generating corrugated OCC (Buck, Lavier et al. 2005). In this model, gabbro intrusions constitutes the A_m proportion, and the corrugated surface constitutes the A_t proportion of crustal accretion (Cannat, Sauter et al. 2009).

According to the Mohr-Coulomb fracture criterion, prolonged displacement along low-angled faults (< 30^o) is unfavourable under most circumstances, and require considerable fault weakening to occur. If these conditions are met, strain will occur on existing faults rather than new ones, ultimately resulting in prolonged 'runaway displacement' (MacLeod, Searle et al. 2009). Mechanically weak faults may accommodate strain down to 20^o (Reston and Ranero 2011).

The assembly of rocks consistently recovered from corrugated fault planes range from rigid basalt and diabase to serpentinite gabbro/peridotite or even talc schists (Escartín, Mével et al. 2003). Weak, hydrous, low-temperature (< 300^oC) metamorphosed minerals such as serpentine, chlorite, and talc require significant fluid-rock interactions. Such circumstances are facilitated by circulation of fluid in mantle derived ultramafic rocks (Escartín, Mével et al. 2003). Weakest among alteration minerals is talc (Boschi, Früh-Green et al. 2006). Formation of talc rather than serpentine requires excess silica, which in turn is believed to be derived from deep-seated interactions between fluid and core-complex gabbro (MacLeod, Searle et al. 2009). Seawater

interaction with such lower-crust and upper mantle rocks requires deep seated faults. Micro seismicity, indicating depth and position of brittle deformation has been reported to extend down to 8 km below certain OCC (Escartin, Smith et al. 2008).

As suggested by Cannat, Sauter et al. (2009), there is a difference in detachment fault morphology connected to the amount of magma injected into the footwall. Corrugations are implied to be surface expressions of uneven strain accommodation induced by irregularly spaced, rigid magma bodies along the fault root (Tucholke, Behn et al. 2008). Absence of such features at detachment faults located on ultra-slow-spreading ridges thus suggests paucity or even absence of gabbro intrusions in the peridotite dominated footwall (see "smooth surfaces" in figure 1c) (Cannat, Sauter et al. 2009).

Magmatism is also believed to regulate the evolution and termination of these faults (MacLeod, Searle et al. 2009). Reduced strain focusing indicated by nucleation of steep normal faults onto, or adjacent to OCC marks the termination of detachment faults (Tucholke, Fujioka et al. 2001, MacLeod, Searle et al. 2009). This change in deformation style may be associated with increased rheological strength of the crust, which in turn reflect renewed magmatism (Cannat, Sauter et al. 2009). According to MacLeod, Searle et al. (2009), the deep root of detachment faults migrates progressively closer to, and eventually across the magma chamber in accordance with fault rotation. Renewed tectonism and volcanism in the front area of detachment faults is argued to marks their termination (MacLeod, Searle et al. 2009).

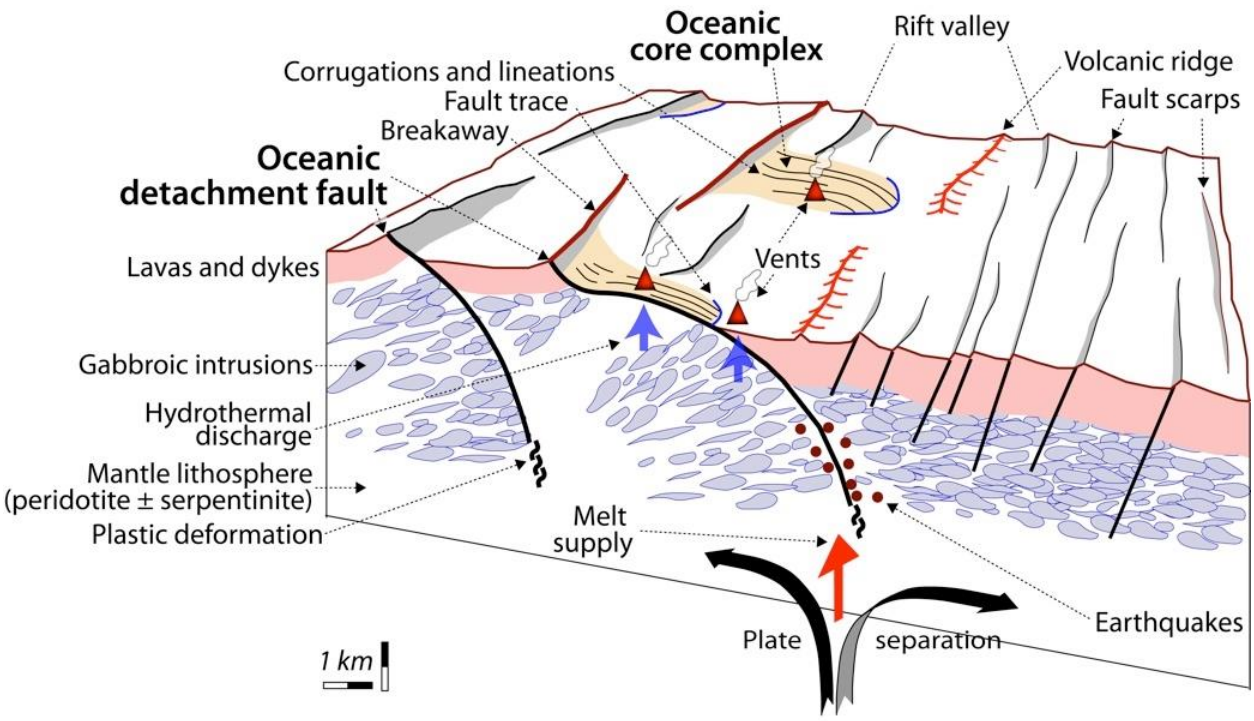

Figure 3: Schematic illustration of a slow-spreading ridge segment with a wide rift valley and asymmetric, detachment fault spreading. Corrugated, low-angle OCC are seen on the left ridge flank. The volcanic ridge is inconsistent. Hydrothermal activity and earthquakes are associated with the detachment faults. On the right ridge flank, normal faults are high-angled and the oceanic crust is dominantly volcanic. Figure presented by Javier Escartín during the 2010 Chapman Conference on Detachment in Oceanic lithosphere (Escartín and Canales 2011).

2.1.5 Prevalence and significance of Oceanic Core Complexes

A growing understanding of the mechanics and dynamics related to detachment fault has led to questioning of their lateral extent and significance as a mode of crustal accretion. When initially described, OCC were thought to be unique features. As progressively more of these features were detected along slow- and ultra-slow-spreading ridges, they became acknowledged as prominent components of the oceanic crust.

Based on literature review, Ciazela, Koepke et al. (2015) estimated that a total of 172 ridge-proximal OCC can be accounted for. The most thoroughly examined ridge sections in terms of detachment faults is the Kane area of the MAR (*e.g.* Tucholke, Lin et al. (1998)), and the Atlantis Massif area of the East Pacific Rise (Cannat, Sauter et al. 2006). In the 13º-15ºN region of the MAR, 45 candidates for detachment faults have been identified (Smith, Cann et al. (2006), Smith, Escartín et al. (2008)).

To further constrain the prevalence of these structure, it is necessary to comprehend their surface expression. It became clear from the previous section that corrugated OCC are manifestations of detachment faults wherever present. According to MacLeod, Searle et al. (2009), detachment faults are restricted to these visible features. Escartin, Smith et al. (2008) distinguishes between symmetric ridges, where spreading takes place on both sides of the spreading axis, and asymmetric ridges, where extensive displacement (>50% of the total plate separation) is focused onto a single fault. These authors further argue that detachment faults prevail even in the absence of visible OCC, and that the asymmetric geometry is the predominant testimony of detachment faults. A "blanket" of *rider blocks* covering the detachment fault footwall could justify observed asymmetry along slow-spreading ridges devoid of OCC (Escartin, Smith et al. 2008, Reston and Ranero 2011).

Evaluation of detachment faults and their role in oceanic crustal accretion ultimately suggests that these tectonic features may be more significant along slow-spreading ridges than initially assumed. Seismic- and bathymetric data between 15^{o}N and 24^{o}N of the MAR suggest that up to 35% of crustal accretion in this area is affected by detachment faults, and that >15% is dominated by OCC (Smith, Cann et al. 2006). Based on prevalence of asymmetric ridge sections between 12^{o}40'N to 35^{o}15'N of the MAR, Escartin, Smith et al. (2008) concluded up to 50% of this ridge section is dominated by detachments (figure 4). During the 2010 Chapman Conference on Detachment in Oceanic lithosphere, displacement along oceanic detachment faults was accepted as a distinct mode of seafloor spreading, and can thus be considered the tectonic manifestation of crustal accretion where present (Escartín and Canales 2011).

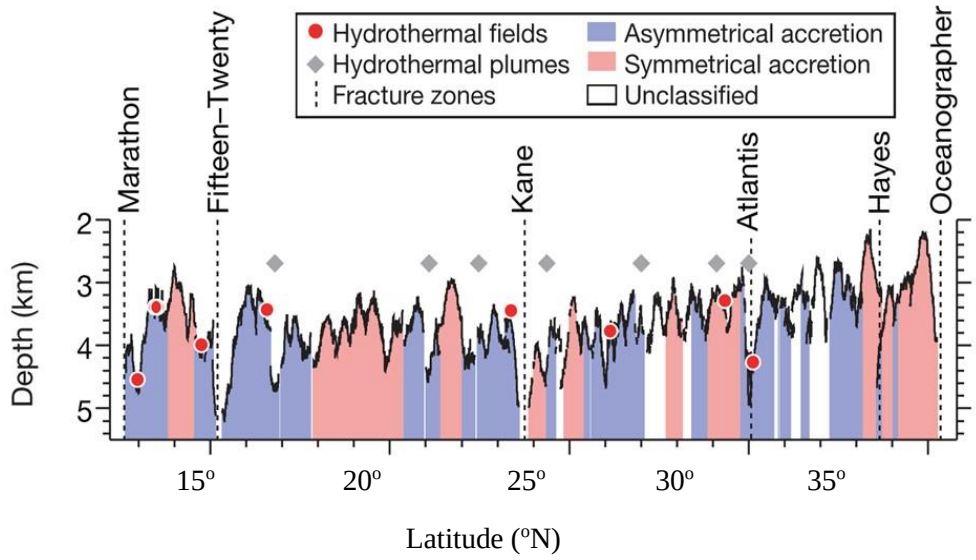

Figure 4: Latitude versus depth for the MAR between 12ºN and 35ºN, displaying up to 50 % prevalence of asymmetric spreading, Hydrothermal fields and plumes are almost exclusively located on asymmetric ridge sections. Figure modified from Escartin, Smith et al. (2008)

2.2 Mid-Oceanic Ridge basalt geochemistry

2.2.1 Basalt as a mantle source proxy

Understanding the nature and evolution of lavas erupted in vicinity of OCC is crucial for the comprehension of these structures. As mid-oceanic ridge basalts (MORB) are generated in the mantle underlying the spreading axis, they are considered as proxies for the mantle source chemistry (Donnelly, Goldstein et al. 2004, Salters and Stracke 2004, Rubin, Sinton et al. 2009, Stracke and Bourdon 2009). Lavas erupted at the ridge axis reflect the sum of different processes, which independently influence the geochemical signal. The geochemical signals measured in basalts are believed to reflect (1) source chemistry, (2) melting related element fractionation, (3) transportation modification (*i.e.* melt mixing and melt-crust interaction), and (4) mineral fractionation.

Geochemical variance in MORB is based on the different behaviour of elements in the presence of two phases (*i.e.* melt and crystals). Substitution between trace elements and major elements in the structure of rock forming minerals occur readily in nature. The ability of an element to substitute for another element, incorporated in the lattice structure, depend on the compliance in

charge and atomic radii between these elements (Goldschmidt 1954). Quantification of elements in igneous processes follows the distribution law (Hanson and Langmuir 1978).

Common trace elements are (1) fluid mobile incompatible Large Ion Lithophile Elements, *LILE* (Cs, Rb, K, Ba, Sr, Pb), (2) fluid-immobile incompatible High Field Strength Elements *HFSE* (Sc, Y, Th, U, Pb, Zr, Hf, Ti, Nb, Ta) and (3) Rare Earth Elements *REE* (La, Ce, Pr, Nd, Sm, Eu, Gd, Tb, Dy, Ho, Er, Tm, Yb, and Lu), and (4) Compatible elements (Ni, Cr, Co, V, and Sc). While compatible elements accumulate in rock-forming minerals, incompatible elements will be more concentrated in melts. It should be noted that several incompatible elements become compatible in the presence of certain minerals. This is true for Sr and Eu in the presence of plagioclase, Yb, Y, Lu in the presence of garnet, and Sc in the presence of in clinopyroxene (Hofmann 2007).

In geochemical studies, MORB samples are often categorized by their incompatible element abundance (Sun and McDonough 1989). Spider diagrams, plotting normalized (*e.g.* to chondrite) abundances of trace elements with decreased incompatibility from right to left provide a visual demonstration of the compositional variance in incompatible trace elements (Thompson, Morrison et al. 1984) (figure 5). REE are particularly useful, as these elements are analogous in all chemical and physical properties apart from atomic size, and consequently reflect a gradual decrease in incompatibility from Light Rare Earth Elements (LREE) to Heavy Rare Earth Elements (HREE). Spider diagrams may, however be cumbersome to interpret with an increasing number of samples. To resolve this issue, the trace element variance is broadly displayed as the ratio between elements with different partitioning coefficients. Normalized ratios between highly incompatible light rear earth elements (LREE) and moderately incompatible rear earth elements (MREE), for example La/Sm_N, can be used to represent the slope of the REE abundance, and is a common proxy for MORB enrichment and depletion.

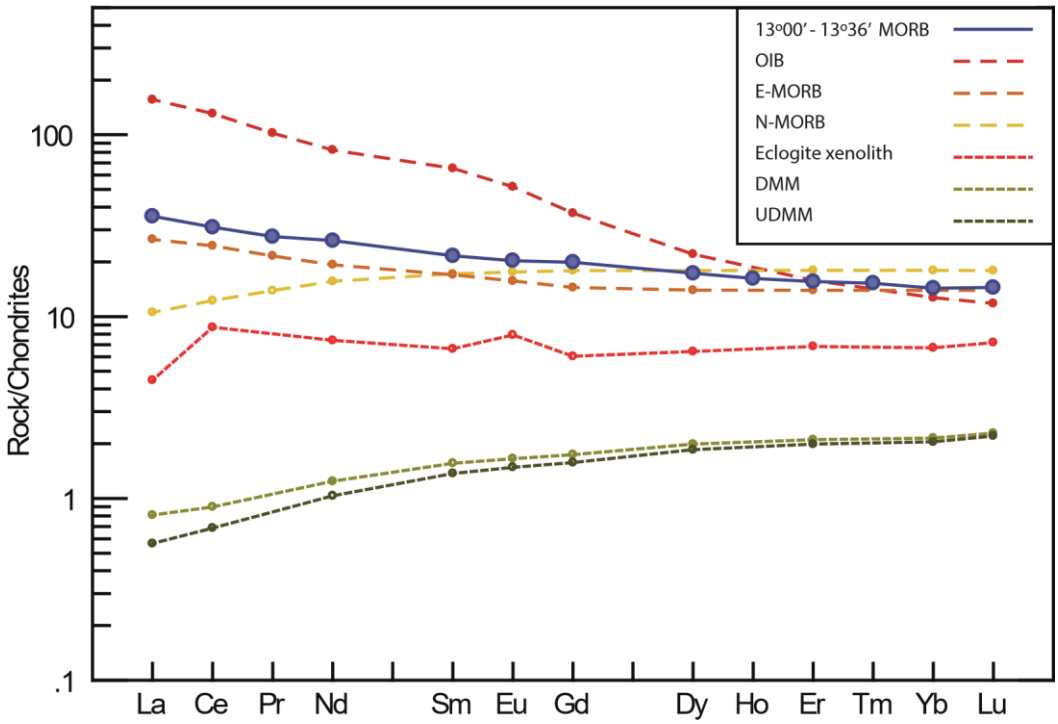

Figure 5: Abundance diagram for REE normalized to chondrite (Sun and McDonough 1989). Data for the average MORB from 13°00' – 13°36'N of the Mid-Atlantic Ridge is from this study and from Wilson, Murton et al. (2013) . Average Ocean Island Basalt (OIB), enriched MORB (E-MORB), and normal MORB (N-MORB) (see section 5.2 for definition of N-MORB and E-MORB) from Sun and McDonough (1989). Eclogite xenolith composition from Jacob and Foley (1999). Average depleted MORB mantle (DMM) and ultra-depleted MORB mantle (UDMM) from Workman and Hart (2005).

2.2.2 Magmatic processes

Isolating geochemical signals attributed to melting- and post-melting processes is essential when evaluating mantle geochemistry. Owing to their variable behaviour in the presence of two phases, trace elements are readily used as petrogenetic indicators.

At the onset of melting, melts may be instantaneously removed (fractional melting) or they may remain in equilibrium with the residual rock (batch melting) (Plank and Langmuir 1992). The modal equilibrium melting equation (equation 1.2, Appendix 4) represent a simplistic model for mantle melting. It is, however unrealistic to assume that the bulk partition coefficient remains constant throughout the melting region, as proportion of mineral phases tend to change due to exhaustion of most fusible phases (*e.g.* clinopyroxene) or in accordance with pressure changes (*e.g.* garnet to spinel in peridotite). A polybaric melting model is therefore a more realistic illustration of melting beneath MOR (Klein 2003, Koornneef, Stracke et al. 2011). Rather than

representing melts equilibrated with the mantle at one specific pressure and composition, the bulk melt composition reflects the sum of compositions from a range of depths and concentrations.

Another fundamental control on trace element fractionation is the extent of melting, *F (*equation 1.2 and 1.3, Appendix 4). The smaller the melting extent, the more significant is the fractionation between elements with different bulk partition coefficients. At large extents of melting, the fractionation between elements with different compatibilities becomes progressively less significant, and trace element ratios virtually reflect those of the mantle source. Contrastingly, at the onset of melting, (*i.e.* at the highest pressures of the melting region), $F \sim 0\%$. Melts produced here experience maximum element fractionation (Stracke and Bourdon 2009), and are thus expected to be extremely enriched in highly incompatible elements (Langmuir 1992, Forsyth and Langmuir 2007).

Certain trace elements behave unambiguously in specific mineral phases. For example, owing to large contrast in partitioning behaviour between MREE and HREE in garnet compared to spinel, the presence of garnet in a melting residue will cause significant MREE/HREE fractionation. At depths higher than 85 km, spinel becomes unstable in peridotite and is replaced by garnet (Robinson and Wood 1998). Hence, MREE - HREE fractionation provides valuable estimates of peridotite solidus depths. It is worth noting that garnet bearing eclogite/pyroxenite melts are expected to display similar HREE depletions (Hirschmann and Stolper 1996)

Extreme trace element and isotopic enrichment reported for melt inclusions relative to their host rock (Sobolev, Hofmann et al. 2000, Maclennan 2008) suggest significant averaging of final melts from primitive melts (Stracke and Bourdon 2009). The extent to which primitive melt compositions are preserved in basalts is strongly affected by the extent of melt mixing, and melt-rock interaction. Complete mixing of melts throughout the melting region will average the trace element composition. Alternatively, incomplete mixing of polybaric melts and/or melts derived from a heterogenous mantle may produce a range of incompatible trace element signals (Stracke and Bourdon 2009, Koornneef, Stracke et al. 2011). Spreading rate, and thus also magma production and melt extraction rate is believed to be crucial for the magnitude of melt mixing (Rubin, Sinton et al. 2009). The degree of melt-rock reaction, and the rate of melt extraction

reflect size and permeability of the melting channels (Plank and Langmuir 1992, Kelemen, Hirth et al. 1997).

As melts ascend towards the surface and progressively cool, new minerals (olivine, plagioclase, and pyroxene) will crystallize. Elements are incorporated into minerals according to their bulk partition coefficients (equation 1.1, Appendix 4). This means that incompatible elements are largely retained in residual melts during differentiation. It follows that the effect of fractional crystallization is most obvious for ratios between incompatible and compatible trace elements, and negligible for ratios between elements of similar compatibility (Hofmann 1988, Klein 2003). Although influenced by source composition and melting processes, the variance in compatible major elements generally observed in MORB is mostly attributed to shallow level fractional crystallization (Klein 2003).

Major element variance associated with fractional crystallization is often displayed as MgO or Mg# (molar Mg/ (Mg + Fe^{2+}), and the corresponding variance in other oxides (*e.g.* K2O, Al2O3, FeO) is indicative of the phase being crystallized. The order of phase crystallization in mantle derived melts is: (1) olivine + spinel or garnet, (2) plagioclase, and (3) pyroxene (Klein 2003). A gradual change in melt composition with decreasing Mg contents from the parental melt is indicated by the "liquid line of descend" (LLD).

2.2.3 Mantle heterogeneities

A consensus theory is that Earth's mantle is geochemically and lithologically heterogenous at various scales, reflecting several episodes of crust-mantle fractionation (Hedge and Walthall 1963, Tatsumoto, Hedge et al. 1965). This theory is essentially founded on isotopic ratios systematics observed in oceanic basalt suits (figure 6). Such ratios are expected to display a time-integrated differentiation rather than recent element fractionation (Hart 1986, Stracke 2012). Mixing trajectories observed in isotopic ratios suggest a heterogenous melt source at various scales.

The most depleted mantle component, so called Depleted MORB Mantle (DMM) (Andres, Blichert-Toft et al. 2004), is considered to be the result of mantle-crust differentiation. This process is believed to have left the DMM depleted in incompatible elements (Hart 1986). The

isotopic signature of the DMM is low $^{206}Pb/^{204}Pb$, $^{207}Pb/^{204}Pb$, $^{206}Pb/^{204}Pb$, and $^{87}Sr/^{86}Sr$, and high $^{143}Nd/^{144}Nd$ and $^{176}Hf/^{177}Hf$. The DMM is, however not homogenously depleted. This is apparent from the range of radiogenic isotope ratios (Pb, Sr, Nd, and Hf) in MORB isolated from plume interference. This range is believed to reflect large-scale (10^3 km) geochemical domains in the depleted upper-mantle (Hamelin, Dosso et al. 2011). The theory has existed for decades (Dupre and Allegre 1983), and is attributed to long term isolation of different mantle domains (Hamelin, Dosso et al. 2011). Each mantle domain reflects different extent of upper-mantle depletion, different convective histories, and different involvement influence of recycled material (Hamelin, Dosso et al. 2011). An example of large-scale isotopic anomalies is the DUPAL anomaly in the southern hemisphere (Dupre and Allegre 1983, Hart 1984). Elevated ΔSr (ΔSr = $[^{87}Sr/^{86}Sr\text{-}0.7030] \times 10^4$) and deviation of $^{207}Pb/^{204}Pb$ and $^{208}Pb/^{204}Pb$ from the *Northern Hemisphere Regression Line* characterizes this province (Hart 1984).

It becomes clear from figure 6 that the variance in DMM fails to reproduce the global isotopic variance. The most extreme isotopic compositions are associated with mantle plumes (White 1985). Ocean Island Basalts (OIB) are more enriched in trace elements and isotopic ratios than MORB (figure 6). Because of this, the theory of mantle re-enrichment by recycled components has emerged. It is now generally accepted that Earth's mantle should be seen as a "marble cake" of enriched components enclosed by DMM (Wyllie 1970, Allegre and Turcotte 1986). Recycling- and reintroduction of enriched crustal material to the depleted mantle is a consensus theory (Stracke 2012, Kimura, Gill et al. 2016). According to this theory, oceanic crust, and lithosphere, as well as small amounts of continental material is incorporated into the mantle during subduction process. During high pressure subduction zone metamorphism, crustal material will be transformed to eclogite (Hofmann and White 1982, Hofmann 1997). Mantle convection is believed to produce a "stirred" upper mantle, consisting of eclogite veins enclosed by peridotite (Allegre and Turcotte 1986). Ultimately, the heterogenous mantle is a product of "convection-driven interaction between crust and mantle" (Stracke 2012).

Based on isotopic patterns, three universal end-members; the HIMU (High μ. *i.e.* high U/Pb ratio) and two distinctive, enriched mantle components (EMI and the EMII) have been recognized (Hart 1986, Sun and McDonough 1989). All components are believed to be old, isotopically evolved subducted material (Hofmann and White 1982). Different protolithic

compositions, subduction zone modifications, and recycling time are all factors expected to cause significant variance between recycled components (Kimura, Gill et al. 2016)

Several theories exist on the nature of the most common of enriched components, the EMI. Delaminated, subcontinental lithosphere, recycled oceanic crust, and subduction zone, metasomatized mantle wedge peridotite are likely candidates (Hauri and Hart 1993, Stracke 2012, Kimura, Gill et al. 2016). Influence of sediments is believed be most profound on the EMII component (Hofmann and White 1982, Hart 1988). A recent review of global variability in isotopic data has revealed a continuous transition from EMI and EMII (Stracke 2012). This is contradicting to the dichotomous EMI and EMII components suggested by Hart (1986). According to Stracke (2012), each EM basalt trend represent unique EM components rather than mixing between EMI and EMII. The more uncommon HIMU is characterized by abnormally high Pb isotopic composition. Selective removal of Pb relative to Th and U is believed to be the result of fluid-rock interaction. Although debated, a theory is that the HIMU component represent recycled oceanic crust which has been subjected to significand alteration and subduction zone dehydration (Hofmann and White 1982, Hauri and Hart 1993, Stracke, Bizimis et al. 2003, Stracke 2012, Kimura, Gill et al. 2016). An additional, less enriched component has been the subject of debate. This component appears to be the average of all enriched components. It was originally entitled "Prevalent Mantle" (PREMA) (Hart 1986), but has also been referred to as the "Focal Zone" (FOZO) (Hart, Hauri et al. 1992), and the "Common" (C) component (Hanan and Graham 1996). Several hypotheses regarding its origin have been proposed. Owing to the enriched isotopic composition of this component, it was originally suggested to represent the "primitive" lower mantle (Hart 1986). More recent studies argues that this component reflect a relatively uniform, solid-state mixture of different components (Stracke 2012).

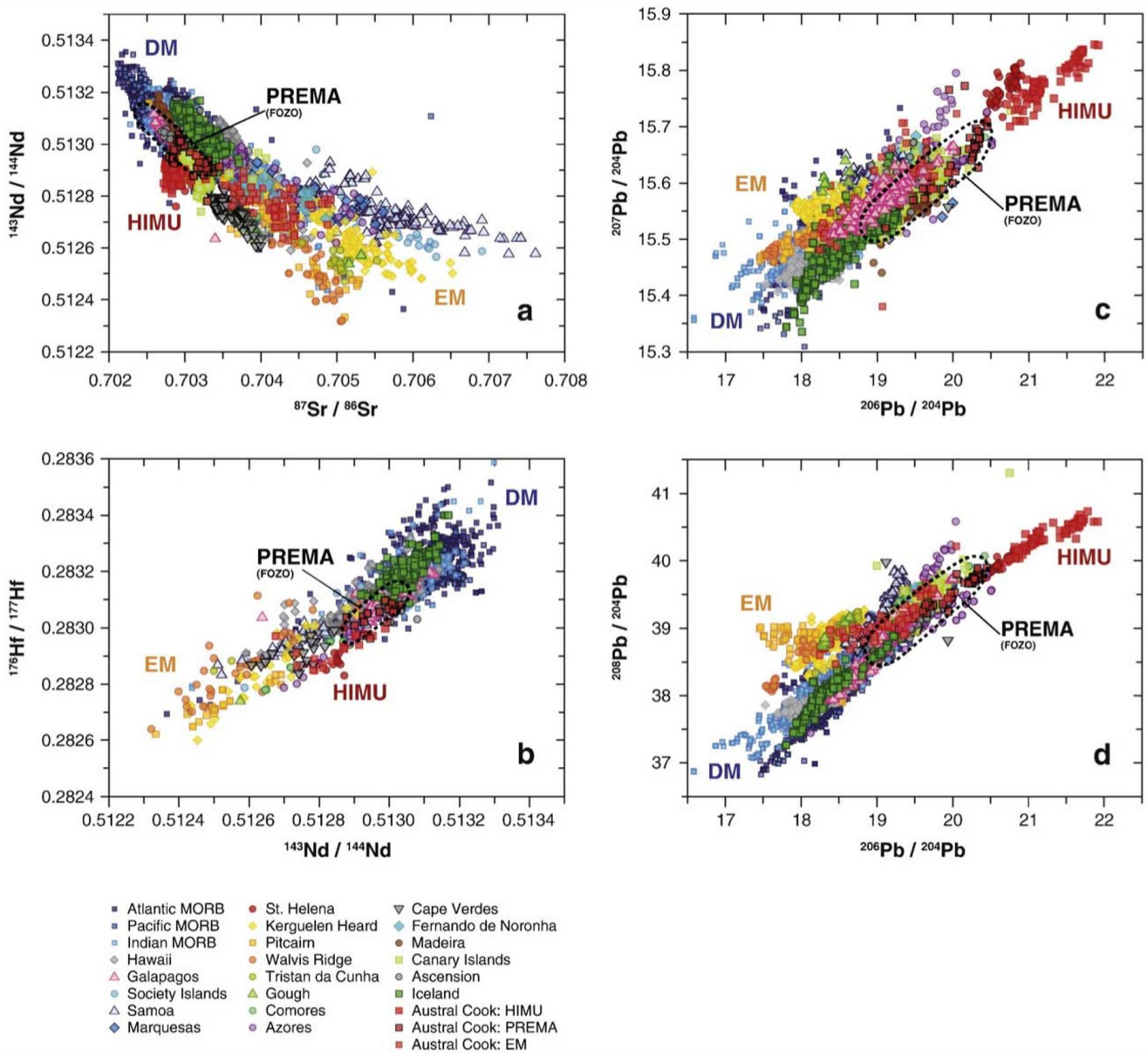

Figure 6: Global variability in isotopic composition. (a) $^{143}Nd/^{144}Nd$ versus $^{87}Sr/^{86}Sr$, (b) $^{143}Nd/^{144}Nd$ versus $^{176}Hf/^{177}Hf$, (c) $^{206}Pb/^{204}Pb$ versus $^{207}Pb/^{204}Pb$, (d) $^{206}Pb/^{204}Pb$ versus $^{208}Pb/^{204}Pb$. PREMA (FOZO or C) as defined by Stracke (2012). EMI and EMII have been generalized to EM. Plots from Stracke (2012).

3. Geological setting

3.1 The Mid-Atlantic Ridge

The Mid-Atlantic ridge, extending from the Gakkel Ridge in the north to the Bouvet Triple junction in the south, is among the longest volcanic chains on Earth, with a half spreading rate of ~25 mm/yr (Müller, Sdrolias et al. 2008). Major, deep (1 – 1.4 km) rift valleys bounded on each side by normal faults (20 – 40 km apart) characterizes the spreading center of this slow-spreading ridge (Smith 1998). The MAR is subdivided into segments (approximately 50 km along-axis), bound by transform faults (Sempéré, Lin et al. 1993).

The study area is located on the western flank of the MAR between 13°00'N and 13°36'N (figure 7), near the center of a segment bound to the north by the Fifteen-Twenty Fracture Zone (FTFZ) (15°20'N) and to the south by the Marathon Fracture Zone (MFZ) (12°40'N). It has been interpreted as particularly magma starved (Godard, Lagabrielle et al. 2008, Smith, Escartín et al. 2008). A complex tectonic history is assumed for this area, involving the evolution of the North American - South American – African triple junction (Smith, Escartín et al. 2008). Although situated far from any known mantle plume (Donnelly, Goldstein et al. 2004, Foulger 2010) this region, has been shown to present large geochemical variation (Donnelly, Goldstein et al. 2004, Hémond, Hofmann et al. 2006, Wilson, Murton et al. 2013).

The morphology along the ridge axis between the FTFZ and the MFZ alternates between faulted volcanic terrain and smooth, corrugated OCC (figure 7) (Smith, Cann et al. 2006, MacLeod, Searle et al. 2009). Similar patterns are observed away from the ridge axis (Smith, Escartín et al. 2008). Smith, Escartín et al. (2008) reported at least 24 OCC between 13°N and 14°N of the MAR, of which two were considered active. The presence of these large-scaled dome structures has led to a highly variable seafloor topography, ranging in depth from > 4000 meters to < 2000. Hydroacustic records has revealed high seismic activity in certain areas of this segment (from the FTFZ to ~14°35'N and from ~13°50'N to the MFZ), indicating robust tectonic activity (*i.e.* high A_t) (Smith, Cann et al. 2006). Escartin, Smith et al. (2008) reported a correlation between

hydrothermal sites, abundant seismicity, and asymmetric crust morphology (i.e. OCC), and attributed these characteristics to a distinctive mode of asymmetric, detachment fault accretion

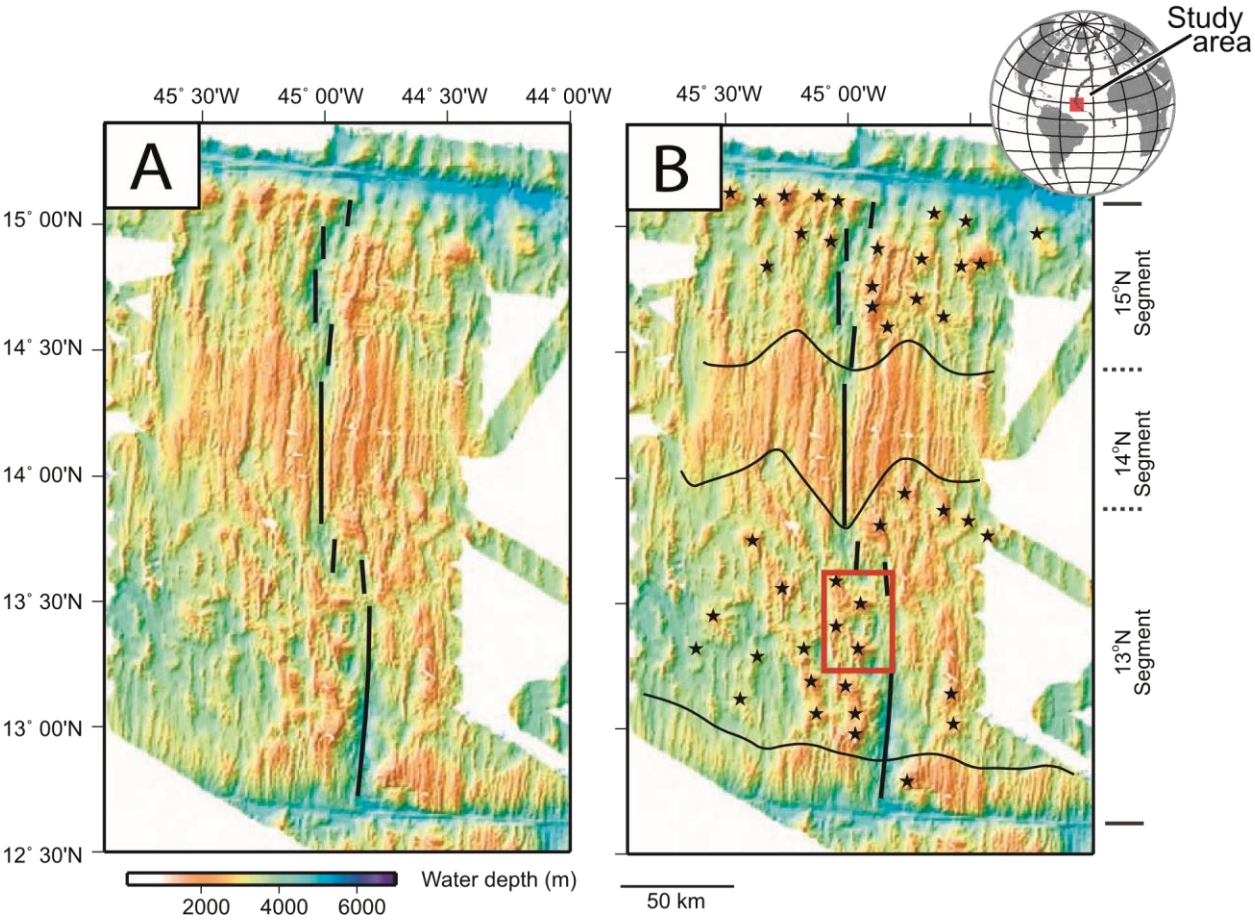

Figure 7: Bathymetry map of the MAR between Fifteen Twenty and Marathon fracture zones, with the bold black lines indicating the spreading axis. (b) similar as (a) but with stars pinpointing positions of OCC, light, black lines indicating the transition between A_t - And A_m- dominated segments. The study area is indicated in red. Figure modified from Smith, Escartín et al. (2008)

3.2 13º20'N and 13º30'N detachment faults

The focus of this study is on the detachment faults situated at 13º20'N and 13º30'N, on the western MAR flank (figure 7). Based on recent, high-resolution mapping of the study area, detailed descriptions of both detachment faults and the surrounding seafloor is available in the literature (Escartín, Mével et al. 2017). From here on, the detachment faults located at 13º20'N and 13º30'N will be referred to as OCC20 and OCC30 respectively. Along axis, OCC20 is ~7 km wide and OCC30 ~12 km wide. In the spreading direction OCC20 extend for ~5.5 km and

OCC30 for ~8 km. Assuming half-spreading rates of ~12 mm/yr, Escartín, Mével et al. (2017) estimated the ages of OCC20 and OCC 30 to be ~0.5 and ~0.7 Ma respectively. When initially described, both detachment faults were categorized as active tectonic features (Smith, Cann et al. 2006). In the most recent evaluation of these faults, the OCC30 is argued to be inactive or at the verge of termination (Escartín, Mével et al. 2017). This interpretation is based on high-angle normal faults truncating the OCC30 front area, indicating renewed strain distribution (MacLeod, Searle et al. 2009, Escartín, Mével et al. 2017).

In order to constrain the evolution of detachment faults, previous studies have subdivided OCC into morphologically similar domains (Smith, Cann et al. 2006, MacLeod, Searle et al. 2009, Wilson, Murton et al. 2013, Escartín, Mével et al. 2017). Based on micro bathymetry data, *in-situ* observations, and rock sampling, Escartín, Mével et al. (2017) divided the OCC20 and OCC30 into morphological domains; (1) *the chaotic terrain*, (2) *the corrugated surface*, and (3) *the hanging-wall cutoff*. The remaining seafloor has been identified as (4) *axial valley floor*, and (5) *inter-OCC seafloor* (figure 8). The axial valley floor constitutes the oceanic crust east of the transition to the neovolcanic zone, whereas the inter-OCC seafloor covers the area west of this transition (apart from the OCC) (figure 8). A thorough description of these different domains can be found in Escartín, Mével et al. (2017). The principle observations from these descriptions will be summarized here.

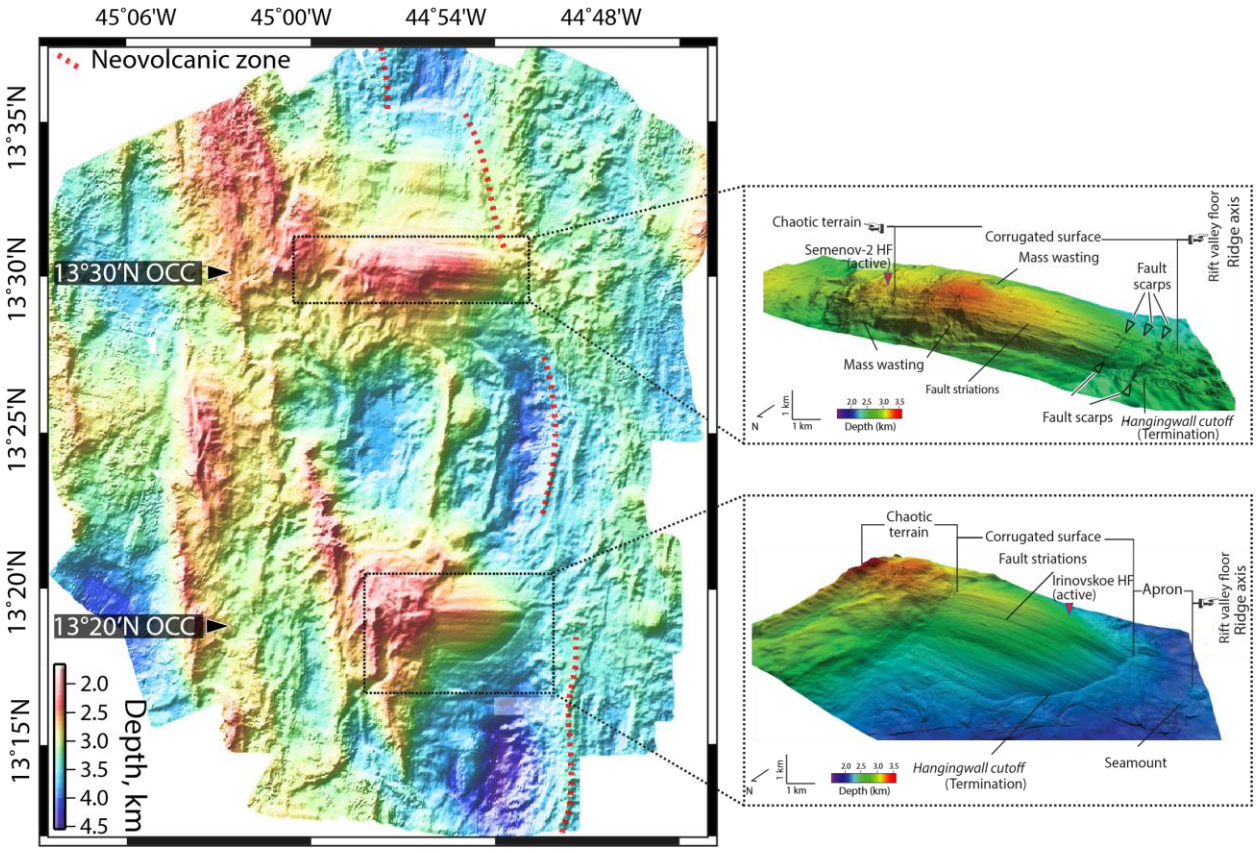

Figure 8: Bathymetry maps of the 13º00' – 13º36'N area outlining OCC20 and OCC30 (right). The chaotic terrains, corrugated surfaces, and hanging-wall cutoff is indicated in outlined 3D maps of the OCCs. Dotted, red line indicates the transition to the neovolcanic zone (east). Except for the OCC20 and OCC30, everything west of this transition falls within the inter-OCC domains. Figure modified from Escartín, Mével et al. (2017).

The chaotic terrain comprises the west-end of the detachment faults. It is bounded by linear ridges, which are interpreted as the high-angle normal faults. Small fault scarps, basaltic talus, hydrothermal deposits, and sometimes steeply dipping *in-situ* basalt characterize the chaotic terrain. This domain extends from the base of the linear ridges to the west-end of the corrugated surface (figure 8). The OCC20 and OCC30 chaotic terrains extends ~3.5 km and ~5 km in the spreading direction respectively. OCC20 appears more elevated than OCC30, with a continuous dip towards the ridge axis. MacLeod, Searle et al. (2009) argued that this morphologically diverse area was the result of tectonic disruption of the oldest part of the corrugated surface. Escartín, Mével et al. (2017) on the other hand suggested that this terrain represented extensive mass waste from previous fault scarps, which have been demolished from the east-facing ridge flank. This mass wasting from initially-steep slopes is effectively reducing the initial fault scarp angle.

The corrugated surfaces stand out as striking, relatively smooth domes in both OCC20 and OCC30. Corrugations or striations are observed at different scales. Large scale corrugations are reported with amplitudes of ~ 100 m. Strain localization is believed to be the dominating factor controlling the formation of these striations. The corrugated surfaces are elevated compared to the surrounding seafloor, indicating large rotation of low-rigidity footwalls (Smith, Cann et al. 2006, Ciazela, Koepke et al. 2015). Corrugations are believed to reflect uneven strain localization and interaction between the ductile footwall and the rigid hanging-wall as the latter slides along the former during footwall rotation (Smith, Cann et al. 2006, Escartín, Mével et al. 2017). As evident from figure 8, the OCC20 appears less affected by recent normal faulting. Furthermore, the transition between the chaotic terrain and the corrugated surface is gradual and sub-horizontal in OCC30 compared to the abrupt transition in OCC20. The corrugated surface of this detachment is covered by a near continuous layer of basaltic breccia and sediments and intervals of larger scale moats. These features are interpreted as slump deposits from the adjacent hanging-wall cutoff (Escartín, Mével et al. 2017). Fresh pillow basalt and diabase dykes have been reported at the termination of OCC30, indicating recent volcanism in this area (Escartín, Mével et al. 2017). Hydrothermal deposits are more abundant in the sediment blanket of the OCC30 corrugated surface. These deposits imply significant hydrothermal circulation (MacLeod, Searle et al. 2009, Escartín, Mével et al. 2017)

The hanging-wall cutoff or termination is the elevated area between the corrugated surface and the ridge axis (Ciazela, Koepke et al. 2015). This domain is regarded as a thin, wedge of unconsolidated matrix dominated by hanging-wall deposits (Escartín, Mével et al. 2017). In the OCC20 termination, the hanging-wall cutoff is distinctive, with a laterally continuous trench and a gently dipping slope. This contrasts with the OCC30 emergence zone, which is disrupted and irregular.

Volcanic seafloor prevails in front of both detachment faults (from the hanging-wall cutoff towards the ridge axis) (figure 8). The volcanic texture of this domain includes hummocks, volcanic cones, and modest normal faulting, and is interpreted to be more recent than the hanging-wall cutoff (Escartín, Mével et al. 2017). The age of this volcanic seafloor is inversely

proportional to the backscatter intensity of side-scan sonar images. High backscatter suggests recent volcanic emplacement. The axial valley floor situated immediately in front of the OCC20 apron displays significantly lower backscatter than that of the northern- and southern axial valley floor, indicating that this volcanic crust is more recent (MacLeod, Searle et al. 2009, Mallows and Searle 2012).

Linear ridges and deep basins characterize the remaining study area. These features are interpreted as crests of high-angle, normal faults, and are likely to be precursors for future detachment faults (Smith, Cann et al. 2006). A prominent linear ridge extending from the north end of OCC20 to the south end of OCC30 is reported to host a flat-topped seamount (~2 km in diameter and 350 m high) (Escartín, Mével et al. 2017). Escartín, Mével et al. (2017) argued that the discrepancy in rotational angle of the normal fault (~15^{o}), the horizontal top of the seamount, and the thin sediment layer covering it were all evidences that this volcanic feature was emplaced sometimes after the fault rotation.

4. Methodology

4.1 Sampling

This study includes 63 new major element analyses, 65 trace element analyses carried out at the University of Nantes, as well as 4 trace element analyses and 20 isotopic ratios measured at the University of Bergen is included to the dataset. Details on sample name-, location, and institute of analytical facilities are given in table A1b (appendix 1). Furthermore, this new dataset has been compiled with major-, trace element -, and isotopic analyses from Wilson, Murton et al. (2013).

Because the main objective of this study is to constrain the relationship between geological structures and chemical signals, lava samples from the area have been separated into groups according to the morphological domains defined by Escartín, Mével et al. (2017) (figure 8). Samples presented here have been given symbols according to the morphological domains described in section 3.2 (figure 9). From here on, the following abbrevations will be used when

referring to these morphological domains: *CT* (Chaotic Terrain), *CS* (Corrugated Surface), *HC* (Hanging-wall Cutoff). Hence, abbreviations for the OCC20 sub-groups are *OCC20-CT*, *OCC20-CS*, and *OCC20-HC*, and *OCC30-CT*, *OCC30-CS*, and OCC30-HC for the OCC30 sub-groups (figure 9). The remaining seafloor has been separated into the following morphological domains: *NF* (Normal Fault, for the volcanic, fault disrupted, inter-OCC seafloor), *SM* (SeaMount. Samples associated with a large, flat-topped, cone shaped structure situated in a normal fault graben in the inter-OCC terrain), *AV* (Axial Valley samples). All samples presented are lavas. The majority of ODEMAR samples were collected by a ROV, and the remaining samples were collected by dredging (table A2, appendix 1). Dredged samples and samples collected from the detachment faults were loose rocks, whereas the remaining samples were *in-situ*.

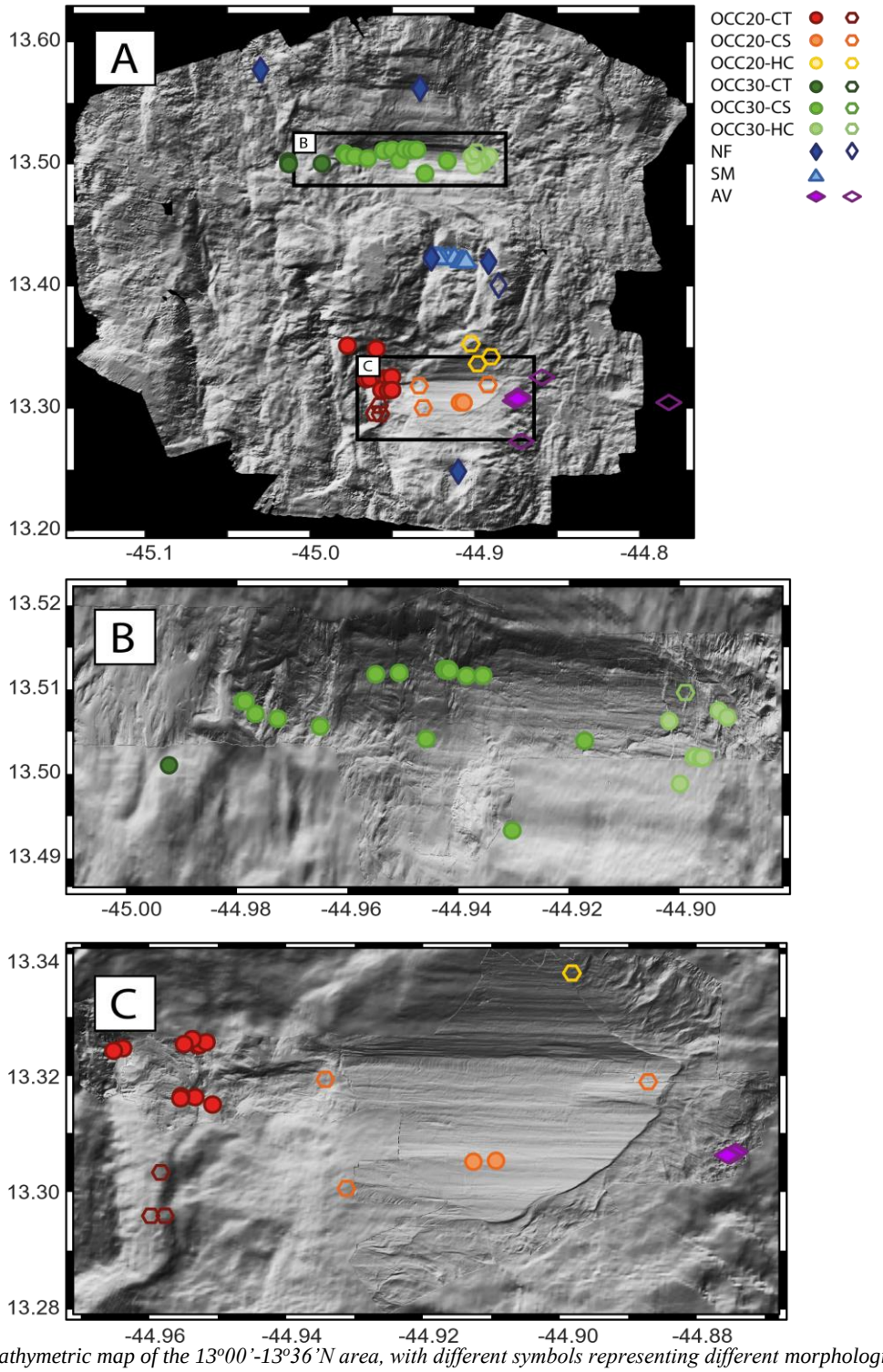

Figure 9:(a) Bathymetric map of the 13º00'-13º36'N area, with different symbols representing different morphological domains. Closed symbols represent data presented in this study. Open symbols represent dredged samples form Wilson, Murton et al. (2013). (b) Micro-bathymetry map of the 13º30'N OCC (OCC30). (c) Micro-bathymetry map of the 13º20'N OCC (OCC20).

4.2 Sample preparation

In this study, 20 basalt samples collected during the ODEMAR cruise have been analysed for Sr- and Hf isotopic ratios, 19 for Pb-isotopic ratios, and 11 for Nd isotopic ratios. In addition, 4 samples have been analysed for trace elements. Preparation and analysis of these samples were conducted at Bergen Geoanalytical Facility (BGF), University of Bergen.

4.3.1 Physical preparation

For all samples analysed at the BGF, a diamond saw was used to remove altered material and obtain fresh rock samples. Each individual sample was then crushed. To avoid external contamination, the sample was sealed in robust plastic bags during this preparational step. After crushing, sample fragments were sieved to fractions ranging from 1 mm to 0.5 mm. Further, grains devoid of phenocrysts and cutting surfaces (from the diamond saw) were handpicked using a stereomicroscope. For samples containing glassy crust (table A1b, appendix1), fresh glass fragments were prioritized over whole-rock fragments. Approximately 1 g of material was obtained for each sample. Whole-rock samples were pulverized using an agate mill. Glassy samples were not pulverized. To prevent contamination, all instruments and tools were cleaned by compressed air, ethanol, and water between each sample preparation. The physical preparation steps have been summarized in figure 10.

4.3.2 Chemical procedure

All chemical preparations were carried out in a class 1000 air filtered clean laboratory to minimize the contamination. All dilutions were made using ultrapure (18.2 MΩ·cm) water, and all labware were acid-washed prior to chemical preparation. The chemical repreparation done for isotopic analyses is elaborated in the following. Pulverized, whole-rock samples (see table A1b, appendix 1) were then subjected to acid leaching. Compared to Hf and Nd, Pb and Sr isotopes are notably sensitive to nonmagmatic contamination (*e.g.* fluid-rock interaction, storage, and sample preparation) (Nobre Silva, Weis et al. 2010, Todd, Stracke et al. 2015). To obtain isotopic ratios that reflect igneous signals exclusively, it is necessary to remove the effects of

contamination and alteration by acid leaching. The acid used for leaching was 0.5 M HCl (1 ml per pulverized sample). Leached powders were then cleaned in an ultrasonic bath for 10 minutes. The leachate solution was decanted from the settled powder immediately after the ultrasonic bath. The purpose of this step to was remove nonmagmatic particles (*e.g.* dust) and fluoride coating on the grains and hence ease the forthcoming breakdown of silicates (Todd, Stracke et al. 2015). Subsequently, the leached powders were dried on a hot plate over night at ~ 100^{o}C. As the hand-picked glass fragments were considered unaltered, the leaching procedure described above was not performed on glassy samples. Instead, 47% HBr was added to and decanted from these samples upon dissolution.

When dried, approximately one third rock powdered and glass chips (~ 0.3g) was transferred to individual screw-top Savillex moulded PFA vials (rounded interior). Whole-rock powders were dissolved in 28 M HF in a 3:1 volume mixture of HF-HBr (47% HBr and 28 M HF). When digested, after being left on a hot plate with the temperature of ~80^{o} C for 48 hours, samples were evaporated to dryness at ~ 135^{o}, and re-dissolved in 0.5 M HNO_3. This step was carried out three times.

Ion-exchange chromatography was used to isolate Pb-, Sr-, Nd-, and Hf-isotopes from the same solution. Single-element solutions are essential in isotopic ratio analysis, as interference from unwanted isotopes (*i.e.* isobaric interferences) may significantly bias the isotopic signal. The principle behind ion-exchange chromatography is to introduce the sample to two immiscible different phases; (1) a mobile phase, and (2) a stationary phase, to which the different components of the analytes have different affinities (Luqman (2012), p. 1). To isolate individual ions from their matrix, it is crucial to use an acid (*i.e.* mobile phase) to which the targeted ion and the matrix have contrasting affinities. This way, the targeted ion may be retained in, or released from the resin (stationary phase).

In this study, chemical separation of Pb, Sr, Nd, and Hf was carried out in four different ion exchange columns. The steps for all ion exchange separations carried out here was are shown in figure 10. As Pb is believed to be highly susceptible to external contamination (Todd, Stracke et al. 2015), this element was separated first. The Pb extraction followed protocol from Manhes, Minster et al. (1978). The sample solution loaded on the Pb-exchange column in a 0.5 M HBr (10 drops) solution. Pb was eluted from a AG1-X8 anion resin with 6 M HCl (25 drops), and the

matrix was eluted with 0.5 M HBr. During this separation step, one sample (ODM-DR13-01-12) was lost.

After Pb-separation, the remaining elute, containing Hf, Sr, REE, and the matrix was evaporated to dryness and redissolved in 6 M HCl three times. This material was re-dissolved in a 1 ml solution of 0.5 M HCl and 0.15 M HF and transferred to a new column. Following the procedure of Hamelin, Bezos et al. (2013), using the AG50W anion exchange resin, Hf and Ti were eluted with 0.5 M HCl and 0.15 M HF (1.5 ml). Sr was eluted with 2.5 M HCl (5 ml), and the REE were eluted with 6 M HCl (5 ml). These three elements were collected into three different vials for further purification.

Vials containing the Sr-fraction were evaporated to dryness, redissolved in 3 M HNO_3 and loaded onto Sr-exchange columns containing Sr-Spec resin. Sr was eluted by water after all other products had been eluted by 3M HNO_3.

Hf-Ti separation followed the procedure described in Hamelin, Bezos et al. (2013), using the LN-spec resin. Vials containing the Hf-fraction were evaporated to dryness and redissolved in 6 M HCl. Samples were then loaded onto the Hf-exchange columns. Ti was eluted by a mixture of 6 M HCl and 10 µl H_2O_2, and Hf was collected after adding 2 M HF to the resin. This procedure was repeated to a second time to ensure complete separation of Hf from Ti. A portion of the Hf-elute was lost during collection of sample ODM-ROC-V550-160.

The vials containing the Nd-fraction from the Hf-Sr-REE separation was evaporated to dryness and taken up in 0.3 ml of 0.25 M HCl. The Nd extraction followed instructions from Hamelin, Bezos et al. (2013),using LD-spec resin. Elution of Nd was carried out by adding 0.3 M HCl (2 ml) to the Nd-exchange columns.

4.3 Mass spectrometry and data reduction

Trace element-, and isotopic ratio were measured by means of mass spectrometry. The principle of mass spectrometry is to separate ions by their mass-to-charge ratios and measure the electric signal for in collectors. Four principal components constitute a mass spectrometer; (1) a sample introduction system, (2) the ion source (3) the analyser, where ions are separated according to mass-to-charge ratio, and (4) ion detectors (Stroobrant 2007). Although the same principles hold

for all mass spectrometers, the components and the configuration of components vary from one instrument to another. A summary of the different analyses performed in this study and their corresponding mass spectrometry techniques is given in table 1.

4.3.1 Trace element measurements

Trace elements were measured using a Thermo Scientific Element XR Inductively Coupled Plasma Mass Spectrometer (ICP-MS). This instrument is equipped with an inductively coupled plasma (ICP) ion source, a reverse Nier-Johnson configuration, and a single secondary electron multiplier (SEM)- ion counting systems.

4.3.2 Pb, Nd-, and Hf-isotopic measurements

Pb-, Nd-, and Hf-isotopes were measured using the multi-collector inductively coupled mass spectrometer (MC-ICP-MS) Nu Instrument Plasma II. The Plasma II is equipped with an ICP ion source. This instrument is equipped with multiple detectors (18 fixed faraday cups) and operates with a normal Nier-Johnson configuration.

4.3.3 Sr isotopic measurement

Sr isotopes were measured using a Thermal Ionization Mass Spectrometry (TIMS), Finnigan MAT262. Unlike the Thermo Scientific Element XR and Nu Plasma II, the Finnigan MAT262 is equipped with a thermal ionization (TI) ion source. This instrument consists of a normal Nier-Johnson mass-spectrometer and multi-collecting detector (9 faraday collector and two SEM amplifiers).

Table 1: Analyses done at the BGA and corresponding mass spectrometers with details on the ion source and detector of these instruments.

Instrument	Name	Ion source	Detector	Analysis
ICP-MS	Thermo Scientific Element XR	ICP	Single collector	Trace elements (including REE)
MC-ICP-MS	Nu Plasma II	ICP	Multi collector 16 Faraday cups	$^{206}Pb/^{204}Pb$ $^{207}Pb/^{204}Pb$ $^{208}Pb/^{204}Pb$ $^{143}Nd/^{144}Nd$ $^{176}Hf/^{177}Hf$
TIMS	Finnigan MAT 262	TI	Multi collector 9 Faraday cups	$^{87}Sr/^{86}Sr$

4.3.4 Mass fractionation correction

Due to difference in bond strength, some isotopes are more prone to ionization than others. The extent to which an element is ionized is mass dependent, that is, heavier isotopes are less prone to ionization than lighter isotopes (Becker 2007). Some isotopic fractionation can thus be expected to occur during mass spectrometric analysis. A result of this is deviation of measured ratios from true ratios (Jakubowski, Prohaska et al. 2011). The extent of mass fractionation differs for different instruments as a function of their ionization potential. Owing to difference in ion sources and ionization efficiencies, the extent of mass fractionation is more significant in ICP-MS than in the TIMS.

To achieve accurate isotopic ratio when using mass spectrometry, it is essential to correct for instrumental mass fractionation. The rationale behind those corrections is to determine a correction factor, from which true isotopic ratios can be estimated. The correction factor is determined by using a pair of stable isotopes from each isotope system. Stable isotope pairs exist for Sr-, Nd-, and Hf isotopes, but for the Pb isotopic system the lack of a stable isotope pair calls

for a more complex approach. For Pb analyses, thallium (^{203}Tl and ^{205}Tl) is added to the solution as this isotopic system contains only one sable isotope (^{204}Pb).

All isotopic ratio measured at the BGF were also corrected for mass fractionation, by repeated measurements of standard solutions. Measured isotopic ratios were normalized to corresponding international standard values. An in-house standard was used as internal standard for ^{176}Hf/^{177}Hf analyses. Details on mass fractionation correction parameters are given in table 2.

Table 2: Mass fractionation correction parameters.

Isotopic ratio analysis	Internal standard	Number of standard measurements	Internal standard values (average)	International standard values
Pb	NBS-981 (Tl-doped)	23	^{206}Pb/^{204}Pb = 16.931±0.003 (2σ) ^{207}Pb/^{204}Pb = 15.482±0.005 (2σ) ^{208}Pb/^{204}Pb = 36.669±0.015 (2σ)	^{206}Pb/^{204}Pb = 16.9371 ^{207}Pb/^{204}Pb =15.49135 ^{208}Pb/^{204}Pb = 36.72132
Sr	SRM 987		^{87}Sr/^{86}Sr = 0.710233±8	^{87}Sr/^{86}Sr = 0.710240
Nd	JNdi	4	^{143}Nd/^{144}Nd = 0.512058±1	^{143}Nd/^{144}Nd = 0.512115
Hf	Hf-Norm	16	^{176}Hf/^{177}Hf = 0.282125±5	^{176}Hf/^{177}Hf = 0.282127 (corresponding to JMC475 ^{176}Hf/^{177}Hf = 0.282157)

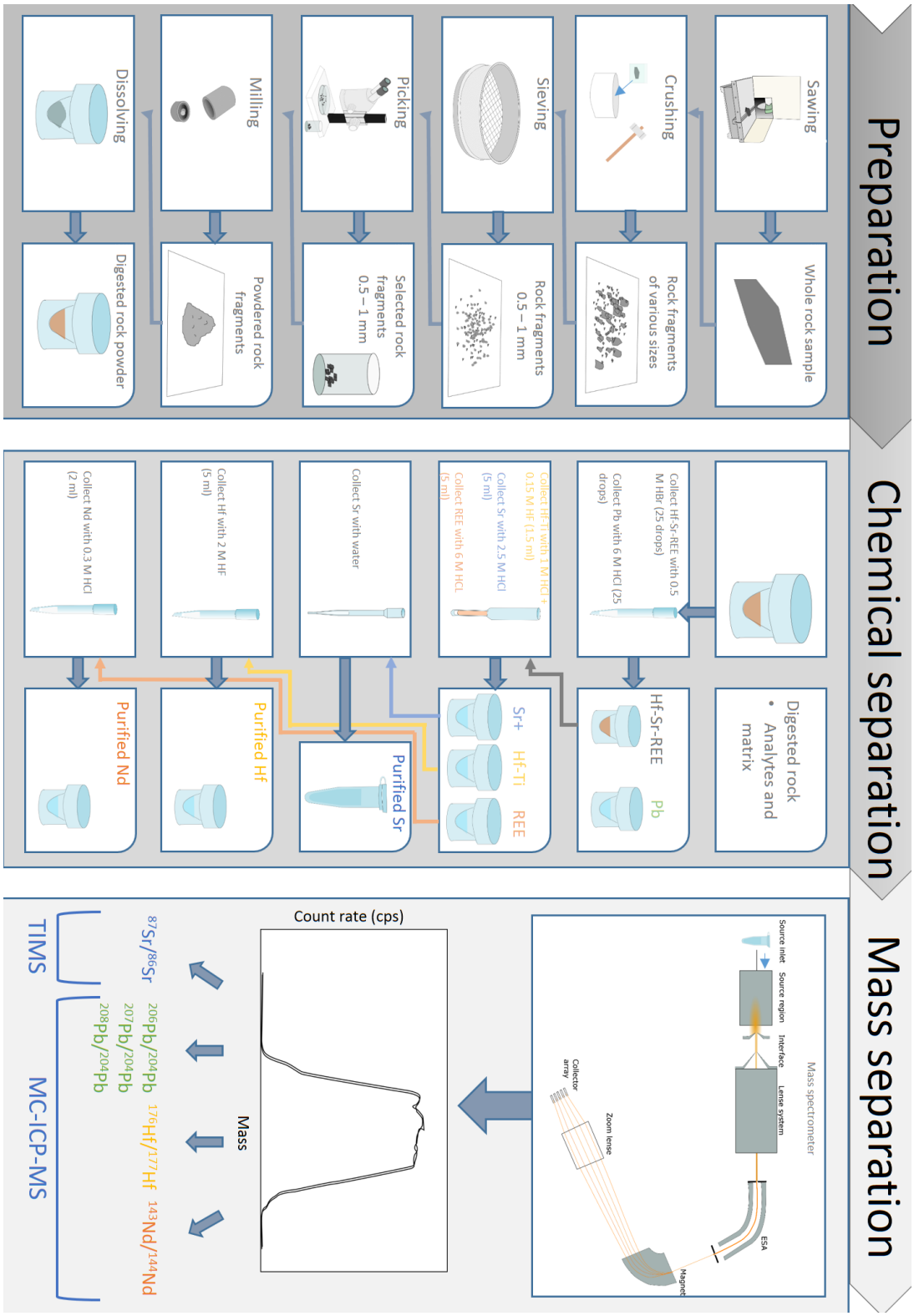

Figure 10: Schematic illustration of the main steps and sub-steps of work performed in this thesis, from physical preparation (left), through chemical preparation (middle) and finally isotopic ratio measurement (right).

5. Results

In the following sections, a description of the major- and trace element, and radiogenic isotopes (Pb, Nd, Sr, and Hf) systematic will be presented in terms of the morphological groups defined in chapter 3.2.

5.1 Major elements

As indicated in the TAS (Total Alkali Silica) diagram in figure 11, most samples from the 13º00'-13º36'N area form a continuous trend from low SiO_2 (~46 wt. %) low alkali (Na_2O + K_2O ~ 2 wt. %) basalts towards more basalt-andesitic (SiO_2 ~ 54 wt. % and Na_2O + K_2O ~ 3 wt. %). It appears, however that certain lavas deviate from this trend with elevated alkali contents for a given SiO_2 concentration. From here on these different trends will be referred to as the tholeiitic and alkaline trends respectively. Furthermore, two outlier samples (ODM-ROC-V544-055 and ODM-ROC-V546-097) have unusual compositions.

The morphological groups defined in the previous chapter largely overlap in major element variation. Nevertheless, some characteristics are common within each group. OCC20-CT lavas appear in both the tholeiitic and the alkaline trend. In the tholeiitic trend, they constitute the more andesitic end. Apart from one sample (D13-9), the OCC20-CS lavas all plot within the tholeiitic trend. OCC20-HC lavas are exclusively found in the tholeiitic trends. OCC20-CS- and HC lavas appear in the mid- to lower end of the tholeiitic trend. OCC30-CT appear similar as OCC20-CT, albeit with a subtle sample density. OCC30-CS samples are primarily found within more andesitic end of the tholeiitic trend. Exceptions are sample ODM-ROC-V546-097, which appears high in alkali (> 4 wt. %) for a low SiO_2 contents (~45 wt. %), and ODM-ROC-V559-374, which is low in both alkali (~ 2 wt. %) and SiO_2. OCC30-HC lavas display a similar pattern as OCC30-CS, with one outlier sample (ODM-ROC-V544-055). NF lavas appear similar to the OCC20-CS, OCC20-HC, OCC30-CS, and OCC30-HC lavas. The most SiO_2 poor NF samples are associated with the inter-OCC seamount. AV lavas display a wide range, plotting in both alkaline and tholeiitic trend. AV samples plotting in the lower end of the tholeiitic trend (ODM-ROC-V557- [098-101]) appear almost homogenous. SM samples are restricted to the lower end of the tholeiitic trend and display small variance.

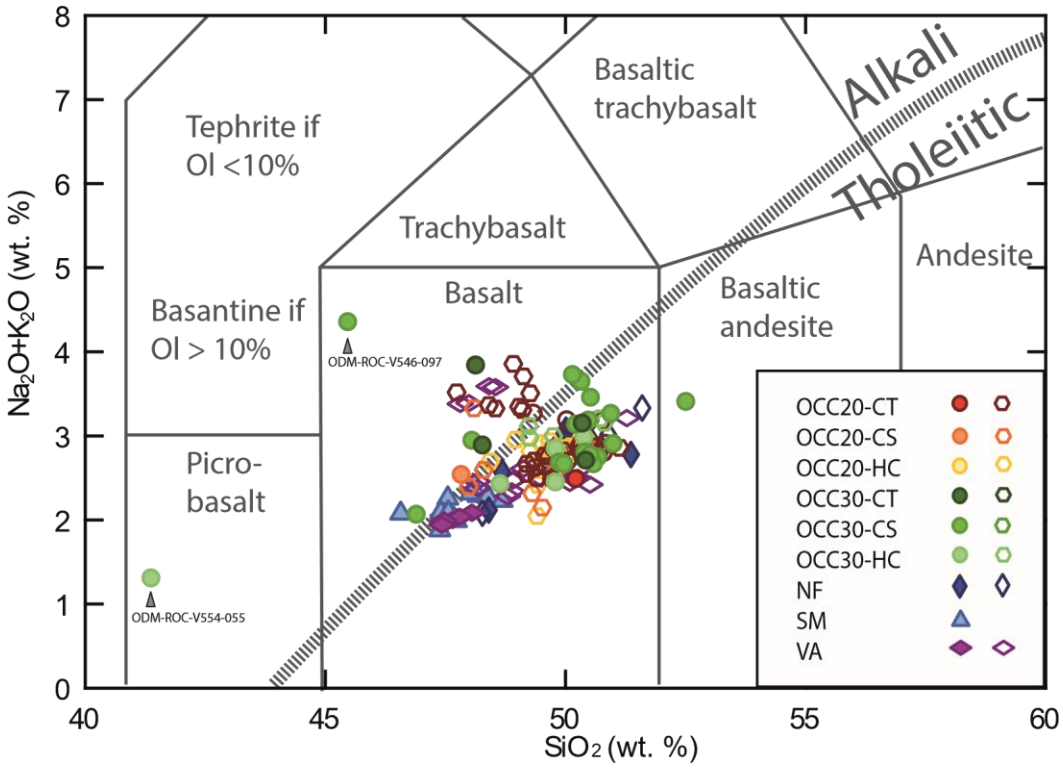

Figure 11: Total alkali versus silica (TAS) diagram for classifying volcanic whole-rocks, after Le Maitre, Streckeisen et al. (2002). Symbols are similar to figure 9. The dividing line distinguishes alkali basalt from tholeiitic basalt (from Sen (2014)). The overriding suite ranges from basalt to basaltic andesite, with SM and AV (sample 557- [098-101) constituting the lower end of the suite and OCC30-CS, NF and AV lavas constituting the higher end. Sample 559-374 (OCC30-CS) plots within the basaltic andesite field, whereas sample 544-055 (OCC30-HC) plots within the picro-basalt field. A selection of samples (OCC20-CT, OCC20-CS, OCC30-CT, OCC30-CS, and A) plots within the alkali basalt field. The most alkali sample is found in the OCC30-CS domain (sample 546-097).

Most samples are relatively magnesian. Indeed, a selection of lavas display abnormally high MgO (> 10 wt. %). Figure 12 is showing repartition of MgO (wt. %) for approximately 7000 global basalts collected along ridges. A plot displaying the MgO versus frequency of sample for the bulk MORB suite reveals a good normal distribution, with mean MgO 7.46 ± 0.9 wt.%. The 13º00'-13º36'N lava suite is notably skewed compared to the global distribution, and incorporates a significant proportion of highly magnesian (between 10 wt. % ≤ MgO ≤ 12 wt. %) basalts (figure 12). Distribution curve at 10 wt. % ≤ MgO ≤ 12 wt. % suggest extensive abundances of high-Mg lavas relative to global MORB. In the 13º00'-13º36'N area, more than 11% of the lava suite is highly magnesian. The most magnesian sample (ODM-ROC-V545-073) is found within the SM domain (Mg# = 70). These highly magnesian samples constitutes the low-end of the lava suit observed in TAS diagrams (figure 12).

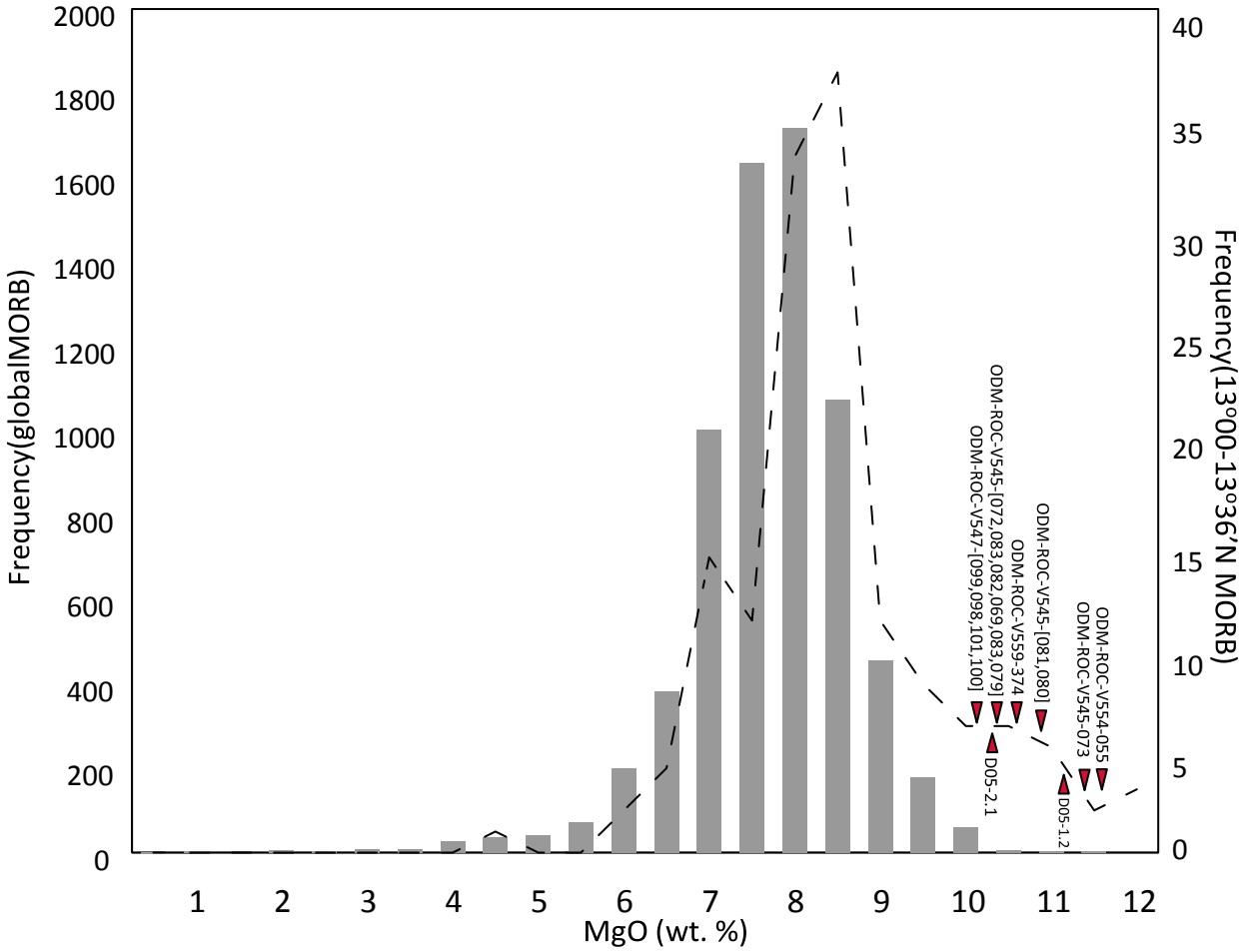

Figure 12: MgO (wt.%) versus sample frequency for MORB on a global scale (left axis) and from the 13°00'N – 13°36' N MAR (right scale). Global data was obtained from PetDB petrological database with the following criterions: glassy MORB, and is represented in this diagram by grey columns. Local data (from the 13°00'N – 13°36' N) includes data from this study and from Wilson, Murton et al. (2013), and is illustrated by a black curve.

Variation diagrams are convenient for examining the chemical evolution of melts. Most of the chemical variation in 13°00' – 13°36'N lavas is consistent with rest of the MAR lavas (figure 13). Nevertheless, there are some notable deviations from this classic, low-pressure fractional crystallization trends.

The majority of lava samples display a wide range in SiO_2 from 48 – 53 wt.% (figures 13 a). The most Mg-rich samples, however appear relatively restricted in terms of SiO_2 (46 – 48 wt. %). A similar pattern is seen in the MgO – Al_2O_3, K_2O, Na_2O, TiO_2, FeO_T plots (figure 13). Furthermore, the deviation towards more alkaline compositions for some samples (see figure 11)

is apparent in figures 13 c and 13 d, as well as in the MgO – TiO_2 plot (figure 13). The same samples appear also to be low Al_2O_3 and CaO. As in the TAS diagram, samples ODM-ROC-V544-055 and ODM-ROC-V546-097 display unusual compositions in the variation diagrams in figure 13.

OCC20-CT lavas primarily plot within the MAR MORB field. Exceptions are samples with more alkaline compositions (figure 13). Except for sample D13-9 (more alkaline), OCC20-CS- and OCC20-HC samples fall within the MAR MORB field. OCC30-CT and OCC-CS samples appear primarily within the MAR MORB field. However, each of these groups incorporate one alkaline sample. The ODM-ROC-V546-097 (OCC30-CS) outlier appears anomalously low in MgO in all variance plots (figure 13). OCC30-HC samples appear similar as OCC30-CS, albeit without any alkaline samples. The ODM-ROC-V544-055 outlier is highly magnesian, but deviate from the general MAR MORB trend in all variance diagrams (figure 13).

The Al_2O_3 – and CaO trends appear to increase as a function of decreasing MgO in the most Mg-rich lavas, whereas the remaining dataset display a corresponding decline in these oxides. It should be noted that certain samples (the alkaline samples addressed in figure 11) deviate from the overriding trend. Al_2O_3. Sample ODM-ROC-V559-373 (OCC30-CS group) deviate significantly from the rest of the sample set for all the oxides considered here.

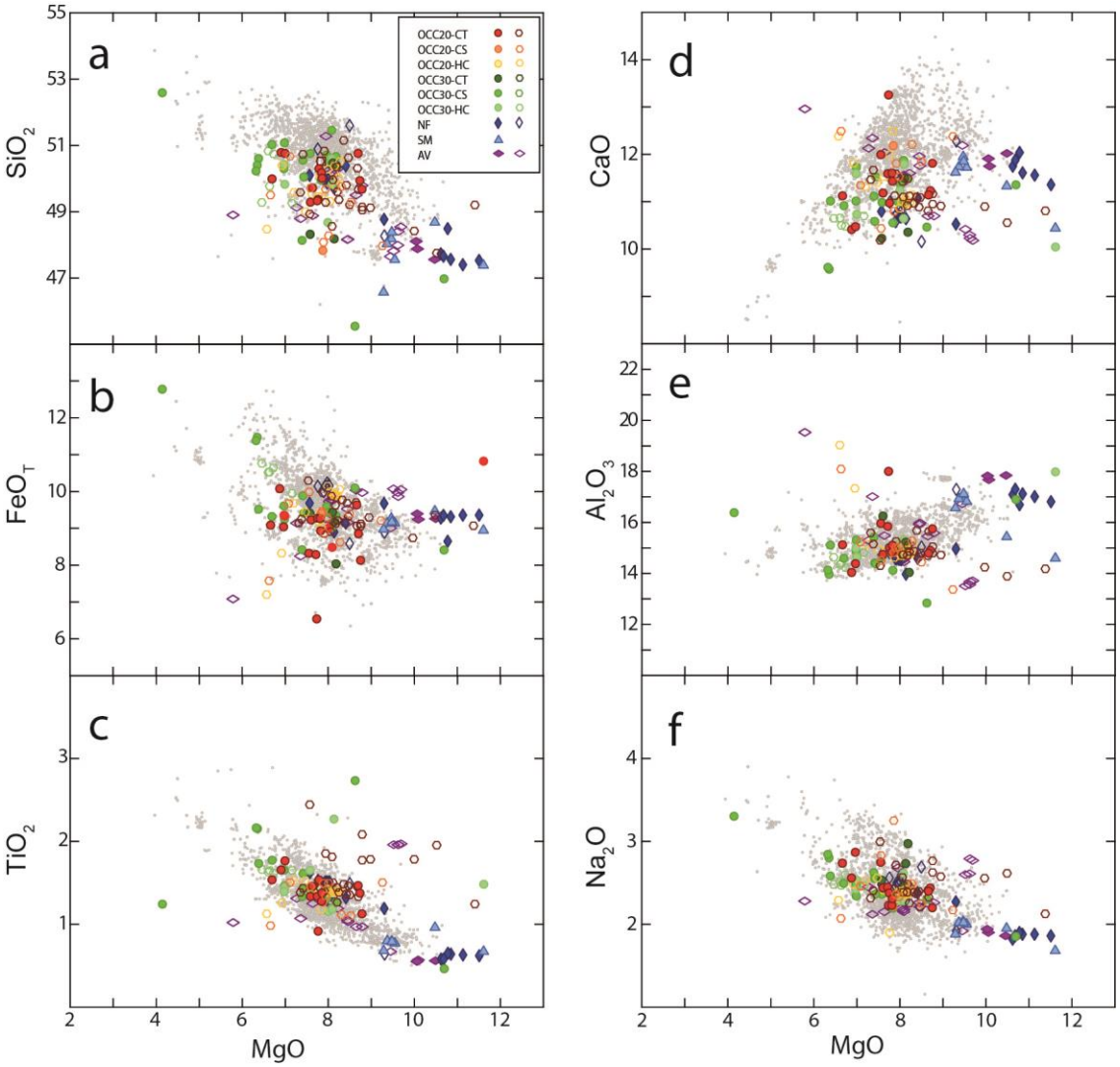

Figure 13:SiO_2 (a), FeO_T (b), TiO_2 (c), CaO (d), Al_2O_3 (e) and Na_2O (f) versus MgO. Filled - and open symbols represent data from this study and from Wilson, Murton et al. (2013) respectively. Smaller, grey symbol indicate all basalt samples (glass and whole rock) collected at spreading centers along the Mid-Atlantic Ridge (PetDB petrological database).

5.2 Trace elements

It becomes clear from figure 14 and 15 that the study area incorporates a large geochemical range. Despite the limited spatial extent of our sampling area our data show a geochemical range in LREE/MREE (La/Sm_N) and MREE/HREE (Gd/Yb_N) that is of the same order of magnitude as reported for the entire MAR (figure 14 a and b). The ratio between La/Sm_N ranges from depleted (~ 0.7) to enriched (~ 2.9), and is most extreme at ~13º20'N and ~13º30'N (figure 14 d and b).

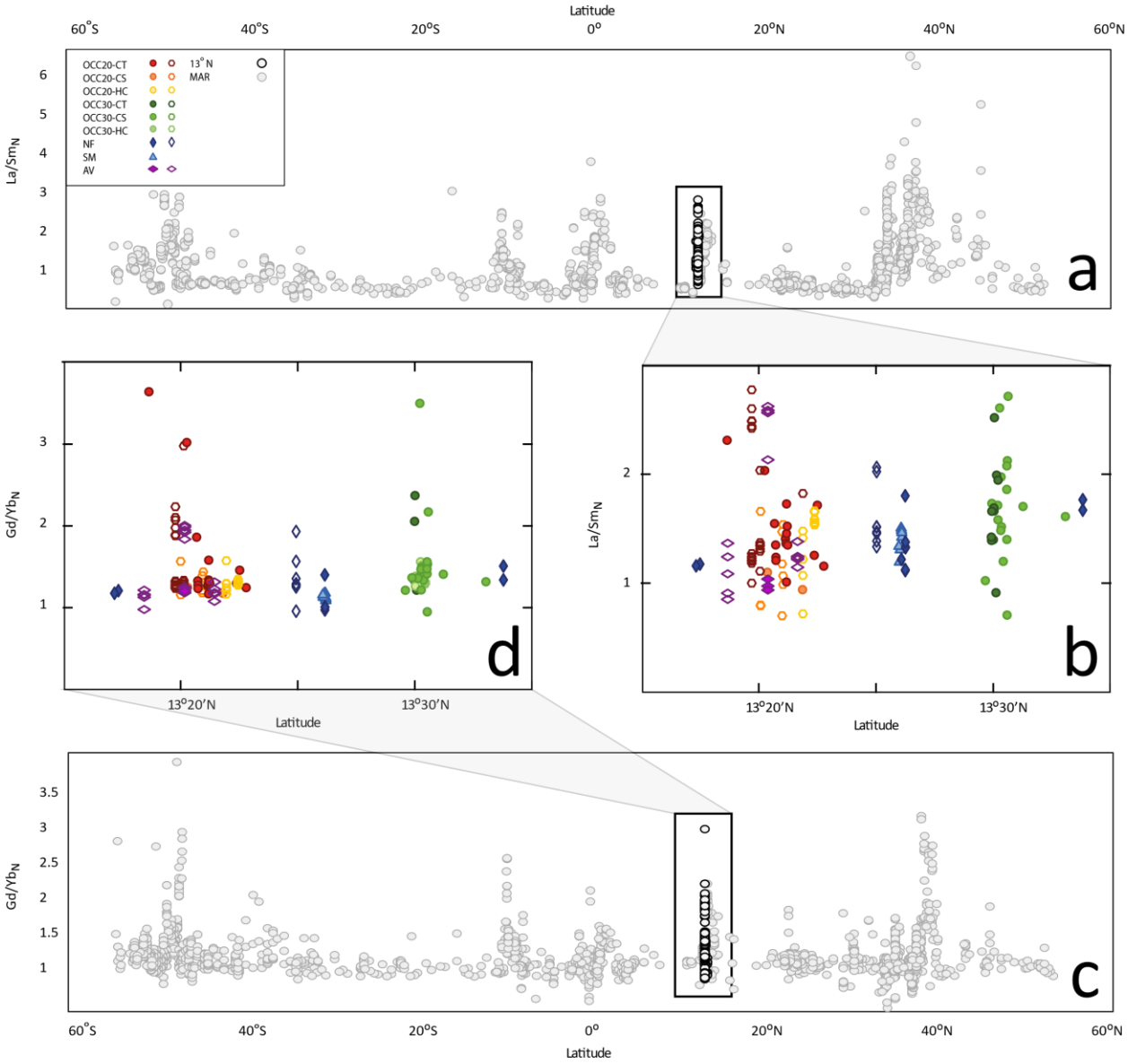

Figure 14: (a) La/Sm$_N$ versus latitude for MAR MORB, outlining the 13°00' – 13°36'N samples. (b) La/Sm$_N$ versus latitude from 13°00' – 13°36'N, with closed symbols representing samples from this study and open symbols representing samples from Wilson, Murton et al. (2013). (c) Gd/Yb$_N$ versus latitude for MAR MORB, outlining the 13°00' – 13°36'N samples. (d) Gd/Ybm$_N$ versus latitude from 13°00' – 13°36'N, with closed symbols representing samples from this study and open symbols representing samples from Wilson, Murton et al. (2013). MAR data represent MORB from the entire spreading ridge, and was obtained from the PetDB on 19.06.17.

Consistent with *e.g.* Gale, Escrig et al. (2011), the MORB suite has been subdivided into *E-MORB* (enriched MORB), representing samples with La/Sm$_N$ >2 , *N-MORB* (Normal MORB), including samples with La/Sm$_N$ <1, and *T-MORB* (transitional MORB) covering the compositional range between E-MORB and N-MORB (figure 15). In REE diagrams, enriched

and depleted MORB may be distinguished from each other by having positive (E-MORB), positive to flat (T-MORB) and negative (N-MORB LREE slopes respectively (figure A1, appendix 5).

The dataset investigated here incorporates all three subgroups of MORB defined above (fig. 14). Unlike the remaining, plume unaffected MAR MORB, most of our samples plot within the T-MORB field (figure 15). An overall positive correlation is seen between La/Sm_N and Gd/Yb_N. Most samples plot along one dominating mixing trend. However, a notable deviation from this trend is seen in some N-, and T-MORB. These samples form a second, less Gd-Yb fractionated, and isolated trend. E-MORB samples appear more scattered than T-MORB and N-MORB samples, and are furthermore isolated from the dominating trend. Some E-MORB samples follow the same curvature as the dominating mixing trend, while others are more MREE-HREE (Gd/Yb_N) fractionated.

OCC20-CT samples are most abundant in the T-MORB field (figure 15). This domain incorporates both highly- and moderately Gd-Yb fractionated samples. OCC20-CS and OCC20-HC samples constitute the intermediate- to lower end of the dominant trend, with most samples plotting in the T-MORB field. A deviation from the dominant mixing trend towards higher Gd/Yb_N values is seen in some transitional- and enriched samples. OCC30-CS is compositionally similar to OCC20-CT, albeit skewed towards higher La/Sm_N values. This domain incorporates the most depleted sample (ODM-ROC-V559-374), which appear to plot on the second (lower Gd/Yb_N) mixing trend. SM lavas represent the more enriched end of this second trend. Relative to OCC lavas, SM lavas display only subtle variance. Except for one sample (ODM-ROC-V559-374), NF lavas plot within the dominant trend, and is restricted to the T-MORB field. AV samples vary from N-MORB to E-MORB. Furthermore, certain AV samples (*e.g.* ODM-ROC-V557- [098-101]) appear to follow the second, less Gd-Yb fractionated trend. The ODM-ROC-V557- [098-101] samples are also notably homogenous.

It is worth noting that the patterns seen in major element plots (figure 11 and 13) are reproduced in the La/Sm_N versus Gd/Yb_N plot (figure 15). That is, E-MORB samples and highly Gd-Yb fractionated T-MORB samples correspond to the alkaline lavas, whereas N-MORB and T-MORB samples constituting the second, less prominent trend corresponds to the highly magnesian samples.

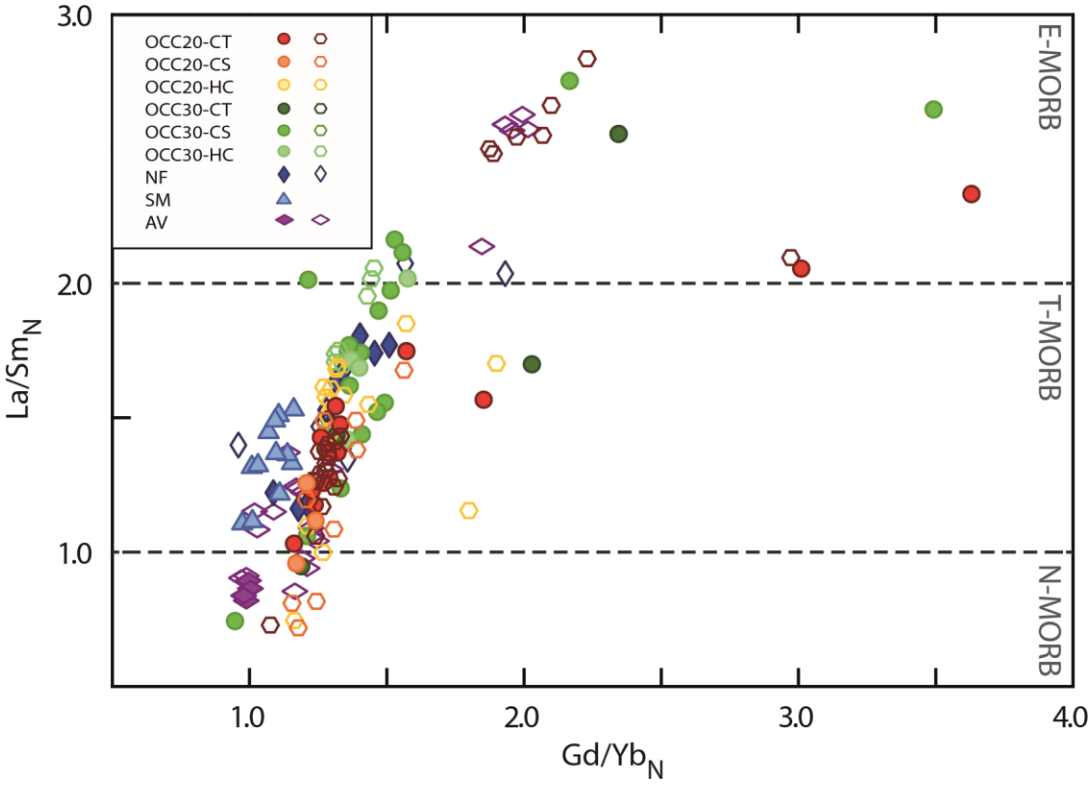

Figure 15: Chondrite normalized (Sun and McDonough 1989) La/Sm$_N$ versus Gd/Yb$_N$ with filled - and open symbols represent data from this study and from Wilson, Murton et al. (2013) respectively. The diagram has been subdivided into three sections: N-MORB, T-MORB and E-MORB, separated from each other by dotted lines. An overall positive correlation is seen between La/Sm$_N$ and Gd/Yb$_N$. In the N-MORB to T-MORB section, SM samples, certain AV samples and one OCC30-CS (ODM-ROC-V559-374) branch off the general trend towards a more Gd/Yb$_N$ poor composition. E-MORB (primarily OCC20-CT, OCC20-CS, OCC30-CT, OCC30-CS, and A lavas display the most extreme Gd/Yb$_N$ ratios. These samples also appear more scattered than the remaining lava suite.

Spider diagrams includes elements that are expected to be significantly influenced by fluid modifications (White 2015b). Hence, these diagrams provide a more comprehensive illustration of the incompatible trace element variance observed in 13°20' – 13°30'N lavas. The most common trace element pattern observed in 13°20' – 13°30'N lavas is relatively similar to that of the average N-MORB (Klein and Langmuir 1989), albeit with higher abundances of most incompatible elements. Hence, the dominating incompatible trace element composition is flat to slightly elevated in spider diagrams (figure 16), consistent with T-MORB. Depletion of highly incompatible elements (Cs, Rb, Ba, Th, Nb, Ta and U) relative to REE, an enrichment of Nb and Ta relative to U, and a depletion of Pb and K relative to Nd are common features in most samples.

The highest incompatible trace element abundances are found within the OCC20-CT, OCC30-CT, and OCC30-CS domains. These enriched samples display prominent depletion in HREE, and correspond to the E-MORB samples addressed in the previous paragraph. Sample ODM-ROC-V546-097, which was described as an outliner based on its major element composition, is seen in the OCC30-CS domain (figure 16) as enriched with Rb, U, K, Pb, Sr, Sm, and Ti depletions. OCC30-CT incorporates the sample with the lowest incompatible trace element abundance (ODM-ROC-V559-374). This sample is characterized by a slightly concave-down pattern and is enriched in Sr relative to Pb and Nd, as well as in Eu relative to Sm and Dy. OCC20-CS and OCC20-HC samples incorporate the most depleted samples in terms of highly incompatible elements. These samples furthermore display prominent negative Rb and K anomalies. Samples with similar Rb and K anomalies are observed in all domains (except the SM domain), but are most abundant in OCC20-CS. OCC30-HC samples are generally more concave-up, and homogenous than the remaining lavas. Furthermore, most of these samples display prominent, positive Pb anomalies. One exception is sample ODM-ROC-V559-374, which was denoted as an outlier in major element plots (figure 11 and 13). SM samples are less heterogeneous than OCC samples, and display a flat to concave-down incompatible trace element pattern. Similar to sample ODM-ROC-V559-374, SM samples display Sr-, and Eu-peaks. Apart from sample ODM-ROC-V545-069 (which is analogues to the SM samples), NF samples display slightly enriched trace element patterns like the OCC samples. AV samples incorporate a range of incompatible trace element patterns. Samples ODM-ROC-V557- [098-101], which are situated immediately in front of OCC20 resemble SM lavas. The most enriched AV lavas correspond to enriched OCC20-CT and appear isolated from the remaining AV lavas.

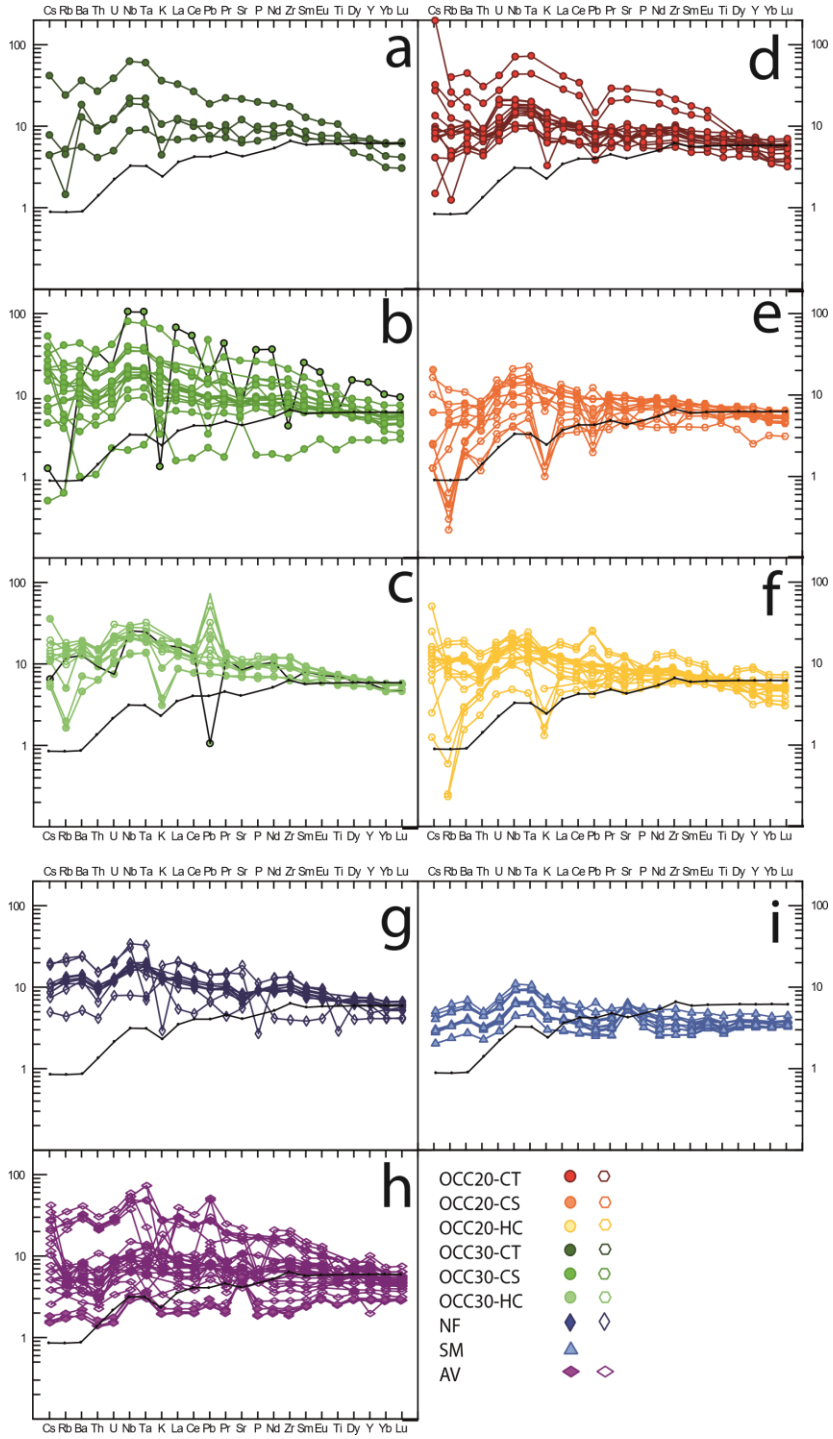

Figure 16: Primitive mantle-normalized (Sun and McDonough 1989) spider diagrams for the 13º20'-13º30'N samples. Black line represents N-MORB from Sun and McDonough (1989). OCC30-CT (a), OCC30-CS (b), OCC30-HC (c), OCC20-CT (d), OCC20-CS (e), OCC20-HC (f), NF (g), AV (f), and SM (i) lavas. Closed symbols represent samples from this study and open symbols represent samples from Wilson, Murton et al. (2013).

5.3 Isotopes

Isotopic ratios are useful source proxies. As the mantle is thought to be heterogenous at different scales a comparison between local (km scale) and ridge scale isotopic ratios becomes essential when interpreting the 13º00'-13º36'N lavas. Similar as with the La/Sm_N and Gd/Yb_N ratios, the range in isotopic ratios (Pb, Sr, Nd, and Hf isotopes) observed in our dataset is of the same magnitude as that reported for the entire MAR (figure 17). The isotopic variation reported here is in good agreement with previous data from this area Wilson, Murton et al. (2013). OCC incorporates the widest range in isotopic ratios (figure 17 b and d).

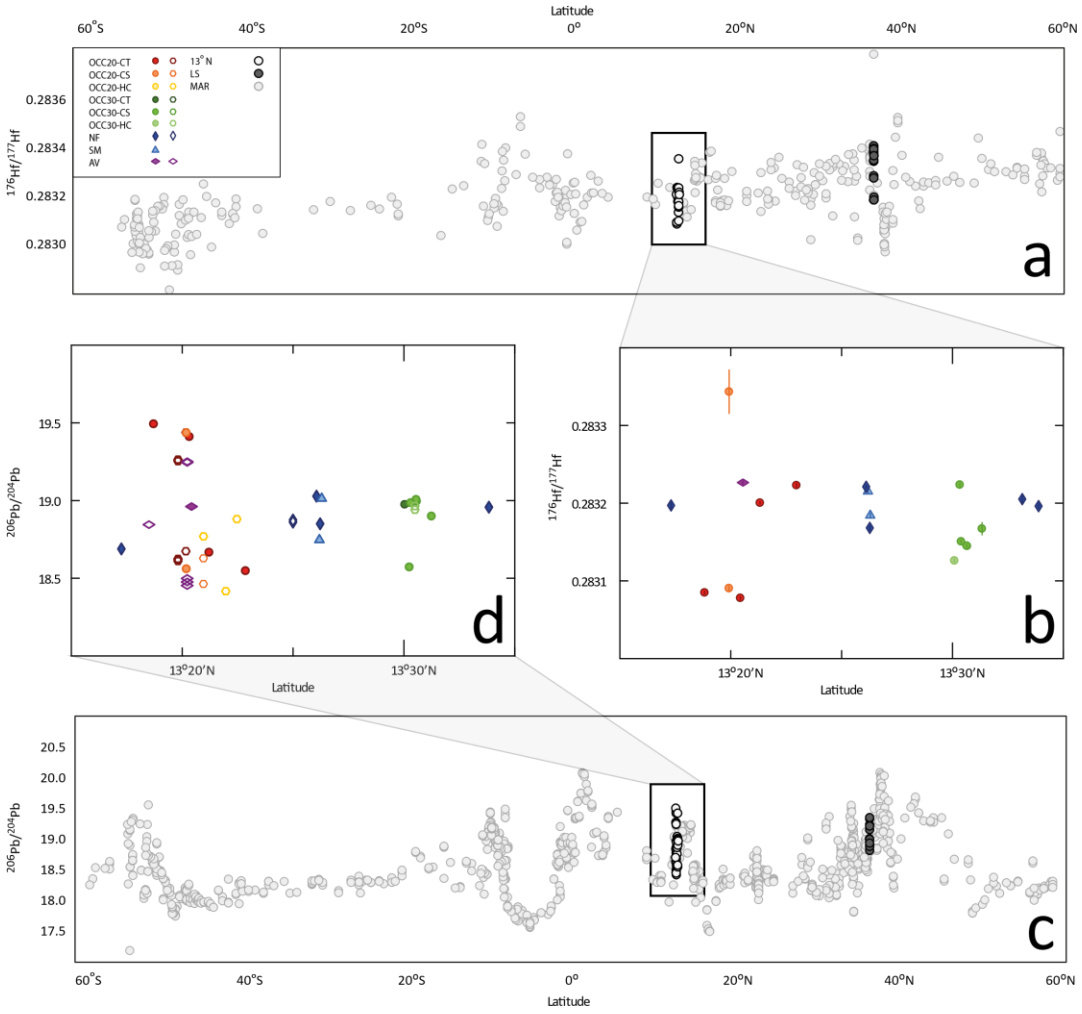

Figure 17: (a) $^{176}Hf/^{177}Hf$ versus latitude for MAR MORB, outlining the 13º00' – 13º36'N samples. (b) $^{176}Hf/^{177}Hf$ versus latitude from 13º00' – 13º36'N, with closed symbols representing samples from this study and open symbols representing samples from Wilson, Murton et al. (2013). (c)$^{206}Pb/^{204}Pb$ versus latitude for MAR MORB, outlining the 13º00' – 13º36'N samples. (d) $^{206}Pb/^{204}Pb$ versus latitude from 13º00' – 13º36'N, with closed symbols representing samples from this study and open symbols representing samples from Wilson, Murton et al. (2013). MAR data represent MORB from the entire spreading ridge, and was obtained from the PetDB on 19.06.17.

In binary isotopic diagrams, 13º00'-13º36'N samples plot along a dominating mixing between a depleted component (low radiogenic Pb and Sr, and high radiogenic Nd and Hf) and an enriched component (high radiogenic Pb and Sr, and low radiogenic Nd and Hf). OCC20-CT, OCC20-CS and AV constitute the most enriched- and the most depleted end of the mixing curve in all isotopic dimensions. Furthermore, these groups are plotting along the entire mixing line. OCC30 samples appear less diverse than OCC20 and AV lavas (figure 17 and 18).

In all isotopic dimensions, samples ODM-ROC-V556-293 and ODM-ROC-V556-307 (OCC20-CT) and ODM-ROC-V550-156 (OCC20-CS), as well as SM, sample ODM-ROC-V545-069 NF, and ODM-ROC-V557-100 (AV) deviate from the dominant trend. These samples appear to extend towards lower $^{87}Sr/^{86}Sr$, higher $^{176}Hf/^{177}Hf$, and higher $^{143}Nd/^{144}Nd$ (figure 18). The deviation is most significant in the $^{87}Sr/^{86}Sr$ dimension.

Relative to the global isotopic ratio systematics, 13º00-13º36'N lavas plot within the enriched part of the MORB field, with markedly elevated $^{206}Pb/^{204}Pb$ values (figure 18 (a, b, d, e, f, g, i)). In the radiogenic Hf-Nd dimension, our data appear to cross-cut the mantle array (figure 18c). That is, the range in $^{176}Hf/^{177}Hf$ is significantly larger than the $^{143}Nd/^{144}Nd$ range in our data compared to the mantle array. A significant discrepancy between the most enriched samples is seen in the $^{143}Nd/^{144}Nd$ - $^{206}Pb/^{204}Pb$ space, where some OCC20-CT samples appear markedly lower in $^{143}Nd/^{144}Nd$ than the remaining dataset for a given $^{206}Pb/^{204}Pb$ value.

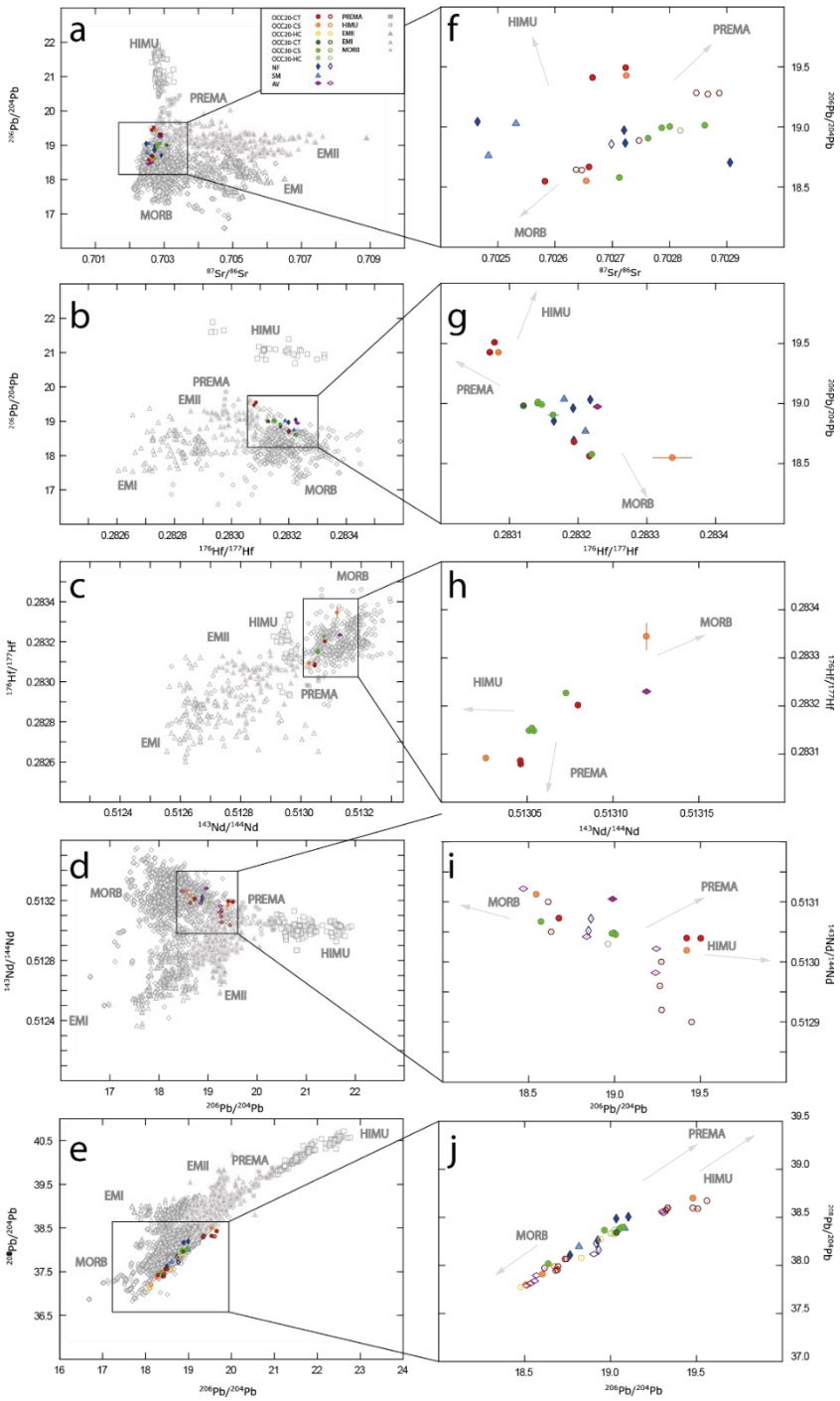

Figure 18: radiogenic isotope-isotope plots, with 13º00'-13º36'N lavas compared to the global isotopic systematics (a-e) and 13º00'-13º36'N lavas alone (f-j). Global isotopic ratio data is from Stracke (2012), and is represented by grey symbols. Data from 13º00'-13º36'N is represented by colored symbols. Closed symbols indicate data from this study, whereas open symbols represent data from Wilson, Murton et al. (2013). (a) and (f); $^{206}Pb/^{204}Pb$ versus $^{87}Sr/^{86}Sr$, (b) and (g); $^{206}Pb/^{204}Pb$ versus $^{176}Hf/^{177}Hf$, (c) and (h); $^{143}Nd/^{144}Nd$ versus $^{176}Hf/^{177}Hf$, (d) and (i); $^{206}Pb/^{204}Pb$ versus $^{143}Nd/^{144}Nd$, (e) and (j); $^{206}Pb/^{204}Pb$ versus $^{208}Pb/^{204}Pb$.

6. Discussion

In this chapter, a conventional petrogenetic model will be presented. The influence of melting- and post-melting effects on the 13º00' – 13º36'N lavas will be explored. Then, the geochemical heterogeneity in the source will be considered. Lastly, a comprehensive, geochemical- and geological model for these lavas will be discussed.

6.1 Petrogenetic model

6.1.1 Fractional crystallization

On their way up to the surface, primary melts are undergoing a complex magmatic history, modifying their chemical composition. Differentiation by fractional crystallization, melt mixing and assimilation is expected to modify primary melts to various degrees. The continuous tholeiitic fractionation trend observed for most samples in the TAS diagram (figure 11) suggests progressive crystal fractionation. At 50-100 MPa, olivine is saturated in melts, followed by plagioclase and clinopyroxene respectively (Klein 2003). It became clear from figure 13 that N-MORB and T-MORB samples follow a trend from high MgO and low TiO_2, SiO_2, FeO_T, Al_2O_3, K_2O and Na_2O towards correspondingly low MgO and high TiO_2, SiO_2, FeO_T, Al_2O_3, K_2O and Na_2O values (figure 13). This chemical variation agrees with the progressive removal of Mg with low-pressure olivine fractionation and subsequent accumulation of the remaining oxides. The proportion of samples along this trend reflects the degree of fractional crystallization from the parental melt.

A slightly different trend is seen in the MgO versus Al_2O_3 and CaO (figure 13), featuring a "kink" in the fractionation trend at MgO ≈ 9 wt.%. As Al_2O_3 and CaO are major constituents of plagioclase, this kink is interpreted to reflect the onset of plagioclase saturation (figure 13). Melts with MgO > 9 wt.% may thus be interpreted as primary, with crystal fractionation limited to olivine. The nature of these high-Mg melts will be discussed later in this chapter. In addition to this LLD, composed primarily of N- and T-MORB samples, a second trend incorporating E-MORB samples is seen variation diagrams (figure 13). These lavas are characterized by elevated

TiO_2, FeO_T, Na_2O and K_2O for a similar MgO range as the major trend (figure 13). Existence of different trends in variation diagrams refute the theory of a straightforward evolution of 13º00'-13º36'N lavas. Similar observations were drawn for other MAR segments (*e.g.* Menez Gwen, Lucky Strike) (Gale, Escrig et al. 2011). Along those segments such separation of major elements into more- and less alkaline groups have been attributed to multiple parental magmas (Gale, Escrig et al. 2011). Ultimately, it appears from the above discussion that the major element diversity reflects both different natures and evolutions of parental melts.

6.1.2 Primary MORB melts?

One of the most striking results of the studied area is the presence of unusual high MgO basalts (see fig 12). A compilation of nearly 7000 MORBs from PetDB (www.petdb.com) gives an average MgO value of 7.46 ± 0.97 (1σ, n=6937). High MgO samples from 13º00'-13º36'N have a concentration statistically higher than 99.9% of the MORB global population. The elevated Mg-contents are consistent with limited crystal fractionation from parental melts. Indeed, it raises the question of whether these basalts were in equilibrium with their corresponding mantle source. A useful proxy for melt evolution is the Mg#. The highest Mg#s are found associated with samples collected on the seamount between the two detachment faults, as well as in some axial valley (AV) samples (ODM-ROC-V547-[098-101]), and one OCC30-CS sample (ODM-ROC-V559-374). A positive, two-folded correlation between Ni and Mg# is seen for the bulk lava suite.

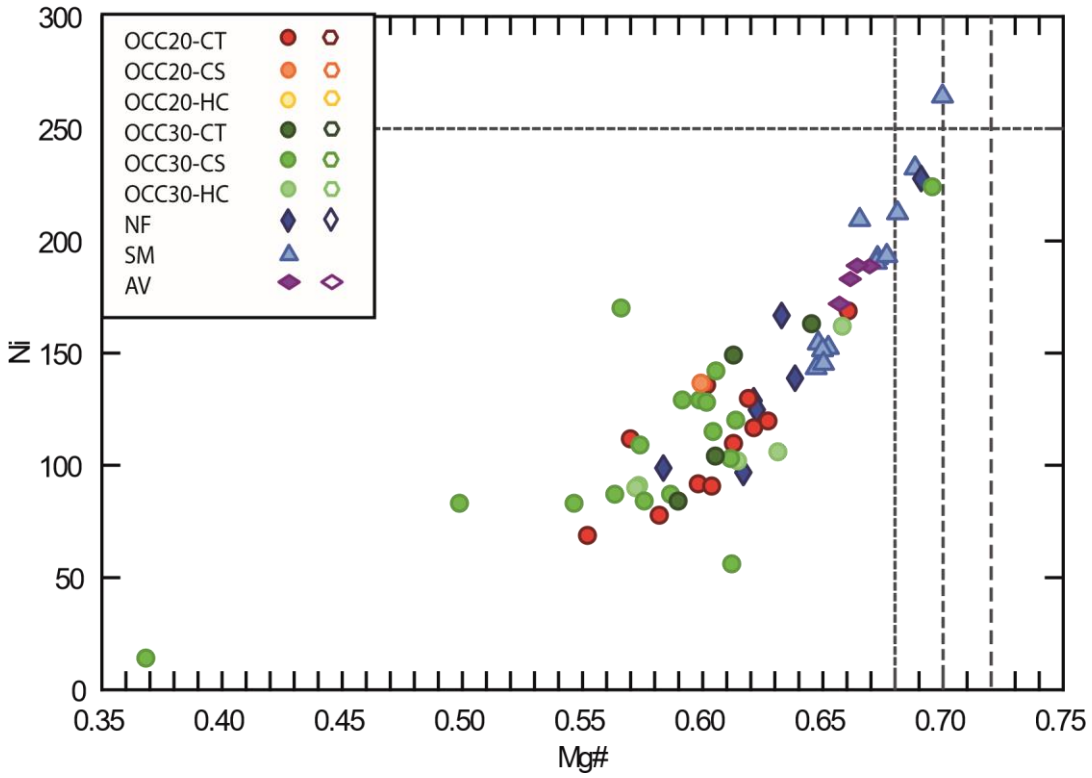

Figure 19: Ni versus Mg# for samples from this study, displaying two distinctive correlation curves. Vertical, dotted lines indicate Mg# concentrations expected for melts in equilibrium with a typical mantle peridotite at 0.5 GPa, 1.0 GPa, and 1.5 GPa from left to right, and horizontal line indicating Ni abundance (ppm) at 0.5 GPa. In terms of Mg#, certain NF samples, as well as one SM sample and one OCC20-CF sample plot within the field of primary melt composition. Only one sample (ODM-ROC-V545-073), displays Ni contents sufficient to represent primary melts (Ni = 263 ppm).

Several aspects should be considered when determining if melts were equilibrated with their sources. Given that olivine is the first phase to crystallize from primary melts, a reduction in olivine-compatible element concentrations (*i.e.* Ni, MgO) is expected to occur as a function of crystal fractionation. Since the composition and the partitioning coefficients of Fe and Mg in mantle peridotite at different depth are known, the Mg# of primary melts can be calculated using simple equations (see appendix 4). Assuming a typical mantle peridotite with olivine composition > Fo_{88}, K_d values for Mg between 0.3 to 0.35, and pressure of melting between 0.5 GPa to 1.5 GPa, primary melts Mg# are expected to range from 0.68 to 0.72 (Sen (2014), p. 111), with Ni > 250 ppm ((Gill 2010), p 319). According to the criterions given above, several lavas from 13º00'-13º36'N may be considered near-primary or even primary (see figure 19)

However, as it will be discussed in a later chapter, the 13º00'-13º36'N mantle source is not simply composed of peridotites, and is believed to contain various amount of eclogite or

pyroxenite. The high Mg contents in melts derived from this source may thus be influenced by these lithologies. Wilson, Murton et al. (2013) argued that the most primary melts observed in the 13°00'-13°36'N area were also among the most enriched samples. According to these authors, such elevated Mg concentrations may result from early saturation of Mg-rich clinopyroxene in melts derived from a recycled component (Wilson, Murton et al. 2013). Based on this assumption, Wilson, Murton et al. (2013) suggested that these lavas reflected melting of a high-Mg source rather than a primitive DMM melts. Our extended dataset reveals that high magnesium concentrations are not restricted to the most enriched samples. Transitional MORBs collected during the ODEMAR cruise are also showing this high MgO characteristic (figure 12, 13, 14, 22, 23, and 24), invalidating Wilson et al., (2013) conclusions. The origin of these melts is probably more complex than previously assumed and will be discussed further in section 6.3.

6.1.3 Eu and Sr positive anomalies in high MgO basalts

Another unusual characteristic of 13°00' – 13°36'N, high MgO lavas is the existence of positive-Sr- and Eu- anomalies (figure 20). These anomalies may be constrained by comparing the chondrite normalized Eu and Sr concentrations to their interpolated values, Eu* and Sr* (Eu/Eu*and Sr/Sr*) (Weill and Drake 1973). Eu/Eu* > 1 and Sr/Sr* > 1 represent positive anomalies in spider diagrams, whereas negative anomalies yield Eu/Eu* < 1 and Sr/Sr* < 1.

While most samples in this dataset are slightly negative or ≈ 1 in Eu/Eu* and Sr/Sr*, SM samples and associated NF samples along with some AV samples (ODM-ROC-V547- [098-101]) show noticeable positive Eu- and Sr- anomalies (figure17). The most extreme positive anomalies are featured in the AV lavas and in one OCC30-CS sample (ODM-ROC-V559-379). It becomes clear from figure 19 d that these samples also display the highest MgO concentrations. Negative anomalies are restricted to the most evolved lavas, whereas positive anomalies dominate in primitive melts.

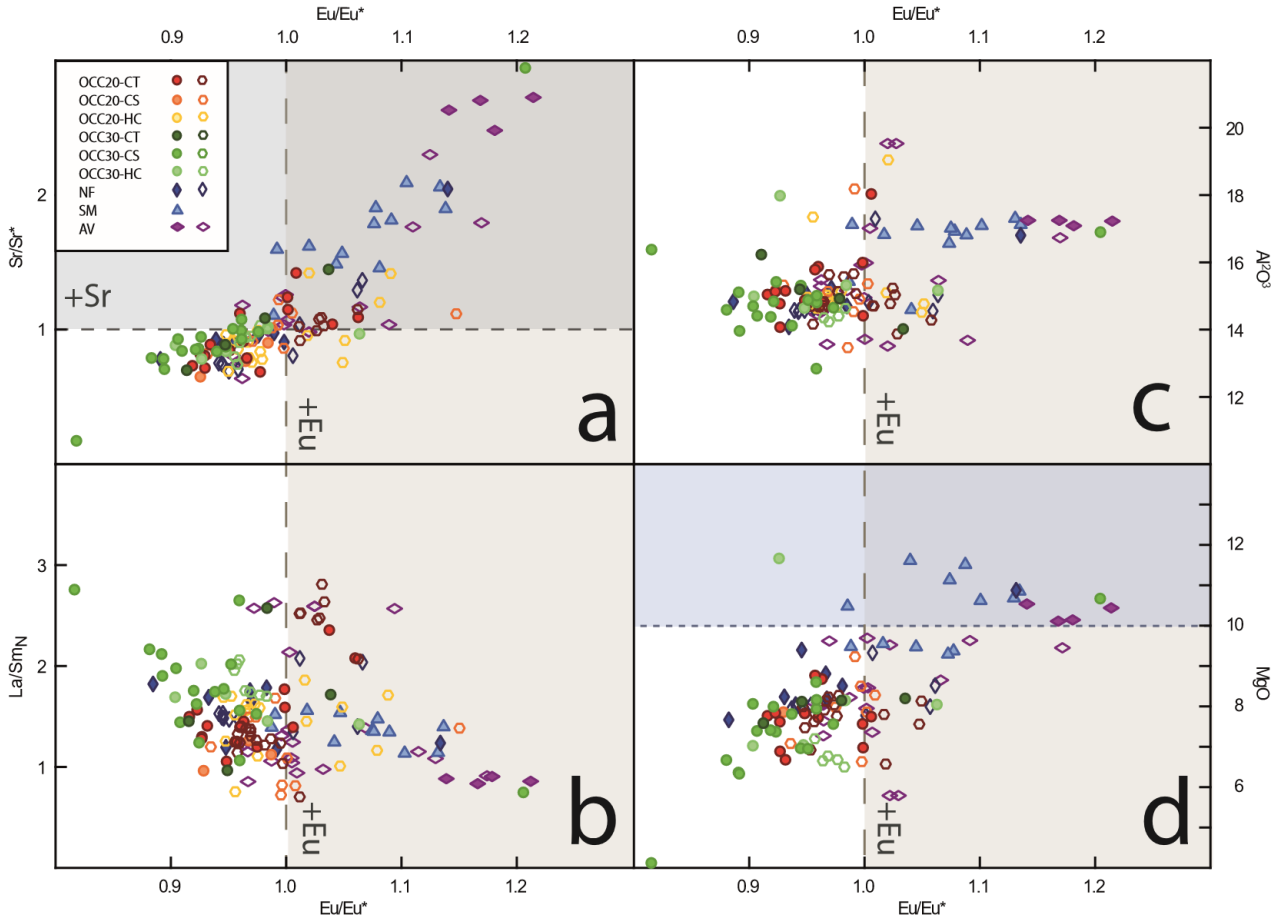

Figure 20: (a) Eu/Eu = Eu_N / sqrt (Sm_N x Gd_N) versus Sr/Sr* = Sr_N / sqrt (Pr_N x Nd_N) displaying a moderately to good correlation for the bulk dataset. Most samples plot in the negative Sr- and Eu- field (Eu/Eu* < 1 and Sr/Sr* < 1), but SM samples, certain OCC20-HC samples (ODM-ROC-V547-(099-101)) and one OCC30-CS) display various extents of positive anomalies (Eu/Eu* > 1 Sr/Sr* > 1). The dotted lines represent the transition from negative Eu- and Sr-anomalies and positive anomalies. (b) La/Sm_N versus Eu/Eu*. Three distinctive trends are observed with varying Eu/Eu* for the same La/Sm_N range. (c) Al_2O_3 versus Eu/Eu* no apparent trend, but a distinctive separation between SM samples, certain OCC20-HC samples (ODM-ROC-V547-(099-101)) and one OCC30-CS and the remaining dataset. OCC20-CT and certain AV lavas also appear high in Al2O3 for a given Eu/Eu*. (d) MgO versus Eu/Eu* displaying a slight, positive correlation, with the highest Eu-anomalies dominating in the primitive field (blue).*

To constrain the nature of the positive and negative Sr- and Eu- anomalies, it becomes necessary to consider the influence of plagioclase on these melts. We have seen in section 4.1.1 that a change in the fractionation trend is observed in the 13º00'-13º36'N (figure 13). This change represents the onset of plagioclase saturation in the LLD. Under reducing conditions, Eu^{3+} becomes divalent (Schreiber 1986) and therefore may readily substitute for Ca^{2+} in plagioclase (Weill and Drake 1973). Fractionation of Eu from their neighboring REE (Sm and Gd) is thus expected to be proportional to plagioclase precipitation. In a similar manner, Sr^{2+} is compatible in plagioclase mineral lattice. The apparition of Sr- and Eu- negative anomalies with lower MgO

concentrations is coherent with fractional crystallization of plagioclase. If this observation is not a surprise in MORB, it is much more challenging to explain the positive anomalies observed in the 13°00'-13°36'N high MgO samples. Three possible scenarios can be considered:

- First, analytical techniques should be assessed. The presence of plagioclase phenocrysts in analyzed samples is expected to significantly bias the Eu/Eu* and Sr/Sr* signal. However, in the dataset investigated here, only very rare plagioclase micro-phenocrysts were observed. For example, the sample exhibiting the most noticeable Sr- and Eu-anomalies (ODM-ROC-V545-083) is completely aphyric. This first hypothesis seems therefore unlikely.
- A second hypothesis is to consider the assimilation of plagioclase cumulates from the lower oceanic crust by melts (Tang, McDonough et al. 2017). Indeed, a plagioclase under-saturated, MgO rich melt is expected to dissolve any plagioclase added to it during its path from source to surface (Tang, McDonough et al. 2017). In accordance with this theory, an increase in Eu/Eu* should be accompanied by increasing values of Al_2O_3. However, no apparent correlation is seen between Al_2O_3 and Eu/Eu* in this study (figure 20 c), suggesting a more complex nature of these positive anomalies.
- A third alternative hypothesis is that the positive Sr- and Eu- anomalies reflect the ancient influence of a plagioclase bearing, recycled component. If this theory holds, more enriched signals are expected to follow positive Eu- and Sr- anomalies. In Figure 20 b we observed a generally more elevated La/Sm_N for samples with Eu/Eu* > 1. This observation supports the theory that these positive anomalies are related to an enriched eclogite source. However, it is worth noting that the highest positive Eu-anomalies are seen in the most Mg-rich samples. This is not expected if these anomalies are attributed to an eclogite (*i.e.* less magnesian) source. According to Sobolev, Hofmann et al. (2000), eclogite signatures may be evident in trace element systematics (*e.g.* elevated Eu/Eu*) without the corresponding major element evidence (Sobolev, Hofmann et al. 2000). Regardless of how refractory the source is, it may ultimately display a certain "ghost plagioclase" signature, resulting from interaction between reactive melts and ambient mantle. If so, the less enriched lavas may still bear the mark of eclogite signatures.

Based on the above discussion, I propose that the positive Sr- and Eu- signatures are best explained by a pyroxenite source. That is, a refractory peridotite source which has been re-fertilized by eclogite melts. This theory will be further constrained in the following discussion.

6.1.4 Melting and melt extraction

As suggested by earlier studies (Wilson, Murton et al. 2013), the effect of fractional crystallization and assimilation fail to reproduce the large variation observed in the 13º00'-13º36'N lava suite. These lavas are associated with detachment faults, whose initiation, evolution and termination are believed to be consistent with a varying melt supply (MacLeod, Searle et al. 2009). It is therefore crucial to constrain the geochemical variance related to melting.

Elements fractionate from each other as a function of incompatibility and melting extent. Hence, large variations in the most incompatible trace elements, accompanied by relatively constant moderately incompatible- and compatible elements patterns could suggest varying degree of melt related fractionation. Recall from section 5.1.1. that E-MORBs (*i.e.* specific OCC20-CT and CS, OCC30-CT, and CS, and AV lavas) display elevated K_2O, TiO_2, and Na_2O for a similar MgO range as N- and T-MORB (figure 13). This suggests a more enriched parental melt for E-MORB. E-MORBs also display enriched trace element patterns (figure 15 and 16), suggesting significant fractionation during melting of these lavas. Assuming this fractionation is exclusively attributed to recent mantle melting beneath the ridge axis, the most fractionated samples reflect also the lowest melting extents.

As the mantle beneath the 13º00'-13º36'N region of the MAR is interpreted to be compositionally heterogeneous (Wilson, Murton et al. 2013), this assumption is at best an oversimplification. A more likely scenario is that the trace element signal is influenced both by melting and source heterogeneity. To test this hypothesis, it is useful to compare source sensitive and melting sensitive parameters.

The ratio between LREE and HREE (*e.g.* La/Sm_N) is influenced by both source signature and melting extent. To constrain the influence of melting extent on REE patterns, an estimate of REE concentrations at different melting extents (from F=2% to F=20%) is provided in figure 21. From

this model, it appears clearly that the range in REE abundances in our data significantly exceed the variations estimated by melting a homogenous source at various melts fractions. This implies that the enriched REE patterns observed in 13º00'-13º36'N is significantly influenced by source heterogeneity.

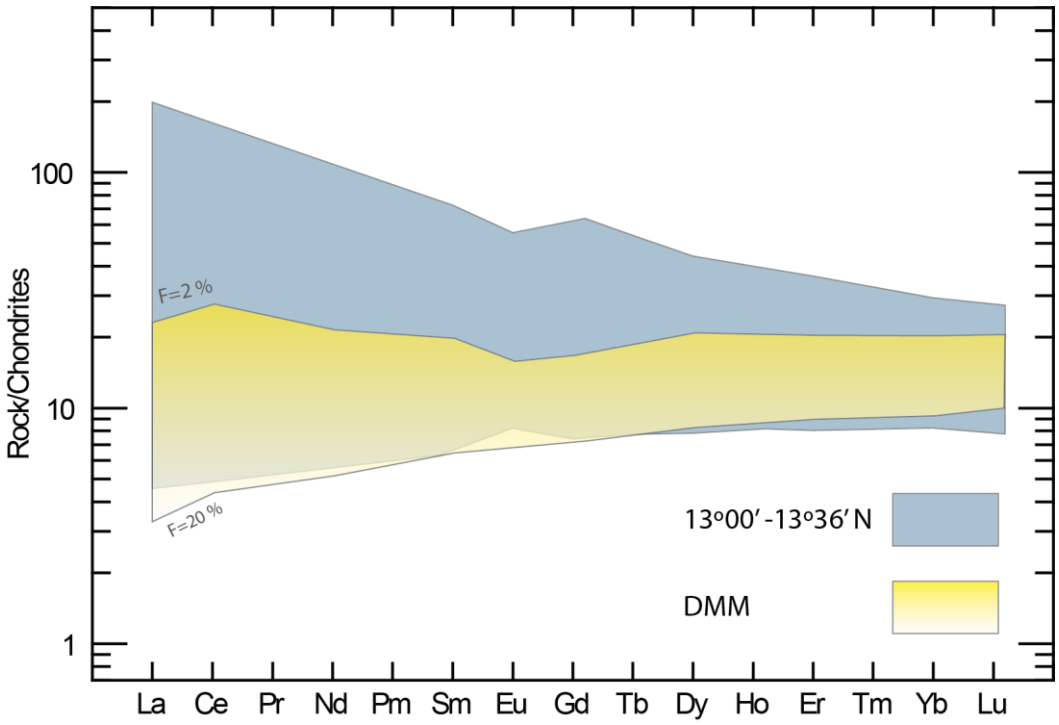

Figure 19: REE diagram normalized to chondrite (Sun and McDonough 1989). The range in REE abundances in 13º00' – 13º36N lavas is indicated by the blue area. The yellow, graded area represent the calculated range between melts produced by 20 % (light yellow), and at 2% (bright yellow) melting. DMM composition correspond to the average DMM estimated by Salters and Stracke (2004). Melt compositions were calculated using the non-modal equilibrium melting (equation 1.3, Appendix 4), using partition coefficients and melting modes from Salters and Stracke (2004).

Supporting this assumption is the relationship between trace element- and isotopic ratios. As isotopic ratios are not varying with recent melting degrees, they are useful proxies for estimating source heterogeneities. Comparison between melting sensitive trace element ratios (Ba/Hf, La/Sm, and Sm/Yb) and source controlled isotopic ratios ($^{206}Pb/^{204}Pb$ and $^{176}Hf/^{177}Hf$) is provided in figure 22. These plots reveal a strong correlation between trace elements- and isotopic ratios in 13º00'-13º36'N lavas. It should be noted that certain samples are plotting away from the overall trend (see figure 19, caption), suggesting a more complex nature of these lavas (further elaborated in section 6.2). The correlation between trace element ratios and isotopic

ratios indicates a progressive increase in element fractionation and hence decrease in melting extent with increased isotopic enrichment.

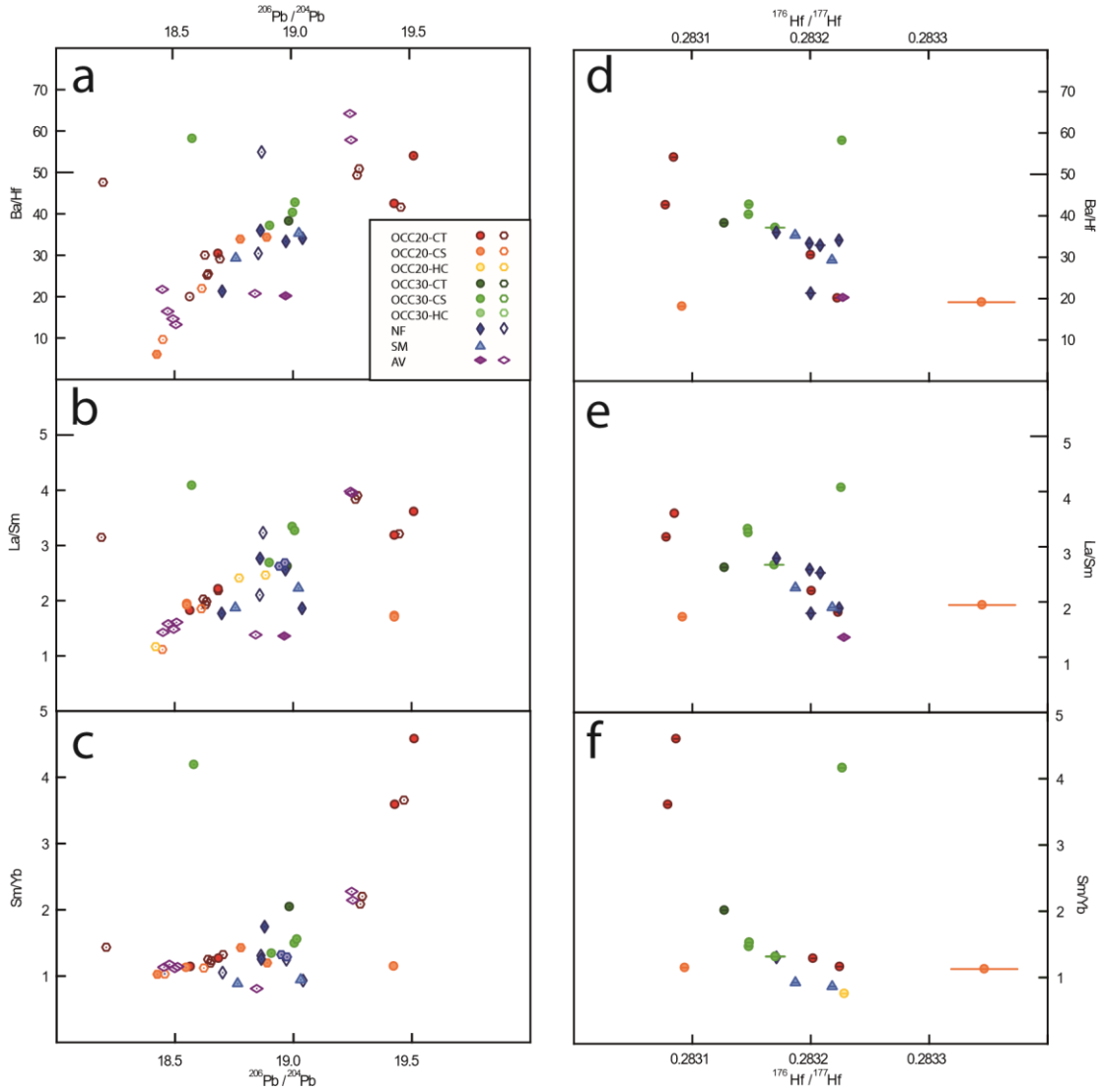

Figure 20: melting sensitive trace element ratios versus isotopic ratios. Positive correlation between $^{206}Pb/^{204}Pb$ and Ba/Hf (a) and La/Sm (b) and Sm/Yb (c), except for sample ODM-ROC-V550-160 (OCC20-CS), ODM-ROC-V546-097 (OCC30-CS) and SM samples and associated NF samples along with certain OCC20-HC samples (ODM-ROC-V547- [098-101]). Similarly, negative correlation between $^{176}Hf/^{177}Hf$ and Ba/Hf (d) and La/Sm (e), and Sm/Yb (f), with exception of OCC20-CS samples ODM-ROC-V550-160 ($^{17}6Hf/^{177}Hf > 0.2833$) and ODM-ROC-V550-156 ($^{176}Hf/^{177}Hf < 0.2831$), sample 546-097 and sample ODM-ROC-V542-038 (OCC30-CT). Note that sample ODM-ROC-V550-160 has a high error bar in the Hf-isotope space.

It becomes clear from the above discussion that source variance has a strong influence on the observed trace element variation. Constraining the effect of melting on trace element systematics is thus cumbersome. Moreover, it is unlikely that all melts where generated at similar pressures within the melting column (Stracke and Bourdon 2009). A more likely scenario is one where

melts were derived from a range of different depths at different melting extents, and further partially mixed during their path to the surface. Such a scenario is referred to in the literature as a polybaric melting (Stracke and Bourdon 2009). A general assumption is that the extent of melt mixing varies as a function of melting depth (Rubin, Sinton et al. 2009).

To constrain the melting depth, it can be useful to consider the mantle lithology within the melting column. The presence of garnet in melt sources provides a viable constraint on the melting depth, as this aluminous phase is stable in peridotite only at depths > 85 km (Robinson and Wood 1998). Owing to the strong affinity of HREE in garnet compared to other rock forming mineral phases, the presence of garnet in the source ultimately causes HREE to be detained in the residue (Hellebrand, Snow et al. 2002). Depending on the melting extent and the abundance of garnet, HREE consequently fractionate from the remaining REE, inducing elevated MREE/HREE (*e.g.* Gd/Yb_N). In the samples investigated here, such "garner effect" appears restricted to groups OCC20-CT, OCC20-CS, OCC30-CT, OCC30-CS, and AV lavas (figure 15 and 16 a, b, d, e, and h). It is reasonable to assume that these melts were generated in the garnet stability field, *i.e.* at greater depths than the other groups.

A complicating aspect of this theory is the expected presence of garnet in the enriched (eclogite) domain, producing the same "garnet signature" (Hirschmann and Stolper 1996, Pertermann, Hirschmann et al. 2004, Wilson, Murton et al. 2013). To distinguish between these two scenarios, it is useful to compare HREE fractionation with source enrichment (*e.g.* La/Sm_N). A positive correlation between Gd/Yb_N and La/Sm_N for the bulk dataset, as well as low Al_2O_3 contents of the most Gd-Yb fractionated samples (figure 13) support the theory of lithology-controlled garnet effect (figure 15). The observation that some transitional and enriched samples display more prominent Gd-Yb fractionation for a given La/Sm_N (figure 15) suggests a more complex nature of these melts. This may be the result of (1) lower melting extents in the presence of garnet, or (2) different source lithology (*i.e.* higher concentrations of garnet in the source). The nature of the highly Gd-Yb fractionated samples will be further elaborated in the next section.

6.2 Mantle structure and heterogeneity

6.2.1 Mantle signal

In the above discussion, the chemical effect of melting extent and depth range of melting on the trace element signal was investigated. It is clear that significant geochemical variance can be traced all the way from the mantle source.

The most solid proxy for mantle heterogeneity is the isotopic signal, as ratios between heavy isotopes do not fractionate during partial melting or fractional crystallization (Stracke 2012). Figure 18 reveals trends in isotopic systems, which suggest the existence of at least two isotopically distinct components in the mantle source. Compared to the remaining MAR MORB dataset, the 13º00'-13º36'N lavas appear as an enriched sharp spike (high $^{206}Pb/^{204}Pb$, $^{87}Sr/^{86}Sr$ and low $^{143}Nd/^{144}Nd$ and $^{176}Hf/^{177}Hf$) in an generally depleted region (figure 17c). This spike is attributed to the most enriched OCC20-CT, OCC20-CS, OCC30-CT, OCC30-CS, and AV samples. Based on simple geochemical modelling, Wilson, Murton et al. (2013) concluded that the depleted end of the lava suite, was a ultra-depleted MORB (UDMM) mantle consistent with Workman and Hart (2005), with some HIMU influence. In their model, the enriched end-member was argued to be consistent with a HIMU source ($^{206}Pb/^{204}Pb$ > 19.6 and $^{87}Sr/^{86}Sr$ <0.7030, $^{143}Nd/^{144}Nd$ <0.5129). According to these authors, 13º00'-13º36'N lavas resemble the enriched lavas that prevail in equatorial MAR lavas (Hannigan, Basu et al. 2001). Furthermore, Wilson, Murton et al. (2013) argued that a second enriched, PREMA-like source component was necessary to account for the scattered appearance of the most enriched samples (see section 6.1.4). In this sub-section, the nature of the 13º00'-13º36'N lavas will be re-evaluated considering our new dataset.

As addressed in section 6.1.4, some transitional and enriched samples deviate significantly from the main mixing trend towards high Gd/Yb_N ratios. A reasonable approach to resolving the nature of these again to compare source sensitive- and melting sensitive parameters. It became clear from figure 18 that at least the E-MORB samples (OCC20-CT and OCC20-CS) deviated from the main trend also in isotope binary diagram. These samples are thus more likely to reflect heterogeneities internally in the enriched domain. This presumption agrees with the suggested

presence of two distinctive, enriched components (HIMU and PREMA) in the 13º00'-13º36'N source region (Wilson, Murton et al. 2013).

Our new data reveals a second, deviating trend of the moderately enriched Seamount (SM) samples and associated normal fault (NF) sample, as well as certain axial valley (AV) samples (ODM-ROC-V547-[098-101]) (figure 15), pointing to a fourth mantle component. This observation has not been accounted for by Wilson, Murton et al. (2013). Ultimately, it is suggested here that the 13º00'-13º36'N mantle source consist of a bimodal depleted source as well as a bimodal enriched source. These assumptions highlight the complexity of the source heterogeneity.

It became clear from section 6.1.1 that the observed major element variance is, in part, attributed to the parental melt. Elevated TiO_2, FeO_T, and Na_2O, along with slightly lower values of SiO_2 in E-MORBs (figure 13) are present in samples showing trace element coherent with a garnet signature (figure 15) and enriched isotopic signature (figure 18). Similar compositions have been interpreted to reflect a garnet bearing, silica-deficient eclogite or pyroxenite source (Stracke and Bourdon 2009). Supporting this theory is the branching of enriched melts into a second mixing trend in the Ni-MgO plot (figure 2). Relative to the major Ni-MgO trend, this second trend displays elevated Ni concentrations for a similar Mg# range. Previous studies have attributed similar high-Ni systematics the influence of eclogite melts (Sobolev, Hofmann et al. 2005, Wang and Gaetani 2008). According to this theory, equilibration of eclogite melts with peridotite olivine increases the concentration of Ni in these melts.

6.2.2 ReLish component

A good correlation between $^{176}Hf/^{177}Hf$ and $^{143}Nd/^{144}Nd$ is expected since their corresponding parent-daughter (^{173}Lu-^{176}Hf and ^{147}Sm-^{143}Nd) behave in a similar manner during partial melting (Salters, Mallick et al. 2011). The correlation found in our dataset is in good agreement with this general statement. However, this correlation is exhibiting an unusual steep slope relative to the mantle array (figure 18 (c)). This imply a high $^{176}Hf/^{177}Hf$ value for a given $^{143}Nd/^{144}Nd$. To account for these anomalous ratios, significant decoupling of the Hf isotopes from the Nd isotopic system is required. This scenario requires the presence of garnet in the melting source

(Hamelin, Bezos et al. 2013) (Salters, Mallick et al. 2011). The partition coefficient in HREE significantly increases in the presence of garnet, making these elements compatible in its crystal lattice. Since Lu is a HREE and Sm is not, Lu will be retained in the melting residue compared to Sm when the source contains garnet. Consequently, $^{173}Lu/^{176}Hf$ (and time integrated $^{176}Hf/^{177}Hf$) will be larger than $^{147}Sm/^{143}Nd$ (and $^{143}Nd/^{144}Nd$) in the mantle residue. The magnitude of decoupling between Lu-Hf from Sm-Nd systems is proportional to the abundance of garnet in the source and the melt fraction (Salters, Mallick et al. 2011).

Among theories proposed as an explanation for anomalous $^{176}Hf/^{177}Hf$ composition is disequilibrium melting (Blichert-Toft, Agranier et al. 2005). This theory states that grain-scale variation in Hf exist in garnet-bearing sources, as garnet retains Lu more efficiently than Hf during melting. Melts derived from a source which is locally enriched in garnet may thus display extreme $^{176}Hf/^{177}Hf$ compositions (Blichert-Toft, Agranier et al. 2005). Hamelin, Bezos et al. (2013) argued that this explanation could not hold for the anomalous Hf variability observed in Lucky Strike basalts. Evidence against this theory was (1) lack of deviations of Hf from other isotopic systematics, (2) the absence of garnet signature in anomalous basalts displaying anomalous garnet signature, and (3) the short time-scale of grain-scale equilibration compared to the time scale for a build-up of radiogenic Hf anomalies. These authors attributed the anomalous Hf-signal to a real mantle component rather than melting induced fractionation.

The 13º00'-13º36'N data display similar $^{176}Hf/^{177}Hf$ systematics as the Lucky Strike basalts (figure 23). In similar manner as Lucky Strike samples, our dataset display negligible deviation from the MAR trend in other isotopic systems (*e.g.* $^{87}Sr/^{86}Sr$, $^{206}Pb/^{204}Pb$, $^{207}Pb/^{204}Pb$, $^{208}Pb/^{204}Pb$, and $^{144}Nd/^{143}Nd$). Differing to what is expected from Blichert-Toft, Agranier et al. (2005), samples displaying radiogenic Hf values in this dataset are devoid of any garnet signature (figure 15 and 16). Furthermore, samples showing HREE depletion (see section 4.1.3) display the lowest radiogenic Hf-values. This is compelling evidences that the anomalously high radiogenic Hf composition observed reflects a unified source rather than grain scale variance.

The origin of such high $^{176}Hf/^{177}Hf$, depleted source remains enigmatic. Given that the decoupling of $^{176}Hf/^{177}Hf$ from other isotopic systems requires the presence of garnet, it is likely that this mantle component represent a residual mantle from melting in the garnet stability field (Salters, Mallick et al. 2011, Hamelin, Bezos et al. 2013, Frey, Nobre Silva et al. 2015). The

magnitude of decoupling is proportional to the garnet concentration and the time elapsed since the melting event, that is, the time duration of isolation of this mantle domain from melting events. Salters, Mallick et al. (2011) argued that such a high-$^{176}Hf/^{177}Hf$ component represented ancient residues from MORB melting, and named it ReLish (Residual Lithosphere). Frey, Nobre Silva et al. (2015) argued for ancient, a low melting extent in the garnet stability generate the ReLish component, and high melting extents of this component to produce the more recent ReLish melts. The anomalous Hf composition of Lucky Strike basalts (figure 23) has been attributed to (1) mixing between the ReLish component (20 %), a local MORB component (70%), (2) reaction of this solid-state mixture with enriched, low-F Azores plume melts (10%), and (3) melting of the resulting component beneath the ridge axis (Hamelin, Bezos et al. 2013).

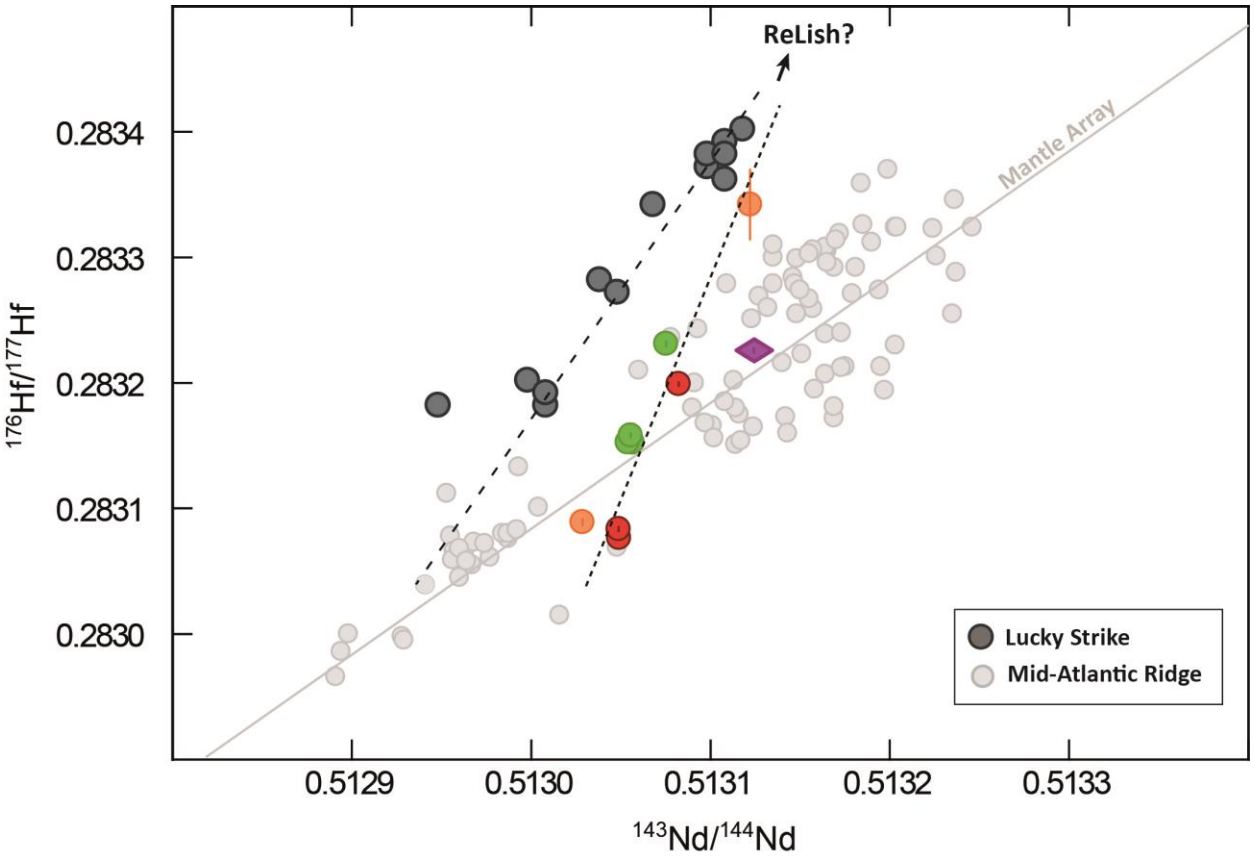

Figure 21: MORB data from the MAR (60ºS – 60ºN) obtained from PetDB on the 19.06.17 along with LS data and data from this study. $^{176}Hf^{177}$ Hf versus $^{143}Nd/^{144}Nd$, with anomalously high $^{176}Hf^{177}$ Hf for a given $^{143}Nd/^{144}Nd$ composition in all LS samples. Data from this study are crosscutting relative to the mantle array, approaching the anomalously depleted LS trend, likely to be similar to the ReLish component (Hamelin, Bezos et al., (2013)).

6.2.3 Geochemical modelling

To reproduce the geochemical and isotopic variance observed in the 13º00'-13º36'N area, and to further constrain the nature and significance of the ReLish component to these melts, a comprehensive melting and binary mixing model has been developed here. Details on parameters, calculations and results derived from this model are given in appendix 4. In the following discussion, the enriched- and depleted components used to model the observed geochemical- and isotopic variance will be addressed. Additionally, two different mixing scenarios will be discussed.

In my model, the enriched end-member of the 13º00'-13º36'N lavas is most successfully reproduced by ancient, recycled oceanic crust that has been preserved from mantle convection mixing for ~2 Ga. This calculated enriched component correspond to the HIMU component suggested by Wilson, Murton et al. (2013). Prominent depletions in fluid mobile elements (Pb, Rb, U, K, Th) and enrichment in immobile elements (Ta, Nb) in the data are coherent with metasomatism and slab modifications in the subduction zone for the enriched component. In terms of trace elements, the best match between the model values and data is seen for melting occurring in two stages beneath the ridge; (1) eclogite melting in the presence of garnet, and (2) melting of a peridotite source which has reacted with the eclogite melts. This model suggests reaction of early stage eclogite melts with olivine rich, ambient mantle to produce pyroxenite, which later re-melts to produce the enriched melts observed here. A similar scenario has been suggested for plume derived melts (Sobolev, Hofmann et al. 2005).

To obtain extreme $^{176}Hf/^{177}Hf$ values without strong depletions of other isotopic ratios (figure 18 and 23), the influence of a component analogous to the ReLish should be evaluated. This component is calculated in my model by partial melting in the presence of garnet, and has been unaffected by differentiation processes for ~2 Ga. An interesting outcome of this model is that the source of this ancient melting must be a relatively enriched mantle component. As further elaborated in Appendix 4, this component is compositionally extreme, and requires some buffering by a normal depleted ambient component to reproduce the data. Based on the different nature of this buffering agent, two different models are suggested as explanation for the observed 13º00'-13º36'N systematics.

- Model 1 assumes solid-state mixing between a depleted DMM component (UDMM) similar to that suggested by Wilson, Murton et al. (2013), and the ReLish component constituted here. The UDMM – ReLish proportion is estimated to be 75:35, and the enriched component is a pyroxenite component resulting from introduction of low-F eclogite melts to the ambient mantle.
- Model 2 assumes a scenario where both the enriched and the depleted components are buffered by low-F eclogite melts, resulting in a less extreme ReLish component with ReLish – eclogite melt.

Details on the results of these models are provided in appendix 4. As shown in the trace element – isotopic ratio plots in figure 24, some problems are still unresolved with both proposed models. However, a quick qualitative evaluation indicates a better match of model 2 with the data than model 1. The remaining discrepancies are essentially attributed to the nature of the depleted end-members, which appear to be too depleted in isotopic ratios (*e.g.* low $^{206}Pb/^{204}Pb$ and high $^{143}Nd/^{144}Nd$) and insufficiently depleted in trace element ratios (*e.g.* Ba/La and La/Sm) (figure 24). The lack of correlation between Gd/Yb and $^{206}Pb/^{204}Pb$ also suggest that the garnet effect is probably overestimated in the depleted end-member (particularly in model 1).

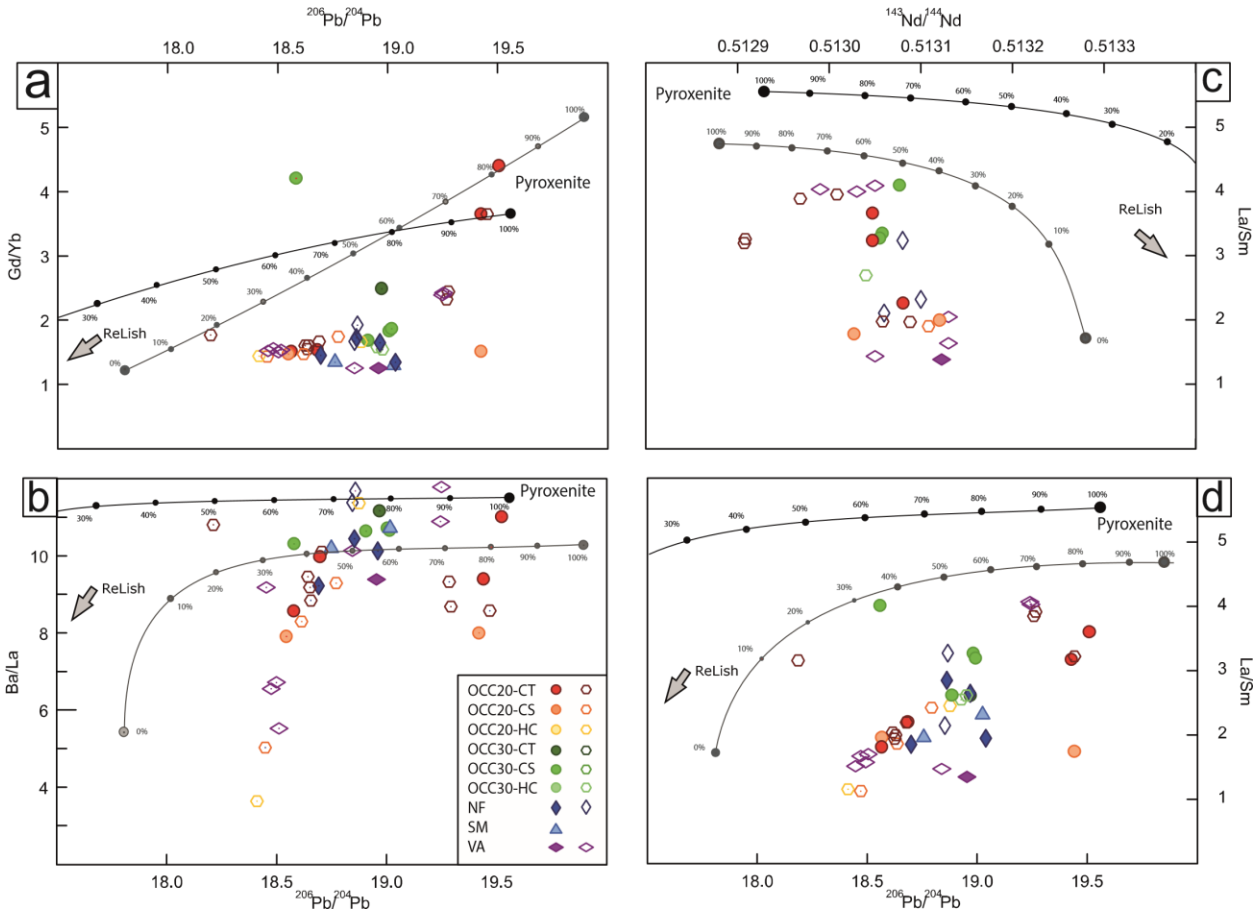

Figure 22: Trace element ratios versus isotopic ratios with closed symbols representing samples from this study and open symbols representing samples from Wilson, Murton et al. (2013). Modeled, binary mixing curves are displayed in black (model1) and grey (model 2), with 100% indicating complete dominance of the pyroxenite component and 0% representing a mantle exclusively made of the depleted component. (a) $^{206}Pb/^{204}Pb$ versus Gd/Yb with straight to concave-down mixing curves for model 2 and model 1 respectively, and a prominent concave up pattern seen in the data. Both models are excessively depleted in $^{206}Pb/^{204}Pb$, but model 2 exceeds model 1. (b) $^{206}Pb/^{204}Pb$ versus Ba/La plotting displaying discrepancy between the observed data for both model 1 and 2 in terms of extreme $^{206}Pb/^{204}Pb$ depletion. The model 2 trend also overestimate the Ba/La of the depleted end-member. (c) $^{143}Nd/^{144}Nd$ versus La/Sm, displaying extreme $^{143}Nd/^{144}Nd$ ratios in the modeled depleted end-members. (d) $^{206}Pb/^{204}Pb$ versus La/Sm, displaying similar, albeit less extreme discrepancy as in (b).

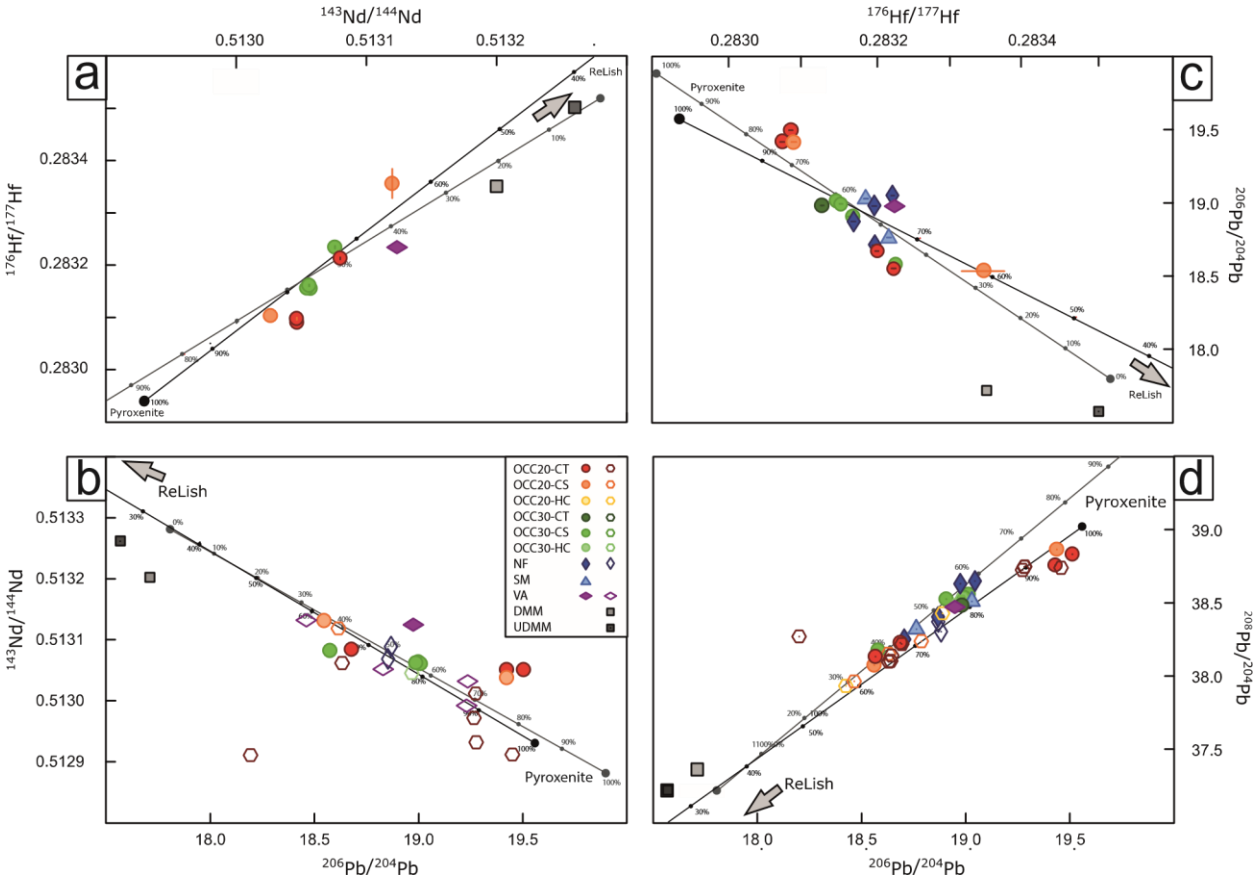

Figure 23: Isotopic ratios versus isotopic ratios with closed symbols representing samples from this study and open symbols representing samples from Wilson, Murton et al. (2013). Modeled, binary mixing curves are displayed in black (model1) and grey (model 2), (a) $^{206}Pb/^{204}Pb$ versus $^{176}Hf/^{177}H$. (b) $^{176}Hf/^{177}Hf$ versus $^{143}Nd/^{144}Nd$. (c) $^{176}Hf/^{177}Hf$ versus $^{206}Pb/^{204}Pb$. (d) $^{208}Pb/^{204}Pb$ versus $^{206}Pb/^{204}Pb$

Compared to the trace element systematics, the isotopic compositions estimated here largely match those observed in the data (figure 25). Of the two models presented here, the model 1 trend provides the best fit to the data in the $^{176}Hf/^{177}Hf$ dimension. However, as this model deviate slightly more than the model 2 trend in the remaining isotopic systems and significantly more in the trace element systematics, it is concluded here that some more work will be necessary to obtain a perfectly balanced petrogenetic model. The inadequate $^{176}Hf/^{177}Hf$ composition observed in both models may reflect (1) excessive melting of the garnet-bearing ReLish protolith, (2) underestimated isolation time of this residue from the bulk silicate earth reservoir, and (3) underestimated garnet concentrations in the ReLish protolith. It should be noted that the ReLish component constructed here is oversimplified. In agreement with previous theories proposed for this component (Hamelin, Bezos et al. 2013, Frey, Nobre Silva et al. 2015),

significant fluid – rock modifications attributed to pre-subduction alteration and subduction-related metasomatism is expected. It became clear from the model presented here that these parameters strongly influence the isotopic composition of the enriched, recycled component, which is considered the initial source of ReLish. Despite the large number of unknown parameters, the models presented here are still bringing new, useful constraints on the nature and importance of the ReLish component on the 13º00'-13º36'N source region.

6.3 Geochemical mapping

To unravel the complex nature of the detachment faults studied here it is essential to evaluate the relationship between geochemical signals and morphological patterns. One approach to this challenge is to merge geochemical information with geological observations. In this section, "geochemical maps" are presented and interpreted. These maps have been developed by plotting geochemical parameters (*e.g.* MgO, La/Sm_N, and $^{206}Pb/^{204}Pb$) on top of bathymetrical maps. A limitation of these maps is the overlapping data points in areas with high sampling density. If samples are collected within a limited area, they will appear as an overlapping cluster on the geochemical maps. This is particularly true for dredges as these represent a range of different rock samples, which end up plotting in the same position on the map. In giving priority to one end of the geochemical scale (*i.e.* the lower end or the higher end), the remaining compositions may be partially or completely concealed. It is therefore noted that by carefully choosing the order in which overlapping samples are plotted, it is possible to highlight certain geochemical features. To fulfill the potential of these geochemical maps, it is essential that the exact position of each sample is known. This is the case for samples collected by a ROV. It is also necessary to consider if the sample was collected *in-situ* as a part of an outcrop or as a lose rock. The challenge associated with high density sampling may be overcome by plotting these data on micro-bathymetry maps, thereby increasing the relative distance between samples.

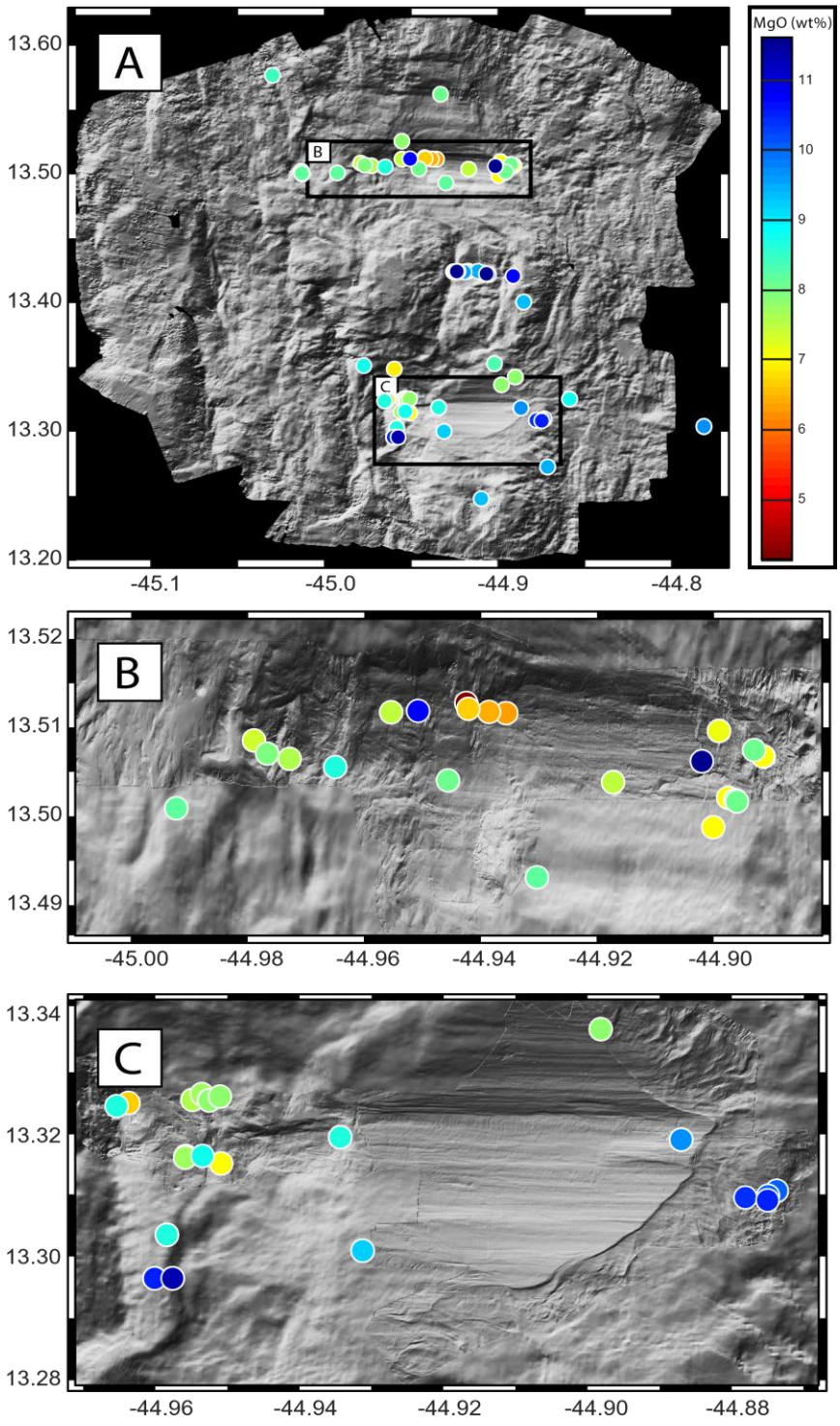

Figure 24: Geological maps displaying a large variation in MgO (wt. %), with higher values superimposed on lower values when multiple samples are found in the same places. (a) Regional geochemical map of the 13º00' – 13º36' N area displaying general decrease in MgO towards north. Inter-OCC lavas and axial valley lavas are more MgO-rich than OCC20- and OCC30 lavas. (b) High-resolution geochemical map of the OCC30 displaying a random distribution samples with different composition. (c) High-resolution geochemical map of OCC20, with equally random distribution of samples with different composition. The less-evolved samples associated with the detachment fault are constrained to a limited area in the chaotic terrain.

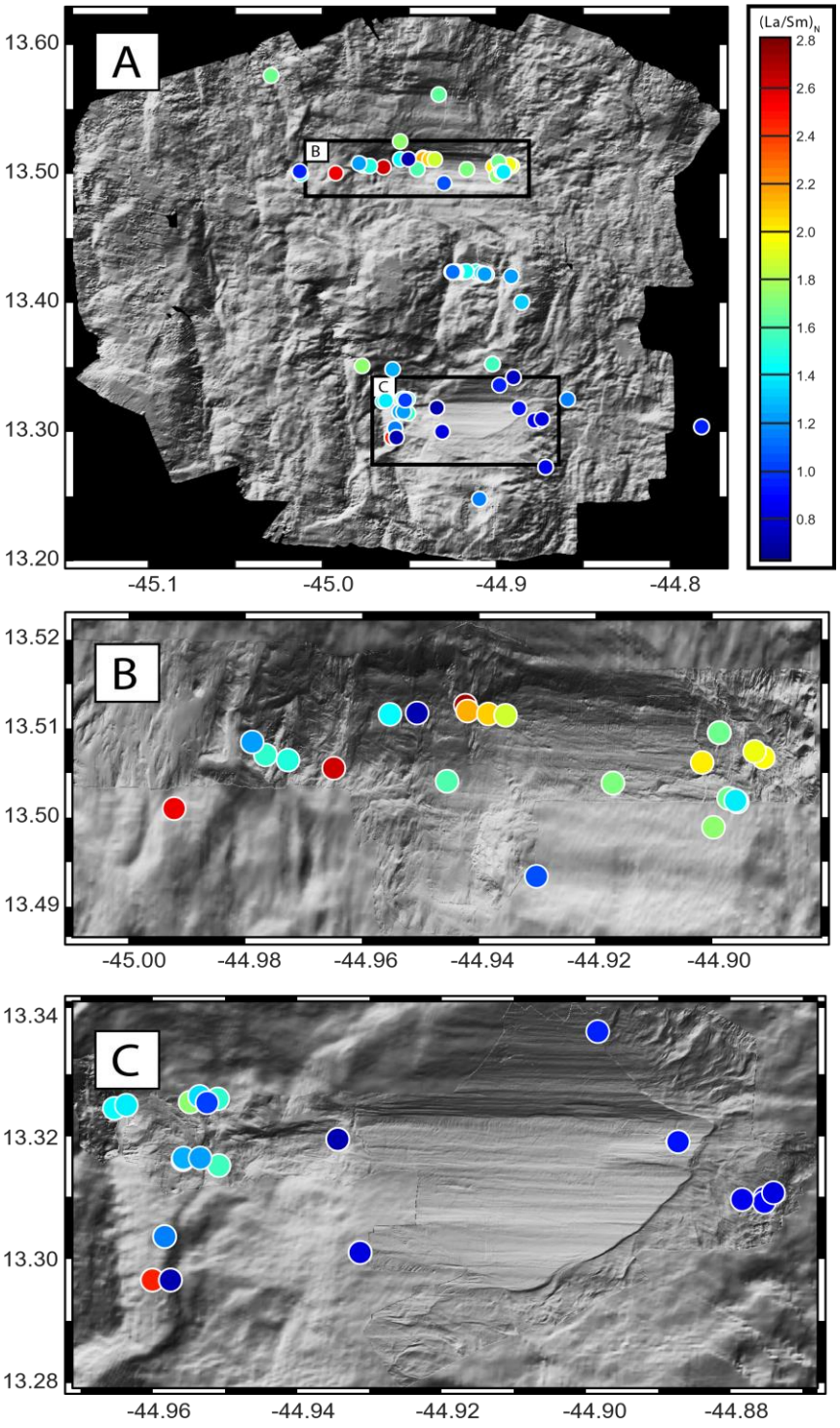

Figure 25: Geological maps displaying a large variation in La/Sm$_N$, with lower values superimposed on lower values when multiple samples are found in the same places. (a) Regional geochemical map of the 13º00' – 13º36' N area displaying general increase in La/Sm$_N$ towards north. Axial valley lavas appear more depleted than inter-OCC lavas. The most enriched samples are restricted to the west-end of the detachment fault (b) High-resolution geochemical map of the OCC30 displaying a random distribution samples with different composition. (c) High-resolution geochemical map of OCC20, showing relatively homogenous REE ratios with the exception of the chaotic terrain.

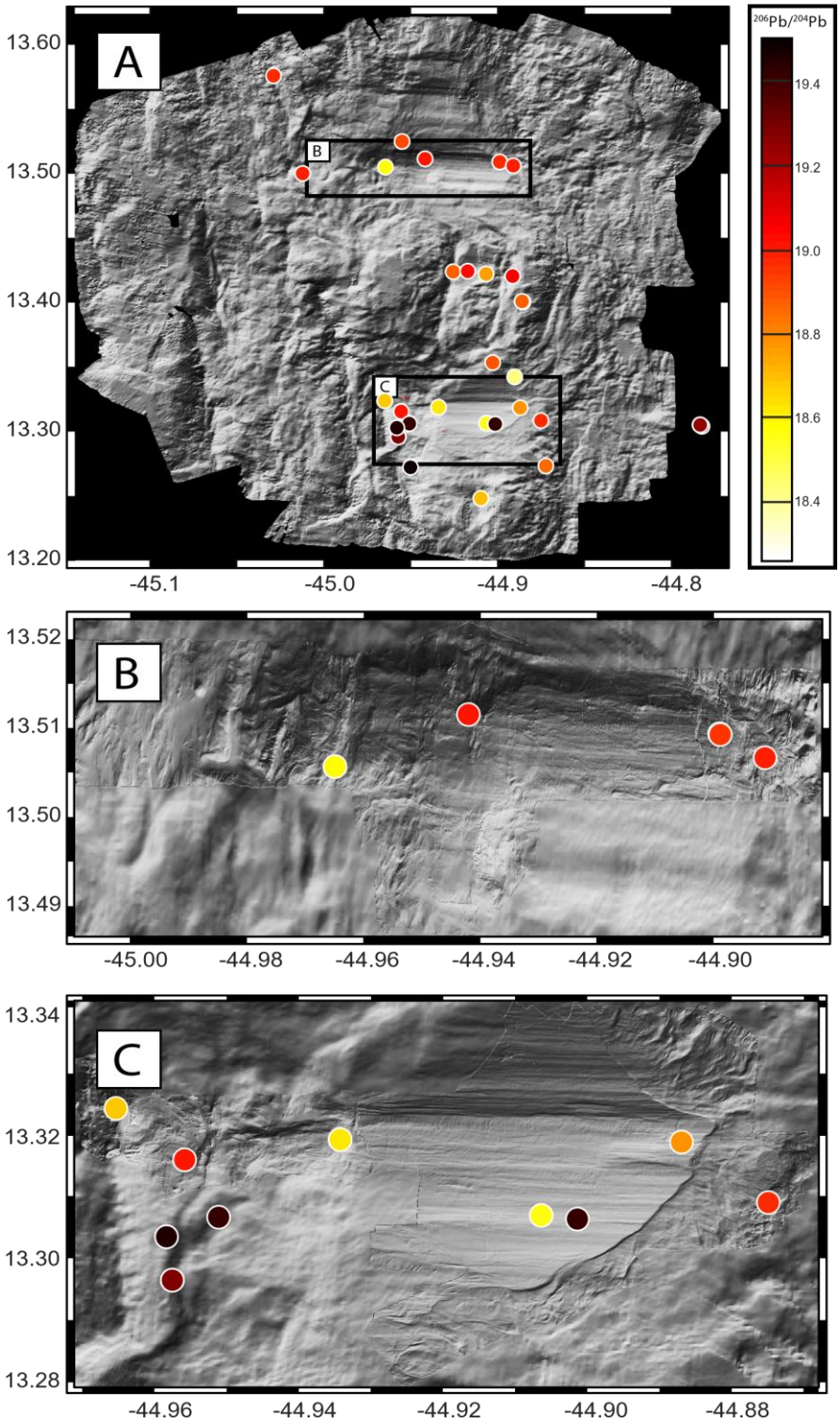

Figure 26: Geological maps displaying a large variation in $^{206}Pb/^{204}Pb$, with higher values superimposed on lower values when multiple samples are found in the same places. (a) Regional geochemical map of the 13º00' – 13º36' N area displaying general increase in $^{206}Pb/^{204}Pb$ towards south. The most enriched samples ($^{206}Pb/^{204}Pb$ > 19.4) and the most depleted samples ($^{206}Pb/^{204}Pb$ < 18.6) are restricted to OCC20. Axial valley lavas and inter-OCC lavas are intermediate between the most enriched and most depleted samples of their detachment faults. (b) High-resolution geochemical map of the OCC30. (c) High-resolution geochemical map of OCC20.

It became clear from the previous chapter that the variance observed in 13º00'-13º36'N basalt samples can be traced to source heterogeneity. I also concluded that the influence of the enriched source was most pronounced in samples from the chaotic terrains and the upper corrugated surface in OCC20 and OCC30, and in some AV lavas. Escartin et al., (2017) argued that hanging-wall material is continuously emplaced onto the detachment fault as a function of fault rotation. This is defining the relative chronology of the lose lava debris collected along those OCCs. Wilson et al., (2013) concluded that older lavas, associated with the chaotic terrain, were enriched compared to more recent eruptions. According to this model, a gradual decrease in La/Sm_N is expected eastward along the detachment surface. This is not, however the observation made from the geochemical maps of the OCC20 and OCC30 (figure 26, 27, and 28). Rather, a more scattered distribution of samples is seen in both detachment faults. Depleted samples are observed in all domains of the detachment fault, and some of the most enriched and depleted samples are located within the same confined areas (*e.g.* samples ODM-ROC-V550-156 and ODM-ROC-V550-160 on OCC20). The lack of a gradual transition from enriched to depleted is particularly clear in the $^{206}Pb/^{204}Pb$ map (figure 28). These observations are consistent with a complex post-melting history. Escartín, Mével et al. (2017) argued that the distribution of rocks atop the detachment faults reflects a combination of (1) mass wasting from the fault scarp, and (2) mass wasting associated with the hanging-wall "pinch-off". According to this theory, pieces of the oceanic crust are transferred onto the detachment fault either from debris filled trench at the fault termination or from the adjacent hanging-wall (figure 29). The implication of this assumption is that rocks deposited onto the detachment at any given time may represent both hanging-wall and footwall material, in good agreement with the observed random distribution of geochemical variations, particularly along OCC30.

Another observation appearing from the geochemical maps is the relative geochemical coherence between *in-situ* samples collected within a restricted area. These characteristics are most prominent in the axial valley lavas near the OCC20 hanging-wall cutoff and the lavas collected along the seamount. A similarity between all compositionally consistent clusters of basalt is that they are mostly high MgO (*i.e.* primitive). To account for these observations, it is reasonable to consider a scenario where the described homogenous, primitive lavas were transported through crust without significant modification.

In the previous section AV lavas, SM lavas, and one OCC30-CS sample have been described to be similar in terms of major- and trace elements as well as isotopic ratios. One could assume that since the normal fault seamount is located at the same longitude as the OCC20 breakaway zone, these melts were erupted within a short time frame at the ridge axis. However, the new dataset presented here shows that SM lavas and lavas associated with the detachment faults are very different. Escartín, Mével et al. (2017) used the thickness of sediment cover and the geometry of the inter-OCC seamount as age constraints for these *in-situ* basalts. Owing to the thin sediment cover and flat-topped appearance of the seamount in an otherwise fault-rotated region, these authors attributed the seamount lavas to more recent, off-axis volcanism. Considering the similarity of SM- and some AV lavas (ODM-ROC-V557- [098-101]) , (figure 11, 13, 15, 16, and 18), it is likely that these lavas are indeed related (*i.e.* source composition, melting extent, transport path and time of eruption).

The presence of axial lavas several kilometers off the ridge axis could be explained by assuming the existence of channelized melt flow through permeable conduits in the oceanic lithosphere. The seamount is situated in the half-graben of a large, high-angle normal fault. It is thus likely that the homogeneous high-Mg lavas migrated relatively rapidly from source to surface through the permeable fault zone. Melt transport has been suggested to occur along valley faults at ultra-slow-spreading settings, producing young off-axis volcanism (Standish and Sims 2010). Assuming this theory holds, the normal fault "hosting" this seamount must be rooted in the injection zone beneath the ridge axis (figure 29). Indeed, this fault has been suggested to be the precursor of an future detachment fault (Smith, Escartín et al. 2008). A similar scenario may account for the high-Mg, homogeneous enriched OCC20-CT lavas (figure 12 and 19), as fissures and fault scarps are common in the chaotic terrain of OCC20 (Escartín, Mével et al. 2017). OCC20-CT melts have most likely experienced similar migration through the crust as SM lavas. I suggest that the OCC20 area resembled the inter-OCC normal fault at the onset of detachment faulting.

It is important to consider the impact of such dispersed volcanism on the formation of detachment faults. If part of the melt escapes from the ridge axis to create off-axis seamounts like in our studied area, it might reduce the magma supply available for magmatic spreading along the axis. Ultimately, this unfocused magmatism might have an important role to trigger the

formation of an OCC. This hypothesis is opening a new field of research to study further these geological objects.

6.4 Geodynamic model

In their conceptual model for OCC development, Wilson, Murton et al. (2013) argued for reduced magmatism and thus also reduced crustal strength as a direct consequence of bimodal mantle melting. According to these authors, reduced magmatism is attributed to latent heat of fusion of the enriched component, followed by heat deficiency and magma starvation. The transition from a source significantly influenced by an enriched component to one devoid of this component has been argued the ultimate driving force for OCC formation. In the previous chapter, the importance of source heterogeneity, melting and melt focusing were evaluated in regards of the spatio-temporal chemical variation in the 13°00 – 13°36'N section of the MAR. It becomes clear from this discussion that the link between source composition and the formation of OCC is anything but straightforward. It follows that the existing geochemical model, suggesting a direct link between mantle heterogeneities and OCC formation (Wilson, Murton et al. 2013) should be re-evaluated.

The results from this study support the assumption that fluctuations in the source composition have a significant influence on the formation and evolution of the detachment faults. However physical transport and magma "leakage" to off-axis volcanism might also influence on-axis melt supply. To demonstrate this complex relationship and summarize the outcomes of this discussion, a comprehensive geodynamic model adapted from Escartin et al., (2017) is proposed (figure 29). In this model, the initiation, evolution, and termination of detachment faults in the 13°00'- 23°36'N area can be described by the following stages:

a. Melting in the presence of pyroxenite pockets, generating lava volumes sufficient for significant magmatic crustal accretion. Emplacement of both enriched and depleted lava within a limited time-frame, possibly accompanied by off-axis magmatism, generating the future chaotic terrain.
b. Reduced influence of pyroxenite and increased influence of a refractory, ReLish-like component in the melting column, intensifying the on-axis melt starvation. Strain focusing on single, existing faults, which eventually extend to the asthenosphere,

enabling fluid infiltration, and talc formation. Mass wasting from the fault scarp and progressive fault scarp retreat.

c. Enduring melt starvation and rotation of the fault scarp, resulting in exhumation of the lower oceanic crust and lithospheric mantle.
d. Continued fault rotation and emplacement of hanging-wall blocks onto the dome shaped fault plane along with other mass wasting material from the apron, forming an intermittent rubble cover. Reduced influence of ReLish and increased influence of DMM.
e. Reappearance of enriched mantle and enhanced melt production reduces the tectonic strain and causes new, high-angle faults break the surface of OCC30.

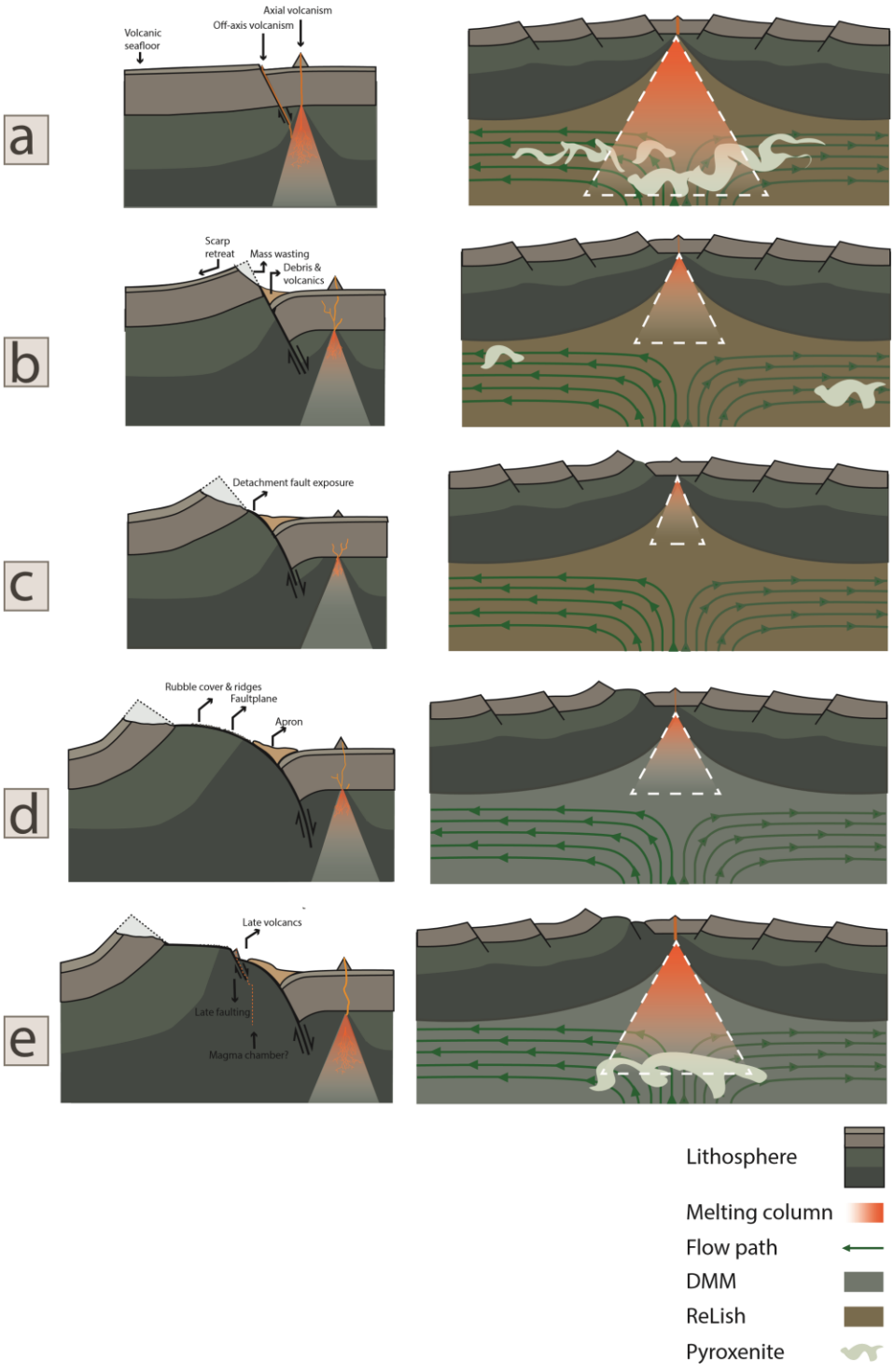

Figure 27: Geodynamic model of spatio-temporal evolution of the study area. Large-scale cross-section of the lithosphere and mantle (right). Small-scale cross-section of the lithosphere on the left ridge flank (left). Detailed description of the different steps is given in the text.

7. Conclusion

This study presents a model for local, spatio-temporal MORB variation in a ridge section dominated by two detachment faults. The data presented here suggest that the MORB variation in the 13º00'N – 13º36'N region of the MAR are far from straightforward. The following factors are suggested to control the observed MORB variation:

- Varying extents of fractional crystallization
- Different melting depths and melting extents
- Different degrees of melt mixing
- Complex melt transport mechanisms
- Heterogeneities within the melting source

To reproduce the range in trace element composition and isotopic ratios, a multi-component source is needed. The enriched source is believed to be an ancient (~2 Ga) oceanic crust material. Enriched melts are suggested to reflect a two-stage melting scenario, involving:

- Melting of recycled oceanic crust (eclogite) and re-enrichment of the ambient refractory mantle by melt-rock interaction.
- Melting of the resulting pyroxenite to form E-MORBs.

The depleted source may be subdivided into two domains. The presence of a ReLish (Residual Lithosphere) component in the mantle successfully reproduces the anomalous $^{176}Hf/^{177}Hf$ on 13º00' – 13º36'N. This component is believed to be a garnet bearing mantle residue, which has been isolated from convectional mixing for ~ 2 Ga. The source of this ancient ReLish melting event is believed to be an enriched mantle component, similar to what is found under a hotspot. Whether or not this ReLish component is nowadays coexisting with a regular depleted MORB upper mantle remains unclear.

Geochemical maps reveal that near-primary melts occur in fault-disrupted areas, interpreted here to reflect fault driven melt transport. It is further inferred that off-axis, fault related volcanism has importance for the initiation of detachment faults. A transition from focused to unfocused melt transport along deep-seated normal faults is suggested here to enhance magma starvation at

the ridge axis. Unlike previous conclusions made for OCC20 and OCC30, this study proposes a combination of geochemical – and structural control on the formation of these faults.

Further research should include a higher sampling density in the axial valley. By expanding the dataset to the ridge axis, recent geochemical evolution of the study area could be evaluated. This is essential for a comprehensive understanding of the study area.

8. References

Allegre, C. J. and D. L. Turcotte (1986). "Implications of a two-component marble-cake mantle." Nature **323**(6084): 123-127.

Andres, M., J. Blichert-Toft and J.-G. Schilling (2004). "Nature of the depleted upper mantle beneath the Atlantic: evidence from Hf isotopes in normal mid-ocean ridge basalts from 79°N to 55°S." Earth and Planetary Science Letters **225**(1-2): 89-103.

Becker, J. S. (2007). Introduction to Mass Spectrometry. Inorganic Mass Spectrometry, John Wiley & Sons, Ltd**:** 1-6.

Blichert-Toft, J., A. Agranier, M. Andres, R. Kingsley, J.-G. Schilling and F. Albarède (2005). "Geochemical segmentation of the Mid-Atlantic Ridge north of Iceland and ridge–hot spot interaction in the North Atlantic." Geochemistry, Geophysics, Geosystems **6**(1): n/a-n/a.

Boschi, C., G. L. Früh-Green, A. Delacour, J. A. Karson and D. S. Kelley (2006). "Mass transfer and fluid flow during detachment faulting and development of an oceanic core complex, Atlantis Massif (MAR 30°N)." Geochemistry, Geophysics, Geosystems **7**(1): n/a-n/a.

Buck, W. R., L. L. Lavier and A. N. B. Poliakov (2005). "Modes of faulting at mid-ocean ridges." Nature **434**(7034): 719-723.

Cann, J. R., D. K. Blackman, D. K. Smith, E. McAllister, B. Janssen, S. Mello, E. Avgerinos, A. R. Pascoe and J. Escartin (1997). "Corrugated Slip Surfaces Formed at Ridge-Transform Intersections on the Mid-Atlantic Ridge." Nature **385**(6614): 329-332.

Cannat, M., D. Sauter, J. Escartín, L. Lavier and S. Picazo (2009). "Oceanic corrugated surfaces and the strength of the axial lithosphere at slow spreading ridges." Earth and Planetary Science Letters **288**(1–2): 174-183.

Cannat, M., D. Sauter, V. Mendel, E. Ruellan, K. Okino, J. Escartin, V. Combier and M. Baala (2006). "Modes of seafloor generation at a melt-poor ultraslow-spreading ridge." Geology **34**(7): 605-608.

Ciazela, J., J. Koepke, J. B. Dick Henry and A. Muszynski (2015). Mantle rock exposures at oceanic core complexes along mid-ocean ridges. Geologos. **21:** 207.

Dick, H. J. B., J. Lin and H. Schouten (2003). "An ultraslow-spreading class of ocean ridge." Nature **426**(6965): 405-412.

Dick, H. J. B., M. A. Tivey and B. E. Tucholke (2008). "Plutonic foundation of a slow-spreading ridge segment: Oceanic core complex at Kane Megamullion, 23°30'N, 45°20'W." Geochemistry, Geophysics, Geosystems **9**(5): n/a-n/a.

Donnelly, K. E., S. L. Goldstein, C. H. Langmuir and M. Spiegelman (2004). "Origin of enriched ocean ridge basalts and implications for mantle dynamics." Earth and Planetary Science Letters **226**(3-4): 347-366.

Dupre, B. and C. J. Allegre (1983). "Pb-Sr isotope variation in Indian Ocean basalts and mixing phenomena." Nature **303**(5913): 142-146.

Escartín, J. and J. P. Canales (2011). "Detachments in Oceanic Lithosphere: Deformation, Magmatism, Fluid Flow, and Ecosystems." Eos, Transactions American Geophysical Union **92**(4): 31-31.

Escartín, J., C. Mével, C. J. MacLeod and A. M. McCaig (2003). "Constraints on deformation conditions and the origin of oceanic detachments: The Mid-Atlantic Ridge core complex at 15°45'N." Geochemistry, Geophysics, Geosystems **4**(8): n/a-n/a.

Escartín, J., C. Mével, S. Petersen, D. Bonnemains, M. Cannat, M. Andreani, N. Augustin, A. Bezos, V. Chavagnac, Y. Choi, M. Godard, K. Haaga, C. Hamelin, B. Ildefonse, J. Jamieson, B. John, T. Leleu, C. J. MacLeod, M. Massot-Campos, P. Nomikou, J. A. Olive, M. Paquet, C. Rommevaux, M. Rothenbeck, A. Steinfuhrer, M. Tominaga, L. Triebe, R. Campos, N. Gracias and R. Garcia (2017). "Tectonic structure, evolution, and the nature of oceanic core complexes and their detachment fault zones (13°20'N and 13°30'N, Mid Atlantic Ridge)." Geochemistry, Geophysics, Geosystems **18**(4): 1451-1482.

Escartin, J., D. K. Smith, J. Cann, H. Schouten, C. H. Langmuir and S. Escrig (2008). "Central role of detachment faults in accretion of slow-spreading oceanic lithosphere." Nature **455**(7214): 790-794.

Forsyth, D. W. and C. Langmuir (2007). "Mantle melting beneath mid-ocean ridges."

Frey, F. A., I. G. Nobre Silva, S. Huang, M. S. Pringle, P. R. Meleney and D. Weis (2015). "Depleted components in the source of hotspot magmas: Evidence from the Ninetyeast Ridge (Kerguelen)." Earth and Planetary Science Letters **426**: 293-304.

Gale, A., S. Escrig, E. J. Gier, C. H. Langmuir and S. L. Goldstein (2011). "Enriched basalts at segment centers: The Lucky Strike (37°17'N) and Menez Gwen (37°50'N) segments of the Mid-Atlantic Ridge." Geochemistry, Geophysics, Geosystems **12**(6): n/a-n/a.

Gill, R. (2010). Igneous Rocks and Processes: A Practical Guide.

Goldschmidt, V. (1954). "Geochemistry: Oxford University Press." Fair Lawn, NJ.

Hamelin, C., A. Bezos, L. Dosso, J. Escartin, M. Cannat and C. Mevel (2013). "Atypically depleted upper mantle component revealed by Hf isotopes at Lucky Strike segment." Chemical Geology **341**: 128-139.

Hamelin, C., L. Dosso, B. B. Hanan, M. Moreira, A. P. Kositsky and M. Y. Thomas (2011). "Geochemical portray of the Pacific Ridge: New isotopic data and statistical techniques." Earth and Planetary Science Letters **302**(1–2): 154-162.

Hanan, B. B. and D. W. Graham (1996). "Lead and Helium Isotope Evidence from Oceanic Basalts for a Common Deep Source of Mantle Plumes." Science **272**(5264): 991-995.

Hannigan, R. E., A. R. Basu and F. Teichmann (2001). "Mantle reservoir geochemistry from statistical analysis of ICP-MS trace element data of equatorial mid-Atlantic MORB glasses." Chemical Geology **175**(3–4): 397-428.

Hanson, G. N. and C. H. Langmuir (1978). "Modelling of major elements in mantle-melt systems using trace element approaches." Geochimica et Cosmochimica Acta **42**(6): 725-741.

Hart, A. Z. a. S. (1986). "Chemical Geodynamics." Annual Review of Earth and Planetary Sciences **14**: 493-571.

Hart, S. R. (1984). "A large-scale isotope anomaly in the Southern Hemisphere mantle." Nature **309**(5971): 753-757.

Hart, S. R. (1988). "Heterogeneous mantle domains: signatures, genesis and mixing chronologies." Earth and Planetary Science Letters **90**(3): 273-296.

Hart, S. R., E. H. Hauri, L. A. Oschmann and J. A. Whitehead (1992). "Mantle Plumes and Entrainment: Isotopic Evidence." Science **256**(5056): 517-520.

Hauri, E. H. and S. R. Hart (1993). "ReOs isotope systematics of HIMU and EMII oceanic island basalts from the south Pacific Ocean." Earth and Planetary Science Letters **114**(2): 353-371.

Hedge, C. E. and F. G. Walthall (1963). "Radiogenic Strontium-87 as an Index of Geologic Processes." Science **140**(3572): 1214-1217.

Hellebrand, E., J. E. Snow, P. Hoppe and A. W. Hofmann (2002). "Garnet-field Melting and Late-stage Refertilization in 'Residual' Abyssal Peridotites from the Central Indian Ridge." Journal of Petrology **43**(12): 2305-2338.

Hirschmann, M. M. and E. M. Stolper (1996). "A possible role for garnet pyroxenite in the origin of the "garnet signature" in MORB." Contributions to Mineralogy and Petrology **124**(2): 185-208.

Hofmann, A. W. (1988). "Chemical differentiation of the Earth: the relationship between mantle, continental crust, and oceanic crust." Earth and Planetary Science Letters **90**(3): 297-314.

Hofmann, A. W. (1997). "Mantle geochemistry: the message from oceanic volcanism." Nature **385**(6613): 219-229.

Hofmann, A. W. (2007). 2.03 - Sampling Mantle Heterogeneity through Oceanic Basalts: Isotopes and Trace Elements A2 - Holland, Heinrich D. Treatise on Geochemistry. K. K. Turekian. Oxford, Pergamon**:** 1-44.

Hofmann, A. W. and W. M. White (1982). "Mantle plumes from ancient oceanic crust." Earth and Planetary Science Letters **57**(2): 421-436.

Ildefonse, B., B. E. D.K. Blackman, Y. John, D. J. M. Ohara and C.J. MacLeod (2007). "Oceanic core complexes and crustal accretion at slow-spreading ridges." **35**(7): 623-626.

Jacob, D. E. and S. F. Foley (1999). "Evidence for Archean ocean crust with low high field strength element signature from diamondiferous eclogite xenoliths." Lithos **48**(1–4): 317-336.

Jakubowski, N., T. Prohaska, L. Rottmann and F. Vanhaecke (2011). "Inductively coupled plasma- and glow discharge plasma-sector field mass spectrometry Part I. Tutorial: Fundamentals and instrumentation." Journal of Analytical Atomic Spectrometry **26**(4): 693-726.

Karson, J. A., and Dick, H.J.B (1983). "Tectonics of a ridge- transform intersection at the Kane fracture zone." Marine Geophysical Researches **6**: 51-98.

Karson, J. A., N. White, L. Curry, D. McKenzie, R. S. White, A. B. Watts, N. Kusznir, K. E. Louden and R. Buck (1999). "Geological Investigation of a Lineated Massif at the Kane Transform Fault: Implications for Oceanic Core Complexes [and Discussion]." Philosophical Transactions: Mathematical, Physical and Engineering Sciences **357**(1753): 713-740.

Kelemen, P. B., G. Hirth, N. Shimizu, M. Spiegelman and H. J. B. Dick (1997). "A Review of Melt Migration Processes in the Adiabatically Upwelling Mantle beneath Oceanic Spreading Ridges." Philosophical Transactions: Mathematical, Physical and Engineering Sciences **355**(1723): 283-318.

Kimura, J.-I., J. B. Gill, S. Skora, P. E. van Keken and H. Kawabata (2016). "Origin of geochemical mantle components: Role of subduction filter." Geochemistry, Geophysics, Geosystems **17**(8): 3289-3325.

Klein, E. M. (2003). 3.13 - Geochemistry of the Igneous Oceanic Crust A2 - Holland, Heinrich D. Treatise on Geochemistry. K. K. Turekian. Oxford, Pergamon**:** 433-463.

Klein, E. M. (2003). Geochemistry of the Igneous Oceanic Crust, Elsevier.

Klein, E. M. and C. H. Langmuir (1989). "Local versus global variations in ocean ridge basalt composition: A reply." Journal of Geophysical Research: Solid Earth **94**(B4): 4241-4252.

Koornneef, J. M., A. Stracke, B. Bourdon, M. A. Meier, K. P. Jochum, B. Stoll and K. Grönvold (2011). "Melting of a Two-component Source beneath Iceland." Journal of Petrology **53**(1): 127-157.

Langmuir, C. K., EM ; Plank, T (1992). "Mantle Flow and Melt Generation at Mid-Ocean Ridges." (71): 183-280.

Luqman, M., Inamuddin (2012). Ion Exchange Technology II: Applications, Springer Netherlands.

Maclennan, J. (2008). "Lead isotope variability in olivine-hosted melt inclusions from Iceland." Geochimica et Cosmochimica Acta **72**(16): 4159-4176.

MacLeod, C. J., J. Carlut, J. Escartín, H. Horen and A. Morris (2011). "Quantitative constraint on footwall rotations at the 15°45'N oceanic core complex, Mid-Atlantic Ridge: Implications for oceanic detachment fault processes." Geochemistry, Geophysics, Geosystems **12**(5): n/a-n/a.

MacLeod, C. J., J. Escartín, D. Banerji, G.J. Banks, M. Gleeson, D.H.B. Irving, R.M. Lilly, A.M. McCaig, Y. Niu, S. Allerton and D. K. Smith (2002). "Direct geological evidence for oceanic detachment faulting: The Mid-Atlantic Ridge, 15°45'N." Geological Society of America Bulletin **30**(10): 879-882.

MacLeod, C. J., R. C. Searle, B. J. Murton, J. F. Casey, C. Mallows, S. C. Unsworth, K. L. Achenbach and M. Harris (2009). "Life cycle of oceanic core complexes." Earth and Planetary Science Letters **287**(3–4): 333-344.

Manhes, G., J. F. Minster and C. J. Allègre (1978). "Comparative uranium-thorium-lead and rubidium-strontium study of the Saint Sèverin amphoterite: consequences for early solar system chronology." Earth and Planetary Science Letters **39**(1): 14-24.

Michael, P. J., C. H. Langmuir, H. J. B. Dick, J. E. Snow, S. L. Goldstein, D. W. Graham, K. Lehnert, G. Kurras, W. Jokat, R. Muhe and H. N. Edmonds (2003). "Magmatic and amagmatic seafloor generation at the ultraslow-spreading Gakkel ridge, Arctic Ocean." Nature **423**(6943): 956-961.

Müller, R. D., M. Sdrolias, C. Gaina and W. R. Roest (2008). "Age, spreading rates, and spreading asymmetry of the world's ocean crust." Geochemistry, Geophysics, Geosystems **9**(4): n/a-n/a.

Nobre Silva, I. G., D. Weis and J. S. Scoates (2010). "Effects of acid leaching on the Sr-Nd-Hf isotopic compositions of ocean island basalts." Geochemistry, Geophysics, Geosystems **11**(9): n/a-n/a.

Pertermann, M., M. M. Hirschmann, K. Hametner, D. Günther and M. W. Schmidt (2004). "Experimental determination of trace element partitioning between garnet and silica-rich liquid during anhydrous partial melting of MORB-like eclogite." Geochemistry, Geophysics, Geosystems **5**(5): n/a-n/a.

Plank, T. and C. H. Langmuir (1992). "Effects of the melting regime on the composition of the oceanic crust." Journal of Geophysical Research: Solid Earth **97**(B13): 19749-19770.

Reston, T. J. and C. R. Ranero (2011). "The 3-D geometry of detachment faulting at mid-ocean ridges." Geochemistry, Geophysics, Geosystems **12**(7): n/a-n/a.

Robinson, J. A. C. and B. J. Wood (1998). "The depth of the spinel to garnet transition at the peridotite solidus." Earth and Planetary Science Letters **164**(1–2): 277-284.

Rubin, K. H., J. M. Sinton, J. Maclennan and E. Hellebrand (2009). "Magmatic filtering of mantle compositions at mid-ocean-ridge volcanoes." Nature Geosci **2**(5): 321-328.

Salters, V. J. M., S. Mallick, S. R. Hart, C. E. Langmuir and A. Stracke (2011). "Domains of depleted mantle: New evidence from hafnium and neodymium isotopes." Geochemistry, Geophysics, Geosystems **12**(8): n/a-n/a.

Salters, V. J. M. and A. Stracke (2004). "Composition of the depleted mantle." Geochemistry, Geophysics, Geosystems **5**(5): n/a-n/a.

Schreiber, H. D. (1986). "Redox processes in glass-forming melts." Journal of Non-Crystalline Solids **84**(1): 129-141.

Sen, G. (2014). Petrology: Principles and Practice. New-Delhi, India, Springer-Verlag Berlin Heidelberg.

Smith, D. (2013). "Tectonics: Mantle spread across the sea floor." Nature Geosci **6**(4): 247-248.

Smith, D. K., J. R. Cann and J. Escartin (2006). "Widespread active detachment faulting and core complex formation near 13 degrees N on the Mid-Atlantic Ridge." Nature **442**(7101): 440-443.

Smith, D. K., J. R. Cann and J. Escartin (2006). "Widespread active detachment faulting and core complex formation near 13[deg][thinsp]N on the Mid-Atlantic Ridge." Nature **442**(7101): 440-443.

Smith, D. K., J. Escartín, H. Schouten and J. R. Cann (2008). "Fault rotation and core complex formation: Significant processes in seafloor formation at slow-spreading mid-ocean ridges (Mid-Atlantic Ridge, 13°–15°N)." Geochemistry, Geophysics, Geosystems **9**(3): n/a-n/a.

Sobolev, A. V., A. W. Hofmann and I. K. Nikogosian (2000). "Recycled oceanic crust observed in /`ghost plagioclase/' within the source of Mauna Loa lavas." Nature **404**(6781): 986-990.

Sobolev, A. V., A. W. Hofmann, S. V. Sobolev and I. K. Nikogosian (2005). "An olivine-free mantle source of Hawaiian shield basalts." Nature **434**(7033): 590-597.

Standish, J. J. and K. W. W. Sims (2010). "Young off-axis volcanism along the ultraslow-spreading Southwest Indian Ridge." Nature Geosci **3**(4): 286-292.

Stracke, A. (2012). "Earth's heterogeneous mantle: A product of convection-driven interaction between crust and mantle." Chemical Geology **330–331**: 274-299.

Stracke, A., M. Bizimis and V. J. M. Salters (2003). "Recycling oceanic crust: Quantitative constraints." Geochemistry, Geophysics, Geosystems **4**(3): n/a-n/a.

Stracke, A. and B. Bourdon (2009). "The importance of melt extraction for tracing mantle heterogeneity." Geochimica et Cosmochimica Acta **73**(1): 218-238.

Stroobrant, E. d. H. a. V. (2007). Mass Spectrometry - Principles and Applications, Third Edition. The Artiut, Southern Gatye, Chichester West Sussex PO198SQ, England, JohnWiley & Sons, Ltd.

Sun, S.-s. and W. F. McDonough (1989). "Chemical and isotopic systematics of oceanic basalts: implications for mantle composition and processes." Geological Society, London, Special Publications **42**(1): 313-345.

Tang, M., W. F. McDonough and R. D. Ash (2017). "Europium and strontium anomalies in the MORB source mantle." Geochimica et Cosmochimica Acta **197**: 132-141.

Tatsumoto, M., C. E. Hedge and A. E. J. Engel (1965). "Potassium, Rubidium, Strontium, Thorium, Uranium, and the Ratio of Strontium-87 to Strontium-86 in Oceanic Tholeiitic Basalt." Science **150**(3698): 886-888.

Thompson, R. N., M. A. Morrison, G. L. Hendry, S. J. Parry, P. R. Simpson, R. Hutchison and M. J. O'Hara (1984). "An Assessment of the Relative Roles of Crust and Mantle in Magma Genesis: An Elemental Approach [and Discussion]." Philosophical Transactions of the Royal Society of London. Series A, Mathematical and Physical Sciences **310**(1514): 549-590.

Todd, E., A. Stracke and E. E. Scherer (2015). "Effects of simple acid leaching of crushed and powdered geological materials on high-precision Pb isotope analyses." Geochemistry, Geophysics, Geosystems **16**(7): 2276-2302.

Tucholke, B. E., M. D. Behn, W. R. Buck and J. Lin (2008). "Role of melt supply in oceanic detachment faulting and formation of megamullions." Geology **36**(6): 455-458.

Tucholke, B. E., K. Fujioka, T. Ishihara, G. Hirth and M. Kinoshita (2001). "Submersible study of an oceanic megamullion in the central North Atlantic." Journal of Geophysical Research: Solid Earth **106**(B8): 16145-16161.

Tucholke, B. E., J. Lin and M. C. Kleinrock (1998). "Megamullions and mullion structure defining oceanic metamorphic core complexes on the Mid-Atlantic Ridge." Journal of Geophysical Research: Solid Earth **103**(B5): 9857-9866.

Wang, Z. and G. A. Gaetani (2008). "Partitioning of Ni between olivine and siliceous eclogite partial melt: experimental constraints on the mantle source of Hawaiian basalts." Contributions to Mineralogy and Petrology **156**(5): 661-678.

Weill, D. F. and M. J. Drake (1973). "Europium Anomaly in Plagioclase Feldspar: Experimental Results and Semiquantitative Model." Science **180**(4090): 1059-1060.

White, W. M. (1985). "Sources of oceanic basalts: Radiogenic isotopic evidence." Geology **13**(2): 115-118.

White, W. M. (2015b). "Probing the Earth's Deep Interior Through Geochemistry." Geochemical Perspectives **4**(2): 95-251.
Wilson, S. C., B. J. Murton and R. N. Taylor (2013). "Mantle composition controls the development of an Oceanic Core Complex." Geochemistry, Geophysics, Geosystems **14**(4): 979-995.
Workman, R. K. and S. R. Hart (2005). "Major and trace element composition of the depleted MORB mantle (DMM)." Earth and Planetary Science Letters **231**(1–2): 53-72.
Wyllie, P. J. (1970). "Ultramafic rocks and the upper mantle."

Appendix 1: Sample description

Table A1-1: Description abbreviations

A	Aphyric
P	Phyric
V	Variolitic
B	Basalt
Px	Pyroxene
Pl	Plagioclase
Ol	Olivine
mp	Microphenocrysts
G	Glass
B-G	Basalt with glassy rim
D	Dolerite
B-A	Altered basalt

Table A1-1: Samples with descriptions. The abbreviation "ROC" suggests that the sample was collected by a ROV. Abbreviations for rock type, texture and visible minerals (i.e. visible phenocrysts) are found in table A1-1. Abbreviations for institution of analysis is B (University of Bergen) and N (University of Nantes).

Sample name	Latitude	Longitude	Depth	Domain	Rock type	Texture	Mineralogy	Institution of analysis	
								Isotopes	Trace
ODM-ROC-V547-100g	13.3089	-44.8751	3435	AV	B	Aphyric		B	N
ODM-ROC-V547-099g	13.3105	-44.8739	3402	AV	B	Aphyric		-	N
ODM-ROC-V547-098g	13.3097	-44.8751	3447	AV	B	Glass		-	N
ODM-ROC-V546-097	13.5057	-44.9649	2283	OCC30-CS		Phyric	pl + ol	B	N
ODM-ROC-V546-096	13.5066	-44.9728	2417	OCC30-CS	B-A	Aphyric	mp (pl)	-	N
ODM-ROC-V546-095g	13.5072	-44.9767	2478	OCC30-CS	B-G	Glass		-	N
ODM-ROC-V546-094	13.5086	-44.9789	2518	OCC30-CS	B-A	Phyric	mp	-	N
ODM-ROC-V545-084	13.4245	-44.9258	2888	NF	B	pl + ol	mp (pl + ol < 3%)	B	N
ODM-ROC-V545-083g	13.4245	-44.9251	2928	NF	B	Aphyric	mp (pl < 1%)	-	N
ODM-ROC-V545-082g	13.4245	-44.9245	2957	NF	B	Aphyric	mp (pl < 3%)	-	N
ODM-ROC-V545-081g	13.4247	-44.9239	3003	NF	B	Aphyric	mp (pl < 3%)	-	N
ODM-ROC-V545-080g	13.4248	-44.9234	3022	NF	B	Aphyric	mp (pl < 3%)	-	N
ODM-ROC-V545-079g	13.4247	-44.9231	3049	NF	B	Microphyri		-	N
ODM-ROC-V545-078g	13.4243	-44.9197	3007	SM	B	Aphyric		-	N
ODM-ROC-V545-077g	13.4246	-44.9180	2952	SM	B-G	Aphyric		-	N
ODM-ROC-V545-076	13.4249	-44.9174	2950	SM	B	Microlithic	mp (pl)	B	N
ODM-ROC-V545-075g	13.4248	-44.9118	3005	SM	B	Aphyric	mp (pl < 1%)	-	N
ODM-ROC-V545-074g	13.4235	-44.9085	3112	SM	B	Aphyric	mp (pl < 1%)	-	N
ODM-ROC-V545-073g	13.4228	-44.9068	3153	SM	B	Aphyric	mp (pl < 1%)	-	N
ODM-ROC-V545-072	13.4224	-44.9057	3259	SM	B-G	Microlithic	mp (pl < 1%)	B	N
ODM-ROC-V545-069g	13.4211	-44.8915	3588	NF	B-A	Aphyric		B	N
ODM-ROC-V544-063g	13.5040	-44.9171	2413	OCC30-HC	B	Aphyric		-	N
ODM-ROC-V544-063	13.5040	-44.9171	2413	OCC30-HC	B	Aphyric		-	N
ODM-ROC-V544-055	13.5063	-44.9017	2725	OCC30-HC	B	Aphyric		-	N
ODM-ROC-V542-039g	13.5025	-45.0130	2371	OCC30-CT	B-G	Aphyric		-	N
ODM-ROC-V542-038g	13.5008	-45.0127	2480	OCC30-CT	B-A	Vesicular		B	N
ODM-ROC-V542-037	13.5002	-45.0124	2538	OCC30-CT	B-A	Phyric		-	N
ODM-ROC-V542-029	13.5011	-44.9923	2703	OCC30-CT	B	Microlithic	mp (Pl + Ol)	-	N
ODM-ROC-V540-002g	13.5257	-44.9553	2798	OCC30-CS	B	Aphyric	mp (ol)	B	N

								Institution of analysis	
Sample name	Latitude	Longitude	Depth (m)	Domain	Rock type	Texture	Mineralogy	Isotopes	Trace
ODM-ROC-V560-404	13.5118	-44.9384	2188	OCC30-CS	B	Porphyric	pl	B	N
ODM-ROC-V560-403	13.5117	-44.9355	2209	OCC30-CS	B	Aphyric	mp (pl + ol)	-	N
ODM-ROC-V559-381	13.5122	-44.9420	2195	OCC30-CS	B	Aphyric		B	N
ODM-ROC-V559-379	13.5128	-44.9424	2251	OCC30-CS	D			-	N
ODM-ROC-V559-374	13.5119	-44.9506	2276	OCC30-CS	B	Aphyric		-	N
ODM-ROC-V559-373	13.5118	-44.9553	2342	OCC30-CS	B	Microphyric	pl	-	N
ODM-ROC-V558-352g	13.5069	-44.8912	2798	OCC30-CS	B	Porphyric	pl	-	N
ODM-ROC-V558-351	13.5068	-44.8911	2802	OCC30-CS	B	Porphyric	pl	B	-
ODM-ROC-V558-341(A)	13.4989	-44.8998	2830	OCC30-CS	B	Aphanitic		-	N
ODM-ROC-V556-314	13.3159	-44.9558	2233	OCC20-CT	B	Porphyric	pl + ol	-	N
ODM-ROC-V556-313	13.3162	-44.9557	2235	OCC20-CT	B	Aphyric	mp (pl)	-	N
ODM-ROC-V556-312	13.3162	-44.9534	2196	OCC20-CT	B	Porphyric	pl + ol	-	N
ODM-ROC-V556-311	13.3149	-44.9508	2222	OCC20-CT	B			-	N
ODM-ROC-V556-307	13.3065	-44.9511	2425	OCC20-CT	B	Aphyric		B	N
ODM-ROC-V556-293	13.2743	-44.9504	2883	OCC20-CT	B	Aphyric	mp (pl)	B	N
ODM-ROC-V555-290g	13.3243	-44.9653	1919	OCC20-CT	B-G	Aphyric		B	N
ODM-ROC-V555-289	13.3248	-44.9636	1969	OCC20-CT	B	Phyric	pl	-	N
ODM-ROC-V555-287	13.3253	-44.9548	2165	OCC20-CT	B-A	Phyric	pl	-	N
ODM-ROC-V555-284	13.3262	-44.9535	2135	OCC20-CT	B-A	Aphyric	mp (pl)	-	N
ODM-ROC-V555-283	13.3252	-44.9524	2112	OCC20-CT	B	Aphyric	mp (pl)	-	N
ODM-ROC-V555-282	13.3252	-44.9525	2115	OCC20-CT	B	Phyric	mp (pl + ol)	-	N
ODM-ROC-V555-281	13.3258	-44.9510	2107	OCC20-CT	B	Aphyric		-	N
ODM-ROC-V554-263	13.5076	-44.8928	2787	OCC30-HC	B	Phyric		-	N
ODM-ROC-V554-247	13.5022	-44.8972	2847	OCC30-HC	B	microcrystal	mp (pl)	-	N
ODM-ROC-V554-244	13.5020	-44.8960	2894	OCC30-HC	B	Phyric	pl	-	N
ODM-ROC-V554-242	13.5018	-44.8957	2905	OCC30-HC	B	Phyric	pl	-	N
ODM-ROC-V551-177	13.3368	-44.8982	3176	OCC20-CS	B-A			-	N
ODM-ROC-V550-160	13.3068	-44.9065	2188	OCC20-CS	B	Aphyric		B	N
ODM-ROC-V550-156	13.3061	-44.9015	2209	OCC20-CS	B	Phyric	pl +px	B	N
ODM-ROC-V547-101g	13.3094	-44.8782	3432	AV	B	Aphyric		-	N

Table A1-2: Samples with descriptions. The abbreviation "DR" suggests that the sample was collected by a dredging. Abbreviations for rock type, texture and visible minerals (i.e. visible phenocrysts) are found in table A1-1. Abbreviations for institution of analysis is B (University of Bergen) and N (University of Nantes).

	On bottom		Off bottom					Institute of analysis	
Samples	Latitude	Longitude	Latitude	Longitude	Depth (m)	Domain	Rock types	Isotopes	Trace element
ODM-DR01-01-03-g	13.579	-45.021	13.575	-45.029	2462	OCC30-CS	Pillow basalt	B	N
ODM-DR01-01-04-g	13.567	-45.011	13.576	-45.030	2462	OCC30-CS	Pillow basalt	-	N
ODM-DR02-01-01g	13.496	-44.954	13.504	-44.945	2303	OCC30-CS	basalt	-	N
ODM-DR04-01-04g	13.488	-44.930	13.493	-44.930	2498	OCC30-CS	basalt	-	N
ODM-DR10-01-06	12.357	-44.957	13.349	-44.960	2546	OCC20-CT	basalt	B	N
ODM-DR11-1-07g	13.354	-44.941	13.352	-44.977	2529	OCC20-CT	basalt	-	N
ODM-DR12-01-06	12.245	-44.901	13.249	-44.910	3655	NF	basalt	B	N
ODM-DR13-01-12g	12.570	-44.930	13.562	-44.933	3002	OCC30-CS	basalt	B	N

Appendix 2: Data

Table A1: Major elements

Sample name	SiO_2	TiO_2	Al_2O_3	FeO	MnO	MgO	CaO	Na_2O	K_2O	P_2O_5	LOI%	Total	Total + LOI
ODM-ROC-V546-095g	50.7	1.31	14.8	9.58	0.16	7.97	10.99	2.38	0.28	0.17		99.41	
ODM-ROC-V546-094	48.13	1.33	15.41	8.41	0.15	7.4	11.11	2.62	0.26	0.17	4.22	95.92	100.14
ODM-ROC-V545-084	50.1	1.62	14.72	9.68	0.18	7.57	10.8	2.48	0.51	0.26		99	
ODM-ROC-V545-083g	47.73	0.58	17.09	9.27	0.17	10.62	11.75	1.82	0.09	0.07		100.2	
ODM-ROC-V545-082g	47.66	0.58	17.3	9.34	0.17	10.68	11.88	1.86	0.09	0.07		100.6	
ODM-ROC-V545-081g	47.53	0.62	16.81	9.35	0.17	11.51	11.36	1.86	0.13	0.08		100.4	
ODM-ROC-V545-080g	47.4	0.63	17.01	9.35	0.17	11.13	11.56	1.88	0.13	0.08		100.3	
ODM-ROC-V545-079g	47.56	0.64	17.12	9.31	0.17	10.85	11.61	1.88	0.13	0.08		100.3	
ODM-ROC-V545-078g	47.55	0.77	16.82	9.14	0.16	9.55	11.72	2	0.18	0.11		99	
ODM-ROC-V545-077g	48.18	0.79	17.08	9.26	0.17	9.47	11.95	2.03	0.18	0.11		100.2	
ODM-ROC-V545-076	48.03	0.8	16.92	9.13	0.17	9.37	11.74	2.02	0.22	0.11		99.52	
ODM-ROC-V545-075g	48.38	0.79	17.12	9.16	0.17	9.48	11.85	2.02	0.18	0.1		100.2	
ODM-ROC-V545-074g	46.57	0.68	16.56	8.97	0.16	9.29	11.62	1.88	0.12	0.09		96.95	
ODM-ROC-V545-073g	47.38	0.67	14.59	8.94	0.16	11.61	10.44	1.68	0.12	0.09		96.68	
ODM-ROC-V545-072	48.68	0.96	15.43	9.46	0.17	10.48	11.33	1.95	0.2	0.12	-0.14	99.83	99.69
ODM-ROC-V545-069g	48.49	0.65	16.69	8.64	0.15	10.78	12.04	1.9	0.14	0.07		100.5	
ODM-ROC-V544-063	49.82	1.45	14.63	9.33	0.18	7	10.73	2.53	0.26	0.2		97.17	
ODM-ROC-V544-063g	50.04	1.44	14.37	9.40	0.18	7.44	11.52	2.36	0.24	0.21	2.75	98.27	101.02
ODM-ROC-V544-055	41.4	1.48	17.97	10.8	0.12	11.62	10.04	0.75	0.5	0.21		96.12	
ODM-ROC-V542-039g	50.5	1.37	15.19	9.43	0.17	8.11	11.45	2.46	0.2	0.14		100.0	
ODM-ROC-V542-038g	50.43	1.37	14.01	8.02	0.15	8.19	10.31	2.97	0.13	0.19	2.43	96.67	99.1
ODM-ROC-V542-037	48.35	1.62	16.22	9.40	0.13	7.58	10.18	2.53	0.31	0.21		97.58	
ODM-ROC-V542-029	48.21	2.24	14.91	9.16	0.14	8.14	10.93	2.73	1.06	0.42		98.97	
ODM-ROC-V540-002g	49.95	1.34	14.11	9.31	0.17	7.84	10.55	2.19	0.43	0.2	0.25	97.14	97.39
ODM-DR13-01-12g	51.45	1.19	15.12	9.00	0.16	8.09	11.87	2.41	0.29	0.16		100.7	
ODM-DR04-01-04g	50.66	1.26	15	9.33	0.17	8.19	11.48	2.42	0.18	0.15		99.87	
ODM-DR02-01-01g	50.48	1.42	14.83	9.42	0.17	8.02	11.36	2.38	0.36	0.19		99.68	
ODM-DR01-01-04-g	50.38	1.32	14.59	9.14	0.16	8.41	11.07	2.38	0.35	0.18		99	
ODM-DR01-01-03-g	49.71	1.3	13.97	8.89	0.16	8.14	10.64	2.29	0.34	0.18		96.62	

Sample name	SiO_2	TiO_2	Al_2O_3	FeO_T	MnO	MgO	CaO	Na_2O	K_2O	P_2O_5	LOI %	Total	Total +LOI
ODM-ROC-V555-284	49.36	1.33	15.81	8.279	0.15	7.72	11.61	2.47	0.1	0.17	2.06	97.92	99.98
ODM-ROC-V555-283	50.21	1.27	14.81	9.259	0.16	7.82	11.62	2.25	0.19	0.14	0.83	98.76	99.59
ODM-ROC-V555-282	50.33	1.53	14.98	9.268	0.16	7.76	10.99	2.4	0.44	0.21	0.86	99.1	99.96
ODM-ROC-V555-281	50.04	1.37	15.07	8.926	0.16	7.83	11.45	2.33	0.32	0.18	0.84	98.66	99.5
ODM-ROC-V551-177	47.86	1.26	15.06	9.403	0.15	7.85	12.2	2.24	0.26	0.15	2.43	97.47	99.9
ODM-ROC-V547-101g	47.53	0.55	17.18	9.367	0.17	10.4	12.23	1.81	0.06	0.04		100.39	
ODM-ROC-V547-100g	47.56	0.56	17.22	9.241	0.16	10.5	12.03	1.86	0.06	0.06		100.29	
ODM-ROC-V547-099g	48.11	0.55	17.2	9.376	0.16	10.07	11.92	1.94	0.06	0.04		100.47	
ODM-ROC-V547-098g	47.88	0.57	17.06	9.223	0.16	10.1	11.76	1.9	0.07	0.05		99.8	
ODM-DR12-1-06g	48.77	1.19	14.96	9.673	0.17	9.3	10.53	2.27	0.22	0.15		98.3	
ODM-DR11-1-07g	49.97	1.37	14.87	8.845	0.16	8.71	11.25	2.46	0.39	0.21		99.22	
ODM-DR10-1-06g	50.82	1.65	14.01	10.069	0.18	6.88	10.43	2.58	0.28	0.2		98.23	
ODM-ROC-V560-404	50.6	1.73	15.1	9.511	0.16	6.39	11.01	2.58	0.81	0.29		99.23	
ODM-ROC-V560-403	50.4	2.15	13.95	11.464	0.19	6.36	9.57	2.8	0.78	0.35	0.41	99.29	99.7
ODM-ROC-V559-381	51.02	1.77	14.58	9.313	0.17	6.7	10.91	2.49	0.71	0.3	0.3	99	99.3
ODM-ROC-V559-379	52.58	1.24	16.37	12.769	0.17	4.15	3.31	3.3	0.04	0.79	3.58	96.15	99.73
ODM-ROC-V559-374	46.97	0.46	16.89	8.405	0.14	10.7	11.35	1.85	0.15	0.04		97.9	
ODM-ROC-V559-373	50.55	1.61	14.4	9.880	0.17	7.42	10.58	2.55	0.57	0.21		99.04	
ODM-ROC-V558-352g	50.29	1.65	14.87	9.601	0.17	6.98	11.01	2.47	0.6	0.29	0.29	99	
ODM-ROC-V558-	51.07	1.46	15.3	9.241	0.16	6.99	11.72	2.34	0.5	0.2	0.33	100	
ODM-ROC-V554-263	50.59	1.38	14.69	9.133	0.17	8.09	10.64	2.61	0.1	0.2		98.61	
ODM-ROC-V554-247	50.42	1.39	14.98	9.349	0.17	6.98	11.59	2.42	0.51	0.2		99.05	
ODM-ROC-V554-244	48.67	1.15	15.16	8.989	0.19	8	11.23	2.28	0.09	0.15		96.91	96.91
ODM-ROC-V554-242	49.82	1.18	15.31	8.477	0.24	8.1	11.79	2.28	0.11	0.14		98.39	
ODM-ROC-V546-097	45.54	2.73	12.83	10.087	0.15	8.63	10.46	2.3	1.99	0.57	4.46	96.43	100.89
ODM-ROC-V546-096	50.75	1.4	14.64	9.403	0.16	7.59	10.98	2.36	0.32	0.17	0.67	98.82	99.49

Sample name	SiO_2	TiO_2	Al_2O_3	FeO_T	MnO	MgO	CaO	Na_2O	K_2O	P_2O_5	LOI %	Total	Total +LOI
ODM-ROC-V556-314	49.4	0.91	17.97	6.533	0.12	7.74	13.27	2.25	0.2	0.12	1.24	30.97	32.21
ODM-ROC-V556-313	49.75	1.45	14.71	9.223	0.16	7.61	11.2	2.46	0.34	0.17	0.98	98.11	99.09
ODM-ROC-V556-312	49.71	1.12	15.72	8.126	0.15	8.76	11.83	2.22	0.22	0.13	1.32	98.89	100.21
ODM-ROC-V556-311	50.79	1.76	14.35	9.034	0.15	6.97	10.49	2.89	0.24	0.21	2.34	97.88	100.22
ODM-ROC-V555-290g	50.79	1.46	14.76	9.628	0.17	8.67	11.16	2.42	0.33	0.19		100.66	
ODM-ROC-V555-289	50.02	1.53	15.09	9.079	0.16	6.67	11.14	2.76	0.38	0.2	1.02	98.04	99.06
ODM-ROC-V555-287	49.32	1.33	15.93	8.315	0.14	7.56	12.01	2.77	0.45	0.18	1.19	98.93	100.12

Sample name	Li	V	Cr	Ni	Zn	Rb	Sr	Y	Zr	Nb	Cs	Ba	La	Ce	Pr	Nd
ODM-DR04-01-	5.77	252	315	102	778	3.14	119	27.33	80	6.551	0.036	3862	4.44	11.04	1.682	8.35
ODM-DR02-01-01g	5.9	263	285	114	82	7.1	163	27.8	106	13.87	0.072	84	8.06	18.55	2.6	11.8
ODM-DR01-01-04-g	5.6	241	306	123	76	6.5	177	26.1	99	13.09	0.07	81	8.07	18.14	2.47	11.0
ODM-DR01-01-03-g	5.2	258	323	127	76	6.3	171	25.2	99	13.12	0.068	80	7.89	17.92	2.48	11.4
ODM-ROC-V556-314	7.6	196	443	166	51	2.9	164	19.5	63	7.45	0.074	39	4.59	10.64	1.54	7.27
ODM-ROC-V556-313	5.8	273	250	90	78	5.5	146	30	104	9.95	0.072	60	6.59	16.2	2.39	11.5
ODM-ROC-V556-312	7.7	242	378	167	66	3.2	147	23.8	72	7.54	0.066	43	4.8	11.75	1.72	8.41
ODM-ROC-V556-311	8.7	206	256	76	83	2.8	207	23.8	106	15.36	0.012	51	8.10	17.59	2.41	11.3
ODM-ROC-V556-307	4.8	188	307	182	105	12.1	459.	21.26	174.6	31.66	0.258	186.0	19.7	42.74	5.70	26.1
ODM-ROC-V556-293	2.5	227	317	153	110	25.8	614.	24.39	243.1	51.72		317.4	28.8	61.80	8.18	35.8
ODM-ROC-V555-290g	5.6	270	320	128	82	6.2	152	28.5	103	12.02	0.065	76	7.61	18.02	2.58	12.1
ODM-ROC-V555-289	7.2	290	254	110	79	6	179	31.4	110	12.48	0.108	76	7.77	18.48	2.66	12.8
ODM-ROC-V555-287	10.9	239	359	115	72	16.9	228	22.1	88	15.1	1.591	121	8.18	18.04	2.49	11.4
ODM-ROC-V555-284	2.2	255	353	118	71	0.8	151	27.3	92	10.64	0.033	35	6.52	15.3	2.21	10.4
ODM-ROC-V555-283	5.5	282	224	89	78	2.6	117	28.3	78	6.7	0.033	36	4.59	11.6	1.79	8.99
ODM-ROC-V555-282	9.1	288	283	134	86	8.1	149	30.1	109	13.5	0.219	75	8.16	19.16	2.72	12.8
ODM-ROC-V555-281	5.3	268	296	108	78	5.4	149	27	96	13.06	0.056	73	7.63	17.53	2.45	11.3
ODM-ROC-V551-177	5.8	267	256	136	67	2.9	93	28.7	88	5.63	0.02	34	4.33	11.57	1.82	9.31
ODM-ROC-V547-101g	2.7	137	374	187	52	1.2	122	13.3	22	2.04	0.013	13	1.42	3.66	0.57	2.94
ODM-ROC-V547-100g	2.8	141	368	187	53	1.1	120	13.5	25	2.27	0.012	14	1.47	3.76	0.58	3
ODM-ROC-V547-099g	2.7	139	367	170	52	1.2	122	13.6	23	2.08	0.012	13	1.4	3.62	0.57	2.99
ODM-ROC-V547-098g	2.9	147	384	181	53	1.3	122	14.2	26	2.44	0.015	16	1.59	4.14	0.63	3.21
ODM-ROC-V560-404	4.7	272	190	82	94	15.7	228	31.4	146	25.09	0.422	153	14.4	30.96	4.1	17.7
ODM-ROC-V560-403	6.1	308	147	82	107	15.4	238	38.8	176	28.54	0.175	186	15.8	34.26	4.66	20.9
ODM-ROC-V559-381	4.1	283	201	86	87	13.2	224	31.3	149	25.58	0.168	152	14.2	30.39	4	17.2
ODM-ROC-V559-379	3.6	88	0	13	58	0.4	140	65	47	76.58	0.01	104	47.0	96.61	12.09	49.8
ODM-ROC-V559-374	16.2	127	409	223	47	3.2	112	12.7	19	1.51	0.164	7	1.08	3	0.48	2.55
ODM-ROC-V559-373	4.4	259	258	108	91	10.5	172	31.3	115	12.59	0.312	74	8.25	19.27	2.75	13.0

Table A2: Trace elements

Sample name	Eu	Gd	Tb	Dy	Ho	Er	Yb	Lu	Hf	Ta	Pb	Th	U
ODM-DR04-01-	1.021	3.835	0.690	4.526	0.966	2.713	2.625	0.40	2.043	0.390	0.397	0.3660	0.1110
ODM-DR02-01-01g	1.15	4.46	0.752	4.72	0.997	2.79	2.707	0.42	2.6	0.79	0.641	0.754	0.223
ODM-DR01-01-04-g	1.17	4.48	0.747	4.47	0.934	2.58	2.462	0.38	2.34	0.73	0.646	0.774	0.231
ODM-DR01-01-03-g	1.06	3.95	0.67	4.23	0.897	2.52	2.445	0.38	2.4	0.75	0.636	0.761	0.221
ODM-ROC-V556-314	0.82	2.87	0.496	3.21	0.68	1.9	1.796	0.28	1.58	0.4	0.451	0.417	0.245
ODM-ROC-V556-313	1.17	4.4	0.766	4.93	1.06	2.97	2.864	0.44	2.57	0.56	0.494	0.558	0.17
ODM-ROC-V556-312	0.92	3.42	0.607	3.97	0.849	2.39	2.302	0.35	1.84	0.42	0.278	0.409	0.175
ODM-ROC-V556-311	1.23	4.27	0.711	4.27	0.839	2.21	1.906	0.28	2.71	0.83	0.372	0.806	0.454
ODM-ROC-V556-307	2.17	6.30	0.922	5.09	0.92	2.40	1.73	0.242	4.38	1.82	0.777	1.65	0.588
ODM-ROC-V556-293	2.65	7.64	1.06	5.83	1.00	2.53	1.74	0.239	5.88	3.02	1.06	2.65	0.896
ODM-ROC-V555-290g	1.19	4.14	0.717	4.71	0.998	2.8	2.714	0.42	2.5	0.67	0.728	0.662	0.195
ODM-ROC-V555-289	1.25	4.64	0.811	5.22	1.105	3.11	3.003	0.46	2.73	0.7	0.554	0.689	0.231
ODM-ROC-V555-287	1.1	3.75	0.619	3.8	0.78	2.11	1.971	0.3	2.17	0.82	0.375	0.772	0.439
ODM-ROC-V555-284	1.1	3.99	0.698	4.49	0.96	2.66	2.564	0.39	2.33	0.58	0.404	0.603	0.178
ODM-ROC-V555-283	1.04	3.91	0.709	4.68	1.014	2.85	2.779	0.43	2.08	0.39	0.391	0.376	0.141
ODM-ROC-V555-282	1.21	4.56	0.785	4.97	1.062	2.95	2.832	0.43	2.71	0.76	0.55	0.739	0.272
ODM-ROC-V555-281	1.09	4.08	0.705	4.48	0.958	2.68	2.565	0.4	2.37	0.74	0.535	0.719	0.393
ODM-ROC-V551-177	1.03	3.96	0.713	4.69	1.008	2.84	2.794	0.43	2.21	0.33	0.317	0.32	0.175
ODM-ROC-V547-101g	0.53	1.65	0.318	2.18	0.483	1.39	1.392	0.22	0.65	0.13	0.222	0.119	0.032
ODM-ROC-V547-100g	0.51	1.73	0.324	2.23	0.495	1.42	1.424	0.22	0.69	0.14	0.18	0.133	0.039
ODM-ROC-V547-099g	0.52	1.7	0.318	2.24	0.495	1.42	1.422	0.22	0.66	0.13	0.191	0.122	0.034
ODM-ROC-V547-098g	0.55	1.78	0.335	2.32	0.506	1.45	1.475	0.23	0.72	0.15	0.214	0.144	0.039
ODM-ROC-V560-404	1.44	5.46	0.892	5.39	1.12	3.09	2.904	0.45	3.58	1.44	0.996	1.407	0.44
ODM-ROC-V560-403	1.74	6.51	1.075	6.61	1.38	3.83	3.668	0.55	4.19	1.56	0.976	1.582	0.494
ODM-ROC-V559-381	1.39	5.39	0.881	5.4	1.126	3.11	2.921	0.45	3.77	1.43	0.994	1.425	0.478
ODM-ROC-V559-379	3.22	13.05	2.023	11.21	2.249	6.01	4.989	0.69	2.08	4.35	1.133	3.091	0.49
ODM-ROC-V559-374	0.48	1.54	0.291	2.05	0.46	1.33	1.348	0.21	0.57	0.1	0.161	0.09	0.047
ODM-ROC-V559-373	1.28	4.94	0.85	5.35	1.119	3.09	2.904	0.44	3	0.75	1.063	0.727	0.232

Sample name	Li	V	Cr	Ni	Zn	Rb	Sr	Y	Zr	Nb	Cs	Ba	La	Ce	Pr	Nd
ODM-ROC-V558-352g	5.0	210	252	169	77	7.9	179	24.1	90	12.93	0.182	123	8.62	18.39	2.47	10.96
ODM-ROC-V558-341(A)	4.3	278	242	83	86	9	174	27.1	103	16.22	0.146	101	9.17	20.28	2.76	12.32
ODM-ROC-V554-263	1.6	253	266	119	32	0.4	194	23.7	66	15.06	0.004	54	9.9	21.7	2.92	12.77
ODM-ROC-V554-247	5.3	272	237	88	91	10.2	164	26.9	97	14.15	0.278	89	8.35	18.57	2.56	11.38
ODM-ROC-V554-244	1.4	243	299	100	243	1	140	23.2	71	9.12	0.04	31	5.84	13.36	1.92	9.2
ODM-ROC-V554-242	2.1	258	321	104	84	1.2	147	23.4	73	9.41	0.044	48	5.81	13.37	1.91	9.19
ODM-ROC-V550-160	4.7	320	261	99	77	4.03	145.	27.76	105.4	10.14	0.05	55.26	6.98	16.54	2.45	12.21
ODM-ROC-V550-156	5.0	293	300	102	76	3.27	139.	23.77	83.91	7.18	0.167	42.52	5.31	12.69	1.96	10.11
ODM-ROC-V546-097	2.1	208	309	141	105	26.2	566	25.6	235	58.01	0.257	306	29.8	63.5	8.16	34.03
ODM-ROC-V546-096	4.3	235	313	128	85	5.5	170	23.3	93	11.99	0.057	73	7.08	16.4	2.33	10.94
ODM-ROC-V546-095g	5.0	215	305	128	83	5.5	166	22	89	11.49	0.057	66	6.43	14.82	2.09	9.74
ODM-ROC-V546-094	26.5	254	261	55	80	3.7	153	28.1	93	8.29	0.211	25	5.89	14.32	2.16	10.36
ODM-ROC-V545-084	5.7	264	264	97	83	9.7	194	32.6	131	19.76	0.096	117	11.1	24.88	3.39	15.14
ODM-ROC-V545-083g	2.8	132	328	191	50	1.5	110	14.5	29	3.17	0.016	19	1.97	4.75	0.7	3.42
ODM-ROC-V545-082g	2.8	131	313	189	50	1.5	111	14.7	29	3.16	0.016	19	2.02	4.83	0.71	3.54
ODM-ROC-V545-081g	2.8	138	359	231	52	2.1	118	15	34	4.39	0.022	27	2.73	6.27	0.88	4.18
ODM-ROC-V545-080g	2.9	134	344	211	51	2.1	120	15	35	4.54	0.022	27	2.62	6.06	0.85	4.05
ODM-ROC-V545-079g	3.0	128	318	192	50	2.1	122	15.4	35	4.44	0.023	27	2.73	6.17	0.87	4.12
ODM-ROC-V545-078g	3.6	153	301	151	55	3.2	134	17.7	49	6.64	0.032	39	3.72	8.28	1.14	5.24
ODM-ROC-V545-077g	3.3	160	292	142	54	3.1	134	17.7	47	6.49	0.032	40	3.81	8.48	1.18	5.42
ODM-ROC-V545-076	3.0	166	321	153	59	3.4	133	17.9	49	6.66	0.037	42	3.9	8.79	1.24	5.87
ODM-ROC-V545-075g	3.4	160	302	150	55	3.1	133	17.2	48	6.63	0.032	39	3.62	8.16	1.13	5.36
ODM-ROC-V545-074g	3.5	142	284	144	53	2.2	120	17.2	40	4.73	0.024	28	2.78	6.35	0.91	4.31
ODM-ROC-V545-073g	3.3	155	404	263	56	2.2	108	16.7	39	4.44	0.023	29	2.83	6.64	0.97	4.76
ODM-ROC-V545-072	4.2	209	359	208	65	3.9	122	21.3	60	7.8	0.04	48	4.57	10.65	1.51	7.15
ODM-ROC-V545-069g	2.8	155	439	226	57	2.1	135	13.7	33	4.12	0.021	30	2.49	6.02	0.87	4.19

Sample name	Eu	Gd	Tb	Dy	Ho	Er	Yb	Lu	Hf	Ta	Pb	Th	U
ODM-ROC-V558-352g	0.98	3.54	0.61	3.91	0.851	2.42	2.417	0.37	2.19	0.71	3.417	0.806	0.229
ODM-ROC-V558-	1.17	4.22	0.716	4.53	0.957	2.65	2.565	0.39	2.52	0.88	0.687	0.913	0.313
ODM-ROC-V554-263	1.07	3.99	0.667	4.14	0.856	2.35	2.183	0.33	2.02	0.86	0.238	0.642	0.113
ODM-ROC-V554-247	1.1	4.29	0.727	4.69	0.982	2.71	2.574	0.4	2.46	0.79	0.658	0.8	0.277
ODM-ROC-V554-244	1.07	3.52	0.612	3.81	0.818	2.29	2.181	0.33	1.94	0.55	1.403	0.522	0.226
ODM-ROC-V554-242	0.97	3.47	0.604	3.95	0.834	2.34	2.283	0.35	1.91	0.54	0.526	0.527	0.207
ODM-ROC-V550-160	1.29	4.65	0.835	5.46	1.16	3.44	3.18	0.481	2.87	0.625	0.499	0.644	0.26
ODM-ROC-V550-156	1.13	4.01	0.717	4.71	0.99	2.92	2.67	0.401	2.33	0.468	0.442	0.463	0.137
ODM-ROC-V546-097	2.32	7.43	1.021	5.29	0.94	2.32	1.761	0.25	5.26	3.14	1.48	2.764	0.886
ODM-ROC-V546-096	1.09	3.84	0.638	4.02	0.834	2.29	2.171	0.33	2.31	0.69	0.543	0.658	0.285
ODM-ROC-V546-095g	1	3.75	0.623	3.83	0.798	2.19	2.082	0.32	2.25	0.68	0.518	0.638	0.19
ODM-ROC-V546-094	1.1	4.23	0.736	4.59	0.983	2.75	2.631	0.4	2.42	0.5	0.713	0.463	0.163
ODM-ROC-V545-084	1.32	5.18	0.872	5.43	1.149	3.21	3.064	0.47	3.25	1.12	0.844	1.06	0.343
ODM-ROC-V545-083g	0.52	1.82	0.34	2.34	0.52	1.51	1.553	0.25	0.99	0.19	0.178	0.192	0.061
ODM-ROC-V545-082g	0.55	1.9	0.353	2.38	0.53	1.53	1.562	0.24	0.8	0.19	0.19	0.193	0.06
ODM-ROC-V545-081g	0.57	1.92	0.352	2.42	0.537	1.54	1.581	0.25	0.87	0.26	0.207	0.258	0.082
ODM-ROC-V545-080g	0.56	1.99	0.365	2.45	0.543	1.57	1.603	0.25	0.9	0.27	0.2	0.267	0.085
ODM-ROC-V545-079g	0.61	2.1	0.384	2.54	0.557	1.59	1.59	0.25	0.86	0.25	0.211	0.269	0.085
ODM-ROC-V545-078g	0.67	2.59	0.461	2.97	0.645	1.85	1.852	0.29	1.2	0.38	0.277	0.386	0.123
ODM-ROC-V545-077g	0.68	2.43	0.439	2.88	0.631	1.81	1.824	0.29	1.17	0.37	0.282	0.374	0.117
ODM-ROC-V545-076	0.72	2.4	0.431	2.94	0.648	1.85	1.864	0.29	1.19	0.38	0.458	0.384	0.145
ODM-ROC-V545-075g	0.63	2.42	0.436	2.86	0.633	1.82	1.838	0.29	1.21	0.39	0.269	0.375	0.119
ODM-ROC-V545-074g	0.64	2.47	0.448	2.85	0.624	1.78	1.776	0.28	1.02	0.27	0.229	0.278	0.088
ODM-ROC-V545-073g	0.63	2.29	0.415	2.74	0.6	1.71	1.713	0.26	0.99	0.25	0.23	0.253	0.078
ODM-ROC-V545-072	0.81	2.92	0.525	3.47	0.757	2.15	2.13	0.33	1.52	0.43	0.346	0.423	0.156
ODM-ROC-V545-069g	0.58	1.85	0.332	2.32	0.5	1.42	1.413	0.22	0.88	0.25	0.317	0.236	0.379

Sample name	Li	V	Cr	Ni	Zn	Rb	Sr	Y	Zr	Nb	Cs	Ba	La	Ce	Pr	Nd
ODM-ROC-V544-063	3.0	278	209	89	304	3.1	170	27.9	104	15.78	0.083	127	9.06	20.2	12.65	1.2
ODM-ROC-V544-063g	1.9	269	201	86	207	2.5	165	27.5	102	15.34	0.05	110	8.81	19.43	12.07	1.13
ODM-ROC-V544-055	8.8	284	182	160	28	7.4	175	25.3	68	17.93	0.05	87	10.91	23.15	13.82	1.18
ODM-ROC-V542-039g	5.9	272	284	104	77	3.2	129	29.5	93	6.12	0.034	38	4.58	12.35	9.77	1.12
ODM-ROC-V542-038g	6.5	160	361	163	68	0.9	247	18.4	91	15.23	0.034	88	7.93	17.2	10.83	1.13
ODM-ROC-V542-037	17.8	269	232	84	72	2.8	140	30.9	116	13.19	0.06	125	8.27	19.38	13.26	1.26
ODM-ROC-V542-029	5.1	239	341	149	90	14.9	443	25.5	189	43.58	0.321	248	21.92	46.13	24.93	1.83
ODM-ROC-V540-002g	4.8	251	291	127	77	8.2	166	26.8	98	14.98	0.119	94	8.89	19.69	12.37	1.16

Sample name	Eu	Gd	Tb	Dy	Ho	Er	Yb	Lu	Hf	Ta	Pb	Th	U
ODM-ROC-V544-063	0.743	4.72	0.995	2.78	2.675	0.41	2.59	0.87	0.679	0.876	0.28		
ODM-ROC-V544-063g	0.724	4.6	0.975	2.72	2.619	0.4	2.56	0.87	0.659	0.861	0.284		
ODM-ROC-V544-055	0.71	4.42	0.906	2.46	2.293	0.34	1.94	0.99	0.072	0.765	0.153		
ODM-ROC-V542-039g	0.757	4.9	1.054	2.98	2.905	0.44	2.35	0.36	0.528	0.341	0.102		
ODM-ROC-V542-038g	0.588	3.38	0.659	1.73	1.499	0.22	2.3	0.87	0.703	0.785	0.246		
ODM-ROC-V542-037	0.828	5.25	1.112	3.12	2.992	0.46	2.9	0.73	0.481	0.724	0.253		
ODM-ROC-V542-029	0.857	4.78	0.918	2.39	2.066	0.3	4.26	2.39	1.302	2.223	0.791		
ODM-ROC-V540-002g	0.728	4.48	0.95	2.65	2.523	0.39	2.53	0.87	0.689	0.869	0.286		

Table A3: Isotopic ratios

Sample name	$^{87}Sr/^{86}Sr$	2SD	$^{143}Nd/^{144}Nd$	2SD	$^{206}Pb/^{204}Pb$ [b]	Error	$^{207}Pb/^{204}Pb$	Error	$^{208}Pb/^{204}Pb$	Error	$^{176}Hf/^{177}Hf$	Error
ODM-DR12-01-06	0.70292	0.000009			18.7057	0.000218	15.5386	0.00019206	38.2599	0.00053956	0.28320	0.000004
ODM-DR10-01-06	0.70260	0.000007			18.5648	0.000166	15.5224	0.00015304	38.1145	0.00046347	0.28322	0.000003
ODM-ROC-V556-307	0.70268	0.000008	0.51305	6.58E-06	19.4278	0.000151	15.6023	0.00015006	38.7388	0.00046554	0.28308	2.20E-06
ODM-ROC-V556-293	0.70274	0.00001	0.51305	3.85E-06	19.5099	0.000367	15.6023	0.00030517	38.8142	0.00079618	0.28309	2.42E-06
ODM-ROC-V555-290g	0.70267	0.000009	0.51308	4.15E-06	18.6840	0.000350	15.5198	0.00030609	38.2087	0.00091595	0.28320	2.22E-06
ODM-ROC-V547-100g	0.70239	0.000008	0.51312	4.84E-06	18.9691	0.000319	15.5398	0.00030611	38.4753	0.00084689	0.28323	1.96E-06
ODM-ROC-V560-404	0.70288	0.000009	0.51306	4.40E-06	19.0141	0.000265	15.5700	0.00023511	38.5493	0.00065784	0.28315	2.07E-06
ODM-ROC-V559-381	0.70281	0.000009	0.51306	7.95E-06	19.0040	0.000215	15.5697	0.00017808	38.5429	0.0004706	0.28315	2.05E-06
ODM-ROC-V558-351	0.70280	0.000008	0.51306	6.84E-06	18.9928	0.000245	15.5657	0.0002471	38.5259	0.00071987	0.28315	1.99E-06
ODM-ROC-V550-160	0.70267	0.000009	0.51312	4.78E-06	18.5517	0.000218	15.5164	0.00020907	38.0663	0.00060863	0.28334	2.81E-05
ODM-ROC-V550-156	0.70274	0.000009	0.51303	7.05E-06	19.4280	0.000151	15.6008	0.00020007	38.8568	0.00062366	0.28309	2.77E-06
ODM-ROC-V546-097	0.70273	0.000008	0.51308	8.02E-06	18.5795	0.000300	15.5218	0.00024007	38.1676	0.00067059	0.28323	2.41E-06
ODM-ROC-V545-084	0.70273	0.000009			18.8680	0.000308	15.5697	0.00026109	38.4123	0.00072385	0.28317	0.000003
ODM-ROC-V545-076	0.70255	0.000008			19.0300	0.000254	15.5804	0.00023307	38.5190	0.00061568	0.28319	0.000003
ODM-ROC-V545-073g	0.70250	0.000007			18.7635	0.000196	15.5573	0.00018205	38.3291	0.00050555	0.28322	0.000003
ODM-ROC-V545-069g	0.70248	0.000009			19.0455	0.000228	15.5657	0.00019606	38.6575	0.00057058	0.28322	0.000002
ODM-ROC-V542-038g	0.70307	0.000007			18.9828	0.000331	15.5706	0.00025508	38.4918	0.00097901	0.28313	0.000002
ODM-ROC-V540-002g	0.70278	0.000008			18.9072	0.000363	15.5721	0.00030411	38.5164	0.00095311	0.28317	0.000008
ODM-DR13-01-12g	0.70275	0.000009									0.28321	0.000004
ODM-DR01-01-03-g	0.70273	0.000009			18.9748	0.000369	15.5589	0.00026006	38.6392	0.00152143	0.28320	0.000003

Appendix 3: Source-, melting-, and mixing model

To estimate the nature and evolution of the 13º00'-13º36'N basalts, a comprehensive model has been made. In this model the composition and evolution of mantle sources, the extent of melting, and the mixing relationship between melts derived from different sources is calculated. For simplicity, a binary mixing scenario between an enriched and a depleted component is assumed.

A4.1 Enriched component

A quantitative model from Stracke, Bizimis et al. (2003) was used here to reproduce the isotopic- and trace element composition of a recycled oceanic crust. According to this model, the differentiation age (i.e. the time elapsed since the source was extracted from the bulk silicate earth) is ~ 4.55 Ga. Input parameters in this model are:

1. Protolith composition
2. Time of isolation from the bulk silicate Earth reservoir
3. Influence of ancient sediments
4. The magnitude of metasomatism occurring in the subduction zone
5. The extent of eclogite melting and interaction of this melt with a given ambient mantle
6. Extent and mode of melting accountable for the final, enriched melts

The protolith composition plays a major role in the present-day composition, particularly for Pb isotopic ratios. No adequate fit with the data of this study was found for protolith compositions analogous to those used by Stracke, Bizimis et al. (2003), that is, an oceanic crust consisting of 25% fresh average N-MORB (Sun and McDonough 1989), 25% altered MORB (Staudigel, Plank et al. 1996) and 50% average gabbro (Hart, Blusztajn et al. 1999). The best fit for the eclogite protolith is an oceanic crust consisting of 55% fresh N-MORB and 45% altered MORB.

Initial isotopic compositions of the ancient recycled crust are equal to those of the oceanic crust upon recycling. Equation 1.7 (appendix 4) was used to estimate isotope compositions at the time of recycling from average Present-day MORB compositions and bulk silicate earth (BSE)

compositions were used to estimate composition at the time of recycling. A two-stage evolution from the BSE is considered for the Sr-, Nd-, and Hf-isotopic system, whereas a single-stage evolution is considered sufficient to account for the decay of the Pb-system. The age of the recycled crust is estimated here to be ~2 Ga. As pointed out by Stracke, Bizimis et al. (2003), the age of recycled crust is a free parameter that comes with a significant uncertainty.

Exclusion of sediment influence on the protolith crusts is ultimately attributed to observations in the Pb-isotopic system. The presence of sediments, even very low concentrations (< 0.5 %) decouples the U and Th from each other, resulting in too low $^{206}Pb/^{204}Pb$ and too high $^{208}Pb/^{204}Pb$.

It becomes clear from this model that the influence of altered MORB is significant for the $^{206}Pb/^{204}Pb$ ratios and the $^{87}Sr/^{86}Sr$ ratios of the HIMU component. This observation agrees with the high U/Pb and Rb/Sr ratios expected to follow from seawater interaction (Stracke, Bizimis et al. 2003). Dehydration and loss of fluid mobile elements induces the same effect. Significant subduction modification, i.e. metasomatism may account for some of trace element systematics observed in figure 16. Specifically, such mechanisms fractionate elements according to their mobility coefficients (Kogiso, Tatsumi et al. 1997), ultimately depriving the subducted oceanic crust in the most mobile elements; K, Pb, Rb, U, La, Th, Ba, and Cs but leaving elements like the REE, Ta, Nb, Hf, Sm, and Nd behind. The effect of subduction zone dehydration is obvious from the prominent, positive Nb and Ta anomalies, as well as the negative Pb anomalies (figure 16). To reproduce the negative Rb, Th, U, and K anomalies and the positive Nb and Ta anomalies observed in 13°20'-13°30'N lavas, the protolith is required to have undergone significant metasomatism. The best fit with the data is for a recycled component with moderate loss of fluid mobile elements. A reduction in trace element loss during subduction is done by reducing the mobility coefficients provided by Stracke, Bizimis et al. (2003) reduced by 55%.

Single stage, low F batch melting of pure eclogite (partition coefficients and modes given in table A3-1 and A3-2) produces melts with extreme enrichments in incompatible elements, inconsistent with the observations made in the 13°20'-13°30'N lavas. A two-stage non-modal (equation 1.3, appendix 4) melting model for the enriched melts successfully resolves this issue in lowering the incompatible trace element compositions. The first melting stage is consistent with low-F (~7%) eclogite melting (table A3-2). In phase, reactive eclogite melts interact with

olivine-rich peridotite, ultimately forming clinopyroxene (Sobolev, Hofmann et al. 2005). Melting of the resulting pyroxenite constitute the second smelting stage. In accordance with this model, the second phase occurs in the spinel stability field (i.e. spinel partition coefficients and modes). The best fit is when a depleted source is added to the estimated enriched component. This scenario is consistent with that described by Sobolev, Hofmann et al. (2007). The most suitable scenario is one where a mixture of 80% eclogite melts react with 20% ambient mantle, which in turn melts at ~4% in the spinel stability field.

A4.3 Depleted component

Analogous with the previous model suggested for the 13º20'-13º30'N area (Wilson, Murton et al. 2013), this model is consistent with a depleted end-member with more extreme isotopic signals than average DMM (Salters and Stracke 2004). It becomes clear from this model that the best fit, particularly in the Hf-isotope system, is one where a ReLish component, i.e. an ancient garnet residue analogous to the component suggested by Hamelin, Bezos et al. (2013), has a certain impact on the depleted end-member. To constrain the nature and composition of this ReLish component, the following parameters are included:

1. Protolith composition
2. Extent of garnet field melting necessary to decouple different parent/daughter ratios in the source residue
3. The time elapsed since this melting event

The ReLish component is essentially considered a residue after non-modal melting (equation 1.3, appendix 4) of some mantle component in the garnet stability field, followed by protracted isolation of this residual mantle. The best fit for the trace element systematics is one where this initial mantle component is relatively enriched. A viable candidate for the protolith is recycled oceanic crust. Given that this model does not consider the effect of slab-modifications or modal eclogite melting as expected for recycled oceanic crust, it is likely that the protolith modeled here is an oversimplification of the actual ReLish protolith. Nevertheless, the model indicates that the ReLish protolith must be less depleted in incompatible elements than the average DMM (Salters and Stracke 2004), and that it decouples the Hf-isotopic system from the remaining

isotopic systems. Indeed, substitution of the recycled oceanic crust protolith with that of a primitive upper mantle (PUM) (McDonough and Sun 1995) produces similar mixing curves when combined with the suggested enriched end-member.

The extent of protolith melting to produce the ReLish composition is ambiguous in this model. As discussed in the following section, the depleted end-member may be reproduced by two scenarios, and the properties of the ReLish component differs for the different scenarios. Before establishing the extent of protolith melting, it becomes necessary to introduce the two different models for the depleted end-member. Regardless of model, the best fit for the melting extent of the final, depleted end-member is ~1%.

A.4.4 Two mixing models

Ultimately, these end-members are constrained by the amount of ReLish in the ambient mantle. The two models suggested here are; (1) Mixing between pyroxenite (interaction between eclogite melts and UDMM) and a ReLish-UDMM derived melts, and (2) mixing between pyroxenite and eclogite influenced ReLish.

In model 1, the extent of ReLish protolith melting in the garnet stability field is considered extensive (batch melting ~ 18%). In model 2, the ReLish component requires a significantly lower melting extent (batch melting ~ 10%) to reproduce the observed variability. In both suggested ReLish compositions, the time elapsed since the melting event is estimated to be 2.1 Ga.

To reduce the extreme depletions observed in ReLish, the depleted component requires buffering by a less depleted mantle component. In model 1, this component is the UDMM (i.e. source-source mixing), whereas eclogite melts provides a similar effect in model 2 (i.e. source-melt interaction). Furthermore, the extent of melting to produce sufficient incompatible trace element enrichment from these highly depleted end members is estimated to be extremely low in both models (~ 1%).

In model 1, the depleted end-member consist of a mixture between UDMM (~ 75%) and ReLish (35%). Mixing of melts generated from this component with those derived from an enriched

component generated by interaction between eclogite melts (~80%) and ambient UDMM (~20%) successfully reproduces the data trend.

Alternatively, model 2 represent mixing scenario between melts generated from ReLish mantle influenced by eclogite melts and those generated from an eclogite melt – UDMM reactant. If this model holds, the best fit is a mixture between melts generated from a depleted end-member with ReLish: low-F eclogite melt ~ 75:35, and an enriched end-member with UDMM: low-F eclogite melt ~ 20:80.

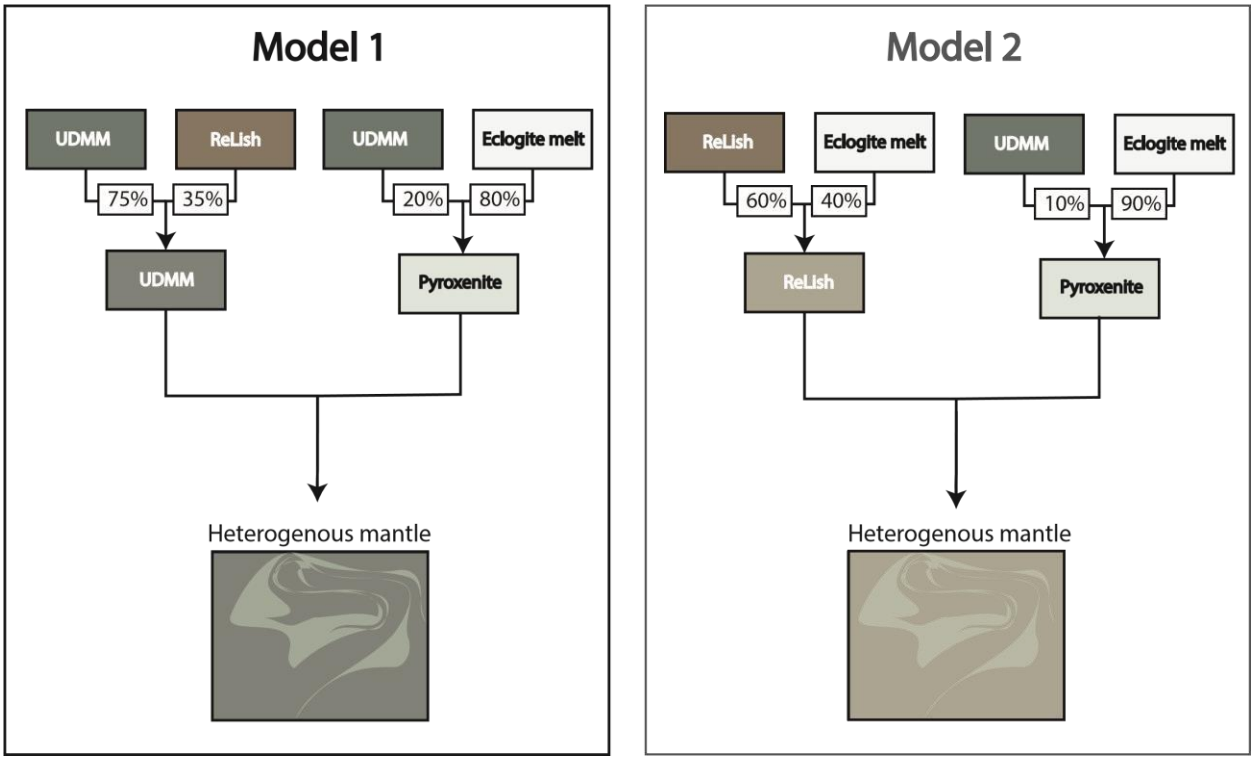

Figure A3-1: Schematic illustration of melting model 1 and 2. Model 1: mixing between a depleted end-member (75% UDMM and 35% ReLish) and an enriched end-member (80% eclogite melt and 20% UDMM). Model 2: mixing between a depleted end-member (60% ReLish and 40% eclogite melts) and an enriched end-member (90% eclogite melts and 10% UDMM)

Table A3-1: Trace element concentrations (ppm) and isotopic ratios for ReLish, UDMM, bulk recycled igneous crust and bulk igneous crust, as well as fluid loss from bulk igneous crust associated with dehydration ReLish, bulk recycled igneous crust, and bulk igneous crust (protolith) estimated in this study. UDMM from Workman and Hart (2005). Mobility coefficients modified (reduced to 55%) from Kogiso, Tatsumi et al. (1997).

	ReLish	UDMM	Bulk recycled igneous crust	Fluid loss	Bulk igneous crust
Rb	0.00398	0.02000	3.09870	44.6%	1.71823
Ba	0.00310	0.22700	27.92350	28.9%	19.86059
Th	0.00141	0.00400	0.30722	20.7%	0.24351
U	0.00077	0.00180	0.12422	41.8%	0.07229
Nb	0.01588	0.08640	4.86715	2.2%	4.76007
Ta	0.00104	0.00560	0.27356	2.2%	0.26754
La	0.13891	0.13400	4.56895	30.9%	3.15920
Ce	0.54656	0.42100	12.78145	27.9%	9.21734
Pb	0.02384	0.01400	0.51708	44.6%	0.28672
Nd	0.93510	0.48300	10.49595	12.1%	9.22594
Sr	9.85795	6.09200	129.28000	22.4%	100.26957
Zr	9.89614	4.26900	94.97600	12.1%	83.48390
Hf	0.30413	0.12700	2.69570	12.1%	2.36952
Sm	0.52504	0.21000	3.41880	7.5%	3.16307
Eu	0.26305	0.08600	1.21355	4.6%	1.15815
Ti	2279	650	8659	3.2%	8382.99088
Gd	1.28050	0.32400	4.48305	2.8%	4.35977
Dy	1.87499	0.47100	5.51460	2.0%	5.40541
Y	11.82791	3.12900	32.03500	1.1%	31.68262
Er	1.29625	0.32900	3.60755	0.3%	3.59565
Yb	1.50331	0.34800	3.46120	0.8%	3.43455
Lu	0.22512	0.05600	0.52305	0.6%	0.52017
87Sr/86Sr	0.70104	0.70263	0.70364		0.70239
143Nd/144Nd	0.51399	0.51326	0.51284		0.51046
176Hf/177Hf	0.28534	0.28350	0.28280		0.28173
206Pb/204Pb	15.32818	17.57300	20.05786		15.15824
207Pb/204Pb	15.17588	15.40400	15.73738		15.21281
208Pb/204Pb	34.34446	37.20000	39.46878		34.52361

Table A3-2: Bulk partition coefficients for non-modal melting (D and P). Abbreviations Gt.= garnet stability field, Sp. = spinel stability field, and Ec. = eclogite melting (Stracke, Bizimis et al. 2003)

	Bulk D Gt.	Bulk P, Gt.	Bulk P, Sp.	Bulk D, Sp.	Bulk D, Ec.	Bulk P, Ec.
Rb	0.00026	0.00021	0.00029	0.00034	0.00032	0.00036
Ba	0.00005	0.00017	0.00006	0.00021	0.00025	0.00027
Th	0.00180	0.00692	0.00253	0.00952	0.01147	0.01261
U	0.00201	0.00837	0.00230	0.00864	0.01134	0.01195
Nb	0.00151	0.00335	0.00150	0.00333	0.00382	0.00390
Ta	0.00151	0.00335	0.00150	0.00333	0.00382	0.00390
La	0.00689	0.02294	0.00971	0.03396	0.03952	0.04379
Ce	0.00936	0.03386	0.01316	0.04803	0.05700	0.06285
Pb	0.00918	0.03262	0.01348	0.04927	0.05766	0.06411
Nd	0.02588	0.10355	0.03240	0.12119	0.15280	0.16414
Sr	0.01579	0.05890	0.02329	0.08739	0.10314	0.11446
Zr	0.03943	0.17570	0.02497	0.08342	0.14920	0.13561
Hf	0.04491	0.19828	0.03771	0.13699	0.20800	0.20440
Sm	0.05617	0.24449	0.05375	0.19967	0.28440	0.28827
Eu	0.08613	0.37398	0.07993	0.29425	0.42400	0.42670
Ti	0.09375	0.28855	0.09095	0.24990	0.33000	0.33450
Gd	0.15103	0.73838	0.08143	0.30061	0.59200	0.52360
Dy	0.22584	1.16169	0.07264	0.26087	0.74400	0.58020
Y	0.30570	1.58156	0.08242	0.28398	0.94960	0.70768
Er	0.34605	1.79710	0.08145	0.27049	1.03200	0.74310
Yb	0.59870	3.15310	0.09470	0.28200	1.64000	1.08200
Lu	0.64288	3.40005	0.10182	0.31532	1.77920	1.18061

Table A4-3: Mineral modes and melting modes from Stracke, Bizimis et al. (2003) used in the non-modal melting equation. Abbreviations Ol = olivine, Opx = orthopyroxene, Cpx = clinopyroxene, Gt = garnet and Sp = spinel.

	Garnet peridotite		Spinel peridotite		Eclogite	
	Source mineralogy	Melting mode	Source mineralogy	Melting mode	Source mineralogy	Melting mode
Ol	0.55	0.05	0.55	0.1	0	0
Opx	0.25	0.05	0.25	0.2	0	0
Cpx	0.12	0.45	0.18	0.68	0.8	0.89
Gt	0.08	0.45	0	0	0.2	0.11
Sp	0	0	0.02	0.02	0	0

Appendix 4: Equations

Table A4-1: Abbrevations used in equation 1.1 – 1.7 with explanations.

$\boldsymbol{D_i}$	*Bulk partition coefficient*
$\boldsymbol{P}$	*Non-modal partition coefficient*
$\boldsymbol{K_d^i}$	*Element partition coefficient in a mineral phase*
$\boldsymbol{C_i^{0l}}$	*Element concentration in a mineral phase*
$\boldsymbol{C_i^0}$	*Element concentration in source*
$\boldsymbol{C_i^S}$	*Element concentration in solid phase*
$\boldsymbol{x_i}$	*Proportion of rock-forming mineral*
$\boldsymbol{F}$	*Melt fraction*
$\boldsymbol{Mg\#^L}$	*Magnesium number in mantle melt*
$\boldsymbol{Mg\#^{ol}}$	*Magnesium number in mantle olivine*
$\boldsymbol{K^{Mg\#}}$	*Partition coefficient of Mg and Fe in mantle olivine*
$\boldsymbol{Rg}$	*Concentration of radiogenic daughter isotope*
$\boldsymbol{Ra}$	*Concentration of radioactive parent isotope*
$\boldsymbol{S}$	*Concentration of stable daughter isotope*

Bulk rock partition coefficient (D_i) (Hanson and Langmuir 1978):

$$D_i = \sum K_{di} x_i = \frac{C_i^S}{C_i^L} \quad (1.1)$$

Modal equilibrium melting (Shaw 1970):

$$C_i^L = \frac{C_i^0}{D_i + F(1 - D_i)} \quad (1.2)$$

Non-modal equilibrium melting equation (Shaw 1970):

$$C_i^L = \frac{C_i^0}{\mathrm{D} + F(1 - P)} \quad (1.3)$$

The equation for residual mantle:

$$C^s = \frac{(D-P) \times F}{1-F} \times \frac{1}{D-P} \times 1 - D \quad (1.4)$$

Fractional crystallization (Sen 2014):

$$C_L^i = C_0^i F^{D^i - 1} \quad (1.5)$$

Mg# of mantle equilibrated melts:

$$\left[\frac{Mg\#}{1-Mg\#}\right]^L = D^{Mg\#} \left[\frac{Mg\#}{1-Mg\#}\right]^{L^{ol}} \quad (1.6)$$

Assuming an average mantle peridotite, $K^{Mg\#}$values are expected to be ~0.3, ~0.32, and ~0.35 for pressures less than 0.5 GPa, 0.5 – 1.5 GPa, and more than 1.5 GPA respectively (Sen 2014).

Radiogenic growth:

$$\left(\frac{Rg}{S}\right)_t = \left(\frac{Rg}{S}\right)_0 + \left(\frac{Ra}{S}\right)_t \times e^{\lambda \mathrm{t} - 1} \quad (1.7)$$

Hanson, G. N. and C. H. Langmuir (1978). "Modelling of major elements in mantle-melt systems using trace element approaches." Geochimica et Cosmochimica Acta **42**(6): 725-741.

Sen, G. (2014). Petrology: Principles and Practice. New-Delhi, India, Springer-Verlag Berlin Heidelberg.

Shaw, D. M. (1970). "Trace element fractionation during anatexis." Geochimica et Cosmochimica Acta **34**(2): 237-243.

Stracke, A., M. Bizimis and V. J. M. Salters (2003). "Recycling oceanic crust: Quantitative constraints." Geochemistry, Geophysics, Geosystems **4**(3): n/a-n/a.